Design and Modeling of Soft Curved Reconfigurable Anisotropic Mechanisms

by

Yuhao Jiang

A Dissertation Presented in Partial Fulfillment
of the Requirements for the Degree
Doctor of Philosophy

Approved March 2023 by the
Graduate Supervisory Committee:

Daniel Aukes, Chair
Spring Berman
Hyunglae Lee
Hamidreza Marvi
Siddharth Srivastava

ARIZONA STATE UNIVERSITY

August 2023

ABSTRACT

This dissertation introduces and examines Soft Curved Reconfigurable Anisotropic Mechanisms (SCRAMs) as a solution to address actuation, manufacturing, and modeling challenges in the field of soft robotics, with the aim of facilitating the broader implementation of soft robots in various industries. SCRAM systems utilize the curved geometry of thin elastic structures to tackle these challenges in soft robots. SCRAM devices can modify their dynamic behavior by incorporating reconfigurable anisotropic stiffness, thereby enabling tailored locomotion patterns for specific tasks. This approach simplifies the actuation of robots, resulting in lighter, more flexible, cost-effective, and safer soft robotic systems.

This dissertation demonstrates the potential of SCRAM devices through several case studies. These studies investigate virtual joints and shape change propagation in tubes, as well as anisotropic dynamic behavior in vibrational soft twisted beams, effectively demonstrating interesting locomotion patterns that are achievable using simple actuation mechanisms. The dissertation also addresses modeling and simulation challenges by introducing a reduced-order modeling approach. This approach enables fast and accurate simulations of soft robots and is compatible with existing rigid body simulators. Additionally, this dissertation investigates the prototyping processes of SCRAM devices and offers a comprehensive framework for the development of these devices.

Overall, this dissertation demonstrates the potential of SCRAM devices to overcome actuation, modeling, and manufacturing challenges in soft robotics. The innovative concepts and approaches presented have implications for various industries that require cost-effective, adaptable, and safe robotic systems. SCRAM devices pave the way for the widespread application of soft robots in diverse domains.

DEDICATION

I dedicate this dissertation to my parents, for their constant love and support.

ACKNOWLEDGMENTS

I would like to express my deepest appreciation to my advisor, Prof. Daniel Aukes, for his valuable guidance, insightful feedback, and unwavering support throughout my research journey. His extensive knowledge, enthusiasm, and encouragement have been indispensable in shaping my ideas and my research.

I would like to extend my gratitude to Prof. Spring Berman, Prof. Hyunglae Lee, Prof. Hamidreza Marvi, and Prof. Siddharth Srivastava, who served as my committee members, for their invaluable guidance and feedback. Additionally, I would like to recognize the assistance and guidance provided by our collaborators, Prof. Nick Gravish, Prof. Cindy Harnett, and Prof. Ross Hatton.

I am also deeply grateful to my parents, Hong Zhang and Zhen Jiang, for their unwavering love, encouragement, and support. Their constant love and support have been the driving force behind my success.

Finally, I would like to acknowledge the immense support of my friends and colleagues, Mohammad Sharifzadeh, Dongting Li, Fuchen Chen, Amir Salimi Lafmejani, and Roozbeh Khodambashi, who have offered me a wealth of support and assistance throughout my Ph.D. study.

I am sincerely grateful to everyone who has offered their support and encouragement.

TABLE OF CONTENTS

CHAPTER Page

CHAPTER Page

CHAPTER Page

LIST OF TABLES

LIST OF FIGURES

Figure Page

Chapter 1

INTRODUCTION

Soft robotic systems have garnered substantial research attention in the past decade due to their reconfigurable and adaptable characteristics. Unlike traditional rigid-body robots, which typically operate within predefined workspaces, soft robots can adapt to their surroundings by actively or passively changing their shape and can assume multiple configurations with a high degree of freedom. This distinctive feature provides several advantages for soft robotic systems, such as increased flexibility and dexterity, enhanced safety for tasks involving humans, and improved energy efficiency.

1.1 Problem Definition

Soft robotic systems are yet to be widely applied in industries such as manufacturing, autonomous logistics, and transportation, unlike the traditional rigid-body robots that have already found extensive use in these areas. The primary reason for the limited use of soft robotic systems is attributed to three key challenges as follows:

1. **Actuation:** Soft robotic systems pose greater challenges for actuation compared to rigid-body robots, as they require more complex and less efficient mechanisms due to the cumbersome structures involving silicone casts, bladders, and chambers. Additionally, these mechanisms can be bulkier in comparison. Several approaches have been proposed to power soft robotics, including pneumatic, cable-driven, and shape memory alloy (SMA) actuation. However, these methods tend to have limited power output and large, cumbersome actuators that can wear out after repeated use. Additionally, to enable greater freedom of movement, these actuators require a significant

number of tubes, cables, or wires, which further contributes to their bulkiness and poor power efficiency.

2. **Modeling:** The modeling and simulation of the non-linear dynamics in soft robotic systems often rely on high-dimensional state space approaches like Cosserat rod and Finite Element Methods (FEM) to capture their intricate behavior. However, the computational requirements of these methods can pose challenges for design optimization and controls due to the considerable degrees of freedom inherent in soft bodies. Moreover, fabricating soft materials with high viscoelasticity can introduce variations in prototypes and between different prototypes, leading to inaccuracies, even with geometrically exact models.

3. **Manufacturing:** Conventional soft robots are typically created using silicone-cast structures with pneumatic chambers to enable actuation and sensing. However, this fabrication technique of mold-casting has its limitations, particularly when it comes to constructing intricate structures. Additionally, the mold-casted structure usually necessitates a thick wall for impermeability under high-pressure air, resulting in bulky size and cumbersome movements.

In summary, the limitations of efficient actuation in soft robotic systems hinder their ability to maneuver effectively and swiftly, thereby limiting their application in traditional industries like manufacturing, logistics, storage, and agriculture. Additionally, the modeling challenges of soft robotic systems impede effective control, further restricting their potential applications. The less robust and time-consuming manufacturing methods associated with soft robotic systems limit their mass production at a lower cost, thereby restricting their widespread use as well. Lastly, the high cost of soft robotic systems presents a barrier to their deployment in educational scenarios, where affordable tools are in high demand.

1.2 Solutions and Visions

This dissertation studies the curved geometry of thin elastic structures, which, when manipulated, can result in local shape change and reconfiguration of mechanical properties. This concept can be leveraged to create a new type of soft system, which we refer to as Soft Curved Reconfigurable Anisotropic Mechanisms (SCRAMs). By harnessing the geometry of soft surfaces, SCRAM systems overcome actuation challenges commonly encountered in soft robotic systems. Additionally, the simplified structure of SCRAM systems allows for easier modeling and manufacturing, resulting in lower costs.

Human-robot interaction remains a significant challenge for the robotics field, particularly when it comes to ensuring the safety of humans. Soft robots, with their deformable and flexible bodies, possess inherent advantages for addressing such challenges. By employing the SCRAM concept, the scale of actuators at the robot's end effectors can be significantly reduced. This reduction leads to the development of lighter and softer end effectors, enabling the adoption of safer working modes during tasks involving human interaction such as factories and warehouse logistics.

Amphibious robots have garnered significant research interest in recent decades due to their capability to adapt and maneuver in various environments and media through self-reconfigurability. Soft robots with reconfigurable bodies show promise for fulfilling the requirements of such tasks. SCRAM devices, characterized by simplified actuators and structures, offer substantial benefits in this context. By incorporating precisely-tuned geometries with complex dynamic behavior, SCRAM devices can be easily reconfigured to achieve various locomotion modes, effectively meeting specific environmental demands. As a result, they hold great potential for advancing the application of amphibious robots.

1.3 Contributions and Impacts

This dissertation focuses on investigating the actuation, modeling, and manufacturing aspects of SCRAM devices. It aims to address the challenges mentioned earlier by utilizing various case studies. Through these case studies, valuable insights are obtained, which are summarized as follows:

1. **Reconfigurable anisotropy:** The reconfigurable anisotropic stiffness serves as a fundamental concept in SCRAM devices, enabling the alteration of their static and dynamic behavior. This dissertation delves into the exploration of geometry and material designs to develop anisotropy in diverse soft structures to cultivate distinct behaviors. These behaviors are then utilized to generate purposeful locomotion patterns tailored to specific tasks.

2. **Modeling and simulation:** In this dissertation, a reduced-order modeling approach is introduced for simulating soft robots. This approach enables fast and accurate modeling and simulation of soft continuous structures. Notably, the method is highly compatible with widely used rigid body simulators available in the commercial domain, offering promising prospects for optimization and control techniques based on machine learning techniques.

3. **Manufacturing:** This dissertation also investigates the manufacturing processes for soft robotics, with a focus on understanding the landscape of 3D printing over traditional fabrication methods. It delves into the aspects of achieving waterproofing, flexibility, rigidity, compatibility, and manufacturability in soft robotic structures.

These efforts will not only have significant impacts on the soft robotic society but also extend their influence beyond robotic societies. Firstly, artificial intelligence has proven its

effectiveness in enhancing performance across diverse domains, such as unmanned manufacturing, autonomous driving, natural language processing, and data-driven control. The incorporation of machine learning techniques into the design, optimization, and control of soft robots has been a challenging yet valuable pursuit. This challenge primarily stems from the complexities associated with modeling soft robots, which typically exhibit highly nonlinear behavior and possess numerous degrees of freedom. SCRAM devices provide a potential solution to this challenge through their simplified structure, enabling the utilization of machine learning techniques for efficient optimization of performance. Additionally, there has been a significant demand for educational robots in K-12 education, as they serve as an ideal platform for teaching STEM classes and facilitating hands-on experiments to help students learn and solve scientific problems. To be effective in such scenarios, these robots need to be easily accessible, safe to interact with, and affordable. SCRAM robots, with their simple structures, offer promising potential for fabricating durable devices at a low cost, making them well-suited for educational applications. The integration of SCRAM robots in education holds power to greatly amplify the impact of the robotics community and foster the interest of K-12 students in robotics, thereby benefiting the future of the robotics field.

1.4 Dissertation Outline

This dissertation will start by delving into three separate case studies, each aiming to elucidate and exemplify the application of the SCRAM concept in generating a diverse range of intriguing locomotion patterns with simple actuation powers. The first case study focuses on showcasing how the local stiffness of soft tubes can be reconfigured by pinching forces, thereby enabling the cultivation of controllable virtual joints. The second case study connects the pinched tube and curved buckling beam via a continuous soft surface using a shape change propagation concept to show how curvature impacts the ability to transmit

shape change between continuous soft surfaces, simplifying power delivery and control signals required for soft robotic locomotion. The last case study delves into the investigation of anisotropic dynamic behavior in soft twisted beams. It demonstrates how simple vibratory actuation can generate complex three-dimensional locomotion by propagating waves through the soft twisted beam. Collectively, these case studies serve to underscore the potential of leveraging reconfigurable anisotropic stiffness in soft bodies to streamline actuation power in soft robots.

Following the case studies, the dissertation delves into a discussion on simplifying the modeling of high-degree-of-freedom SCRAM systems using a reduced-order modeling approach. This technique is applied to the aforementioned case studies, enabling quick and accurate dynamic simulations. Subsequently, the dissertation explores the manufacturing aspects of SCRAM devices. It delves into the fabrication process, which involves utilizing 3D printing technology, mold casting, and the laminate fabrication process. A comparative analysis of each method is also presented to provide insights into their respective advantages and limitations.

Chapter 2

RELEVANT BACKGROUNDS

2.1 Soft Robotic Systems and Actuation

In recent years, there has been a surge of interest in soft robots because of their remarkable capacity to engage with the surroundings through uncomplicated and flexible structures composed of soft materials. Their unique ability has led to extensive research and has facilitated the creation of innovative robots, including walking robots [108, 125, 69], swimming robots[58, 67], amphibious robots [6, 16], robotic arms [65, 77], robotic grippers [50, 122, 11], and robotic gloves [93, 43], etc. The adaptability provided by these characteristics is particularly advantageous when operating in challenging environments where a high level of interaction safety is required. This has empowered researchers to explore new avenues and push the boundaries of robotic development. Such robots often emulate bio-inspired systems such as snakes [86, 108, 70, 75, 97], octopuses [12, 65, 73, 113], and elephant trunks [96, 83, 137] due to their ability to contort themselves into highly complex shapes that would ordinarily be impossible with traditional rigid robots. This is possible because local curvature in any direction can be induced by properly mixing internal actuator forces. However, because of the material-dependent nature of soft-bodied robots, control difficulties can arise due to the high computational cost of estimating pose and optimizing trajectory in redundant, high degree-of-freedom continuum robots.

Actuation and its transmission through soft robotic systems have driven extensive study in recent decades [27, 131, 29]. Unlike actuation in traditional rigid-body robotic systems – which relies on motors, gears, shafts, and belts to actuate and transmit power – the morphology of soft actuators can be deformed to subsequently alter body shapes and drive robots

by stimulating or deforming soft materials. Commonly utilized actuators in soft robots can be categorized into four main types: pneumatic actuators [108], tendon-driven actuators [141], actuators based on shape memory alloys (SMAs) [89], and dielectric elastomer actuators [14]. Although there have been significant advancements in the development of various soft actuators for driving soft robots in applications such as human-robot interaction [92], bio-inspired robots [21], and wearable robotic systems [5], these systems often suffer from limited power and bulky size.

2.2 Tuning Stiffness in Soft Robots

In order to address these difficulties while utilizing the natural deformability of soft robots, a great deal of research has looked into tuning the stiffness of soft robots for the purpose of simplifying models and making more efficient controllers [72], including utilizing jamming [143, 135], active elastomers [82], tendon-driven solutions [110], as well as anisotropic [1] and functionally graded materials [8]. Tuning the shape or curvature of soft devices has been studied for its ability to alter system stiffness. Nguyen et al. highlight how curvature-change can modulate the stiffness of fish fins [84], while Pini et al. detail how internal stress fields can impart stiffness changes in thin sheets via two-dimensional bending [91]. This can be enhanced by weakening or creasing material along a curve to produce rapid transitions between static states in curved soft materials [9]. Curvature and shape change may also be actively controlled for the purposes of changing stiffness [134]. Some compact examples include the use of SMA tendons [62] and springs [112].

On the subject of stiffness-tuned soft robots, the majority of research has been dedicated to investigating how the design and positioning of internal actuators within continuum manipulators affect the configuration or state of the arm and the position of the end effector as a function of actuator states [86, 108, 70, 75, 97, 12, 65, 73, 113, 96, 83, 137, 18]. Various methods have been employed to modify stiffness; many notable papers focus on the

use of curvature to do this [72, 143, 135, 82, 110, 1, 8]. Additionally, studies have been conducted on the mechanics and stability analysis of structures that enhance stiffness using curvature [84, 91, 9]. Researchers have also investigated the use of a single actuator to increase or decrease the rigidity of a geometry [134, 62, 112].

2.3 Bi-stable and Multi-stable mechanisms in Soft Robots

The utilization of bi-stable and multi-stable mechanisms is prevalent in soft robotic systems for generating locomotion. These mechanisms possess two or more stable states that can be altered through actuation. By inducing such changes, these mechanisms can produce locomotion through the transition, thereby enabling the development of intriguing motion patterns. Due to the fact that these actuations solely need to initiate a shift between two stable states, they can be simple and energy-efficient. Additionally, no additional forces are necessary to sustain the state following actuation, as it naturally settles into its nearest stable configuration. These features have enabled researchers to generate interesting locomotions. Chi et al. [17] have developed a flapping robotic swimmer using a snap-through bi-stable mechanism actuated by a simple pneumatic actuator. In [36], Gelebart et al. have investigated a photoactive polymer film to explore its potential in developing a multi-stable mechanism capable of generating wave propagations. Gorissen et al. [41] have proposed an inflatable soft jumper using a bi-stable shell snapping mechanism. The bi-stable mechanism has also been used for generating grasping motion [114] and running motion [119].

2.4 Related Works in Soft Curved Surfaces and Shape Propagation

Flexibility and curvature play significant roles in enhancing locomotion capabilities in various natural structures. Certain observations have identified the utilization of active curvature or cupping in fish [30, 85], three-dimensional curvature in batoids [24], and the flexible flapping of insect wings [20] as strategies for optimizing locomotion efficiency

during a stroke. These examples highlight how nature exploits the benefits of flexibility and curvature to achieve efficient movement.

A technique known as curved crease folding has been extensively studied and applied in origami – the art of paper folding – to manipulate the curvature of thin sheet structures. Curved crease folding leverages the concept of curved paper creases to introduce and propagate curvature across interconnected developable surfaces. Researchers have computationally investigated this principle [49, 25, 59, 78, 35], and it has found applications in graphics [23, 117], architecture [117], and robotics [79].

While there are some similarities between curved crease folding and the shape change propagation proposed in our work, it is important to note that the basic assumptions of curved crease folding do not hold for several reasons. Firstly, we employ soft materials that are extensible in all dimensions, unlike the rigid and inextensible paper sheets assumed in curved crease folding. Secondly, the geometries we work with are not infinitely thin; instead, they have a non-negligible thickness that influences the development and transmission of curvature. Lastly, our chosen manufacturing method of 3D printing allows for the creation of surfaces with both positive and negative Gaussian curvature, whereas curved crease folding assumes a zero Gaussian curvature. Despite these differences, the principle of curved crease folding and the rules governing the transfer of curvature between surfaces is a significant source of inspiration in our work.

2.5 Related Works in Paddling Swimmers

Paddling is a common locomotion strategy observed in various organisms, including the backswimmer [39], frog [57, 33, 19], turtle [51, 63], fruit fly [98], and dog [28]. Numerous studies have examined the use of paddling in human activities such as the breaststroke[118, 22, 46, 123] and canoeing[71]. In these examples, the leg, appendage, wing, or paddle undergoes an asymmetric motion that generates positive average forward thrust and work

on the surrounding medium. Robotic systems have also been developed to mimic paddling gaits, as seen in [115, 56, 66, 88, 94, 87, 31]. However, these approaches typically rely on asymmetric actuation, necessitating designs with higher degrees of freedom and carefully optimized input signals to achieve the desired gait. This can increase system complexity, reduce reliability—especially in underwater applications—and ultimately drive up the cost of the robot.

2.6 Related Works in Soft Twisted Beam Vibration Propagation

Helical shapes, and curved surfaces more generally, are found throughout the natural world. The DNA molecule, a well-known example of helical shape, has been extensively studied [133, 68]. A chirality-creating mechanism has also been observed in the opening of helical-shaped seed pods in Bauhinia variegate [4]. What's more, locomotion from a helical tail shape is understood to be essential in the swimming of human sperm. [32] In the physical world, the self-assembly mechanisms of helical strands has also been studied. [13, 104, 38] Chirality and handedness is also ubiquitous in nature, such as in the snail [103], climbing plant tendrils [40], cucumber tendrils[37], and elegans [10].

Inspired by the chirality and helices in nature, scientists have developed various soft actuators [132, 142, 116, 15] and sensors[126, 95]. These works highlight how chiral asymmetry and helical shapes can be used to generate complex asymmetric locomotion. Other than commonly adopted soft actuators [27] such as pneumatic actuators[131] and jamming actuators [29], etc., some researchers have proposed various soft actuation methods utilizing the stiffness and the geometry change of continuous curved surfaces to propagate and generate working locomotion. Yang et al. [138] present a novel grasping mechanism using a modified kirigami shell. Zhai et al. [140] have developed an origami-inspired mechanism to manipulate the stiffness change of a curved surface to enable grasping and swimming. My previous work [53] has revealed that the local stiffness of the robotic body can be tuned

by altering the geometry of the curved surface and thus the flexure hinges can be developed on demand. Another work [55] from us previously has also presented a paddling like swimming locomotion by propagating the shape change through a continuous curved tubular surface. All the works above inform an important role that the curved geometry plays in the soft robotic system. These works also reveal the idea that the complex locomotion in soft robotic system can be developed by propagating the actuation through a well-designed soft curved structure.

The use of cyclic vibration as a power source for locomotion has been widely adopted in walking robotic systems. In [3], a walking robot has been developed for a tube using elastic fins with a piezo vibration actuator to generate different friction in the forward and backward direction. An insect-scale walking robot actuated by stretchable dielectric elastomers has been developed by Li et al [66]. Bristlebot, another well known simple walking robot example, utilizes vibration actuation and inclined oriented bristles to generate a forward walking locomotion. Extensive studies have been conducted on bristlebots, a thorough study on dynamics of the bristlebots has been presented by Gandra [34], a millimeter-scale bristle robot and its locomotion has also been presented by Kim ea al. [61]. While all the works above validate the capability of using vibration to drive a robot moving in directions agilely, their working legs are all directly linked to the actuators which results in a simple two-dimensional walking gait that is solely related to the actuation input. This deficiency has limited the application of such walking robots to accomplish tasks in rugged and complex environments. In contrast to this limitation, in this dissertation, I propose a novel mechanism to connect the leg and the actuation power source with a soft twisted beam, which introduces more design parameters that can be tuned as well as a more complex three-dimensional walking pattern. As a result, the complex actuation signals typically required to generate a complex walking gait can be ameliorated.

The dynamics of pre-twisted beams has been the focus of many studies in the last 50

years, given its wide application in the propeller blades for helicopters, wind turbines, fans, and turbo-engines. A thorough review of early works up to early nineties was completed by Rosen et al. [100]. These works, though focusing more on reducing the damage caused by twisting, have been instrumental in helping us understand both the static and dynamic models of rigid, pre-twisted beams. Some recent studies shifted the focus toward understanding wave propagation in twisted beams, in order to provide insights on various kinds of waveguides [81, 64]. These studies, while typically looking at nano scales and a higher propagating frequencies, reveal that waves are altered by twisted beams when traveling through them. Twisted structures have also attracted the attention of researchers from the field of robotics. A twisting mechanism has been applied to actuate tendon-based robotic fingers [109]. A twisting tube actuator has also been developed in [67] to exhibit various kinds of forces including contraction, inflation, and deformation.

Chapter 3

RECONFIGURABLE SOFT FLEXURE HINGES VIA PINCHED TUBES

3.1 INTRODUCTION

The purpose of this work is to demonstrate how thin-walled cylindrical tubes can be pinched to create compliant, virtual joints in any radial direction, and then recover their original shape and stiffness once released. Through careful design and material selection, this can result in large changes in stiffness between the original shape, the intended degree of freedom, and orthogonal axes; resulting flexures can then used as passive, compliant rotational joints.

This work is motivated by soft robots, which have received attention in recent years due to their ability to interact with the world in complex ways using simple, continuously deformable structures made with soft materials [101]. Such robots often emulate bio-inspired systems such as snakes [86, 108, 70, 75, 97], octopuses [12, 65, 73, 113], and elephant trunks [96, 83, 137] due to their ability to contort themselves into highly complex shapes that would ordinarily be impossible with traditional rigid robots. This is possible because local curvature in any direction can be induced through the proper mixing of internal actuator forces. However, because of the material-dependent nature of soft-bodied robots, control difficulties can arise due to the high computational cost of estimating pose and optimizing trajectory in redundant, high degree-of-freedom, continuum robots. In order to ameliorate these difficulties while utilizing the natural deformability of soft robots, a great deal of research has looked into tuning the stiffness of soft robots for the purpose of simplifying models and making more efficient controllers [72], including utilizing jamming [143, 135], active elastomers [82], tendon-driven solutions [110], as well as anisotropic [1] and func-

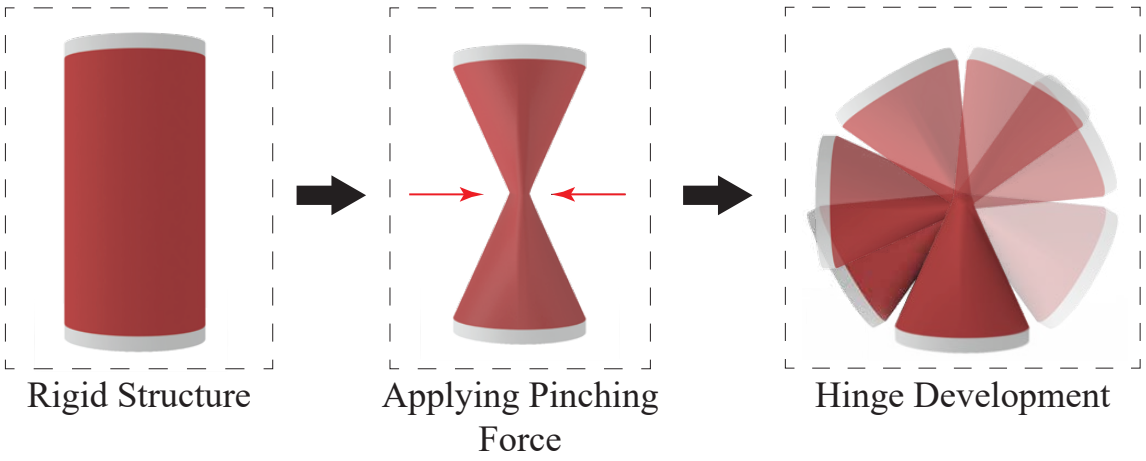

Figure 3.1: **Conceptual rendering of the proposed mechanism.** A cylindrical tube is deformed by pinching, resulting in a flexure hinge that can rotate when a load is applied at the end.

tionally graded materials [8].

Tuning the shape or curvature of soft devices has been studied for its ability to alter system stiffness. Nguyen et al. highlight how curvature-change can modulate the stiffness of fish fins [84], while Pini et al. detail how internal stress fields can impart stiffness changes in thin sheets via two-dimensional bending [91]. This can be enhanced by weakening or creasing material along a curve to produce rapid transitions between static states in curved soft materials [9]. Curvature and shape change may also be actively controlled for the purposes of changing stiffness [134]. Some compact examples include the use of SMA tendons [62] and springs [112].

Across the various research which has been performed in this area, the majority focuses on how the design and placement of internal actuation within continuum manipulators impacts arm state and end effector configuration via multiple actuators [86, 108, 70, 75, 97, 12, 65, 73, 113, 96, 83, 137, 18]. Altering stiffness has previously been accomplished through numerous approaches [72, 143, 135, 82, 110, 1, 8], but within the body of work focusing on

curvature-influenced stiffness, papers focus on mechanics or stability analysis [84, 91, 9] while others use one degree of actuation to stiffen or soften a geometry [134, 62, 112]. In contrast with these studies, this work investigates how combining the forces of more than one actuator can influence the creation and orientation of flexure hinges in tubes, and how, with proper geometry and material selection, those hinges can then passively or actively revert back to a stiffer tubular structure. These devices, if properly implemented in continuum devices, could permit soft robots to utilize simpler models akin to their rigid counterparts while retaining the benefits of soft robots.

In order to realize this concept, we propose to change the local surface curvature of thin-walled tubes in order to alter local bending stiffness; in this way local buckling makes the tube's altered mechanical properties suitable for use as a flexure hinge about the buckled region. We believe this novel soft hinge, shown in Fig.3.1, fits within a larger class of kinematic elements which we call Soft, Curved, Reconfigurable, Anisotropic Mechanisms, or SCRAMs. Like the bio-inspired mechanisms mentioned above, SCRAMs are capable of re-configuring the stiffness of curved surfaces for use as virtual joints in soft robots. The proposed SCRAM mechanism in this work re-configures its internal stiffness through the application of opposed pairs of pinching forces (via actuated pairs of tendons) on the surface of the tube. By controlling the distribution of forces exerted through the tendons, this SCRAM device is able to flatten the tube in different radial orientations, permitting one to select the hinge's axis of rotation on demand. In doing so, the concept proposed in this work extends prior work mentioned above, enhancing the usability of stiffness tuning mechanisms for more complex applications such as robotic arms and snake-like robots. Furthermore, in contrast to prior work, which uses shape change in soft systems directly for actuation purposes, our approach uses shape change and reconfiguration indirectly, for the purpose of reducing system stiffness about a desired hinge axis. Actuator forces are directed orthogonal to system outputs, minimizing their contribution to work done at the

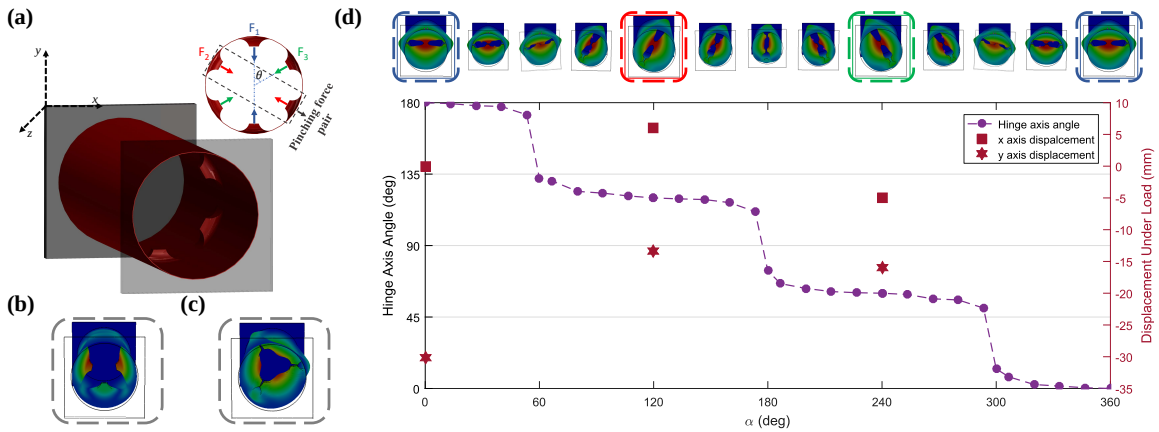

Figure 3.2: **Finite element analysis on a pinched tube.**(a) The tube design in SolidWorks with inset of the cross-section at the midpoint. (b-c) Some tendon configurations fail to create a hinge, including (b) two pairs of pinch forces ($\theta = 90°$) and (c) three pairs of equivalent, radially symmetric pinch forces ($\theta = 60$). (d) FEA results showing the change in the hinge axis for different combinations of pinch forces as well as the displacement of the end effector when the tube is first pinched and load is subsequently applied.

end effector – an advantage for sizing future shape change actuators, which we discuss in the conclusion.

In the following sections, we discuss the principle of operation for the proposed mechanism, using finite element analysis (FEA) to understand the relationship between distributed pinching forces, curvature, and system stiffness. We then propose a set of criteria to evaluate the performance of the mechanism and experimentally validate the concept with a benchtop prototype. We then analyze and compare the stiffness change between pinched and unpinched tubes, and provide insights as to the impact of our work and future research directions.

3.2 FEA Modeling

In this section, we validate the efficacy of the proposed mechanism by conducting a Finite Element Analysis (FEA) study on a cylindrical tube with 0.1 m radius, 0.3 m length, 0.001 m wall thickness and 2.96 GPa stiffness. Using FEA, we seek to demonstrate that a pair of opposing collinear forces exerted on a tube results in a highly deformed section of the tube's body and significantly lowers stiffness in comparison with an undeformed tube. In addition, we study the ability of a finite number of pinching forces to orient the major axis of deformation through 360°. Finally, we analyze the behavior of the pinched tube under various loading conditions.

The analysis is performed using SolidWorks Simulation; small modifications have been made to the tubular geometry in order to better localize constraints and force application points. In order to constrain the tube's circular cross-section at its proximal and distal ends, two rigid prismatic parts are merged with the tube's geometry. In order to provide pinching sites on the surface of the tube, small prismatic geometries are added to the interior of the tube halfway along its length. Fillets are used to transition between geometries to avoid part failure in these particular regions. The resulting geometry can be seen in Fig. 4.4(a).

The first analysis uses a nonlinear, static approach to model the interaction between pinching forces and tubular deformation. The mesh is created with 'Curvature-based mesh' elements with a minimum and maximum sizes of 2.7 mm and 8.1 mm, respectively, resulting in around 30200 nodes in the model. Our approach begins by determining the force required to completely pinch a tube until its sidewalls(or the added prismatic geometries) touch. This results in a weak section in the tube body (that is more conducive to bending like a flexure hinge). Figures in red, blue, and green circles in Fig. 4.4(d) show one pair of pinching forces deforming a tube till its interiors meet. This confirms the possibility of producing a nearly flat section in the tube while meeting the experimental result in

Fig. 3.5(b).

When a pair of equal and opposite collinear pinch forces are applied to each side of the tube, the maximum deformation falls along a line that is orthogonal to the pinch force vectors (Figures with red, blue, and green circles in Fig. 4.4(d)) and the radial axis of the tube. We hypothesize that by combining multiple sets of force pairs, the orientation of this axis can thus be controlled to influence the resulting hinge orientation. Thus, our model has been augmented with multiple pairs of pinching forces, separated by an angular spacing θ of

$$\theta = \frac{360}{2n} \tag{3.1}$$

where n is the number of pinching unit pairs embedded in the tube.

Based on the above design assumptions, with two perpendicular unit pairs of pinching forces ($\theta = 90^\circ$), our FEA reveals that the simultaneous actuation of the units, even at different force levels, does not result in a roughly elliptical cross section with a single major axis. Rather, the pinching forces create the dimpled-looking deformation seen in Fig. 4.4(b), with two independent, simultaneous perpendicular sets of major and minor deformation axes that we liken to a singularity consisting of multiple solutions.

A mechanism with three pairs of pinching units is subsequently studied. In this design $\theta = 60^\circ$. The result, seen in Fig. 4.4(c), shows that simultaneous actuation of all three pairs at the same force magnitude results in the same dimpling as in the case of $n = 2$, with no clear major axis of deformation. Actuating only two of the pairs at a time, however, results in the tube deforming without multiple simultaneous solutions, which looks like the results for the case of a single pair of pinch forces.

In order to further study the effect of pinching forces on the tube's deformation axis,

we define the following formulation for defining individual pinching forces:

$$F_{i1} = F_{i2} = F_p \cos(\beta) \tag{3.2}$$

$$F_{j1} = F_{j2} = F_p \sin(\beta) \tag{3.3}$$

$$F_{k1} = F_{k2} = 0 \tag{3.4}$$

where $i, j,$ and k correspond to the index of a pair of pinch forces, and F_p, and β relates to the magnitude of the force required to flatten the tube and pinch force distribution angle, respectively. Using the above equations, we separate the overall magnitude of the pinching force from its angle throughout the study. This allows us to focus on its direction change as function of β. We then introduce α to parameterize the change in pinch force pairs and the force distribution throughout 360°:

$$\beta = \begin{cases} 0.75\alpha & \text{for} \quad 0^\circ \leq \alpha < 120^\circ \\ 0.75(\alpha - 120^\circ) & \text{for} \quad 120^\circ \leq \alpha < 240^\circ \\ 0.75(\alpha - 240^\circ) & \text{for} \quad 240^\circ \leq \alpha < 360^\circ \end{cases} \tag{3.5}$$

$$(i, j, k) = \begin{cases} (1,2,3) & \text{for} \quad 0^\circ \leq \alpha < 120^\circ \\ (2,3,1) & \text{for} \quad 120^\circ \leq \alpha < 240^\circ \\ (3,1,2) & \text{for} \quad 240^\circ \leq \alpha < 360^\circ \end{cases} \tag{3.6}$$

The radar plot in figure 4.4(d) demonstrates how the major deformation axis can be affected through proper distribution of tension across the three tendon pairs. The inset renderings around the outside of the radar plot show the tube's deformation as a function of α. At $\alpha = 0^\circ, 120^\circ, 240^\circ$, tendon tension F_p is concentrated on just one tendon (blue, red, and green, respectively), and for all other values of α, the tension is shared between tendon pairs i and j. The resulting axis angle can also be seen to increase monotonically as a function of α (violet circles in the interior radar plot), though rapid transitions can be

found around $\alpha = 60^\circ, 180^\circ,$ and 300°. At these three values of α, F_p had to be increased by 50% in order to fully pinch the tube. We believe that this is caused by errors in the numerical solution at these particular values, potentially due to the geometries added to aid simulation. Future work will help to clarify this result as discussed in the conclusions.

Once the tube is deformed, FEA can also be used to study the flexure hinge's behavior under load. This is done by performing a nonlinear dynamics study. In this study the pinching forces are initially applied as before; once the tube deforms, a load is subsequently applied in the negative y direction to the top surface of the prismatic geometry attached to the distal end of the tube. The displacement of the prismatic block attached to the distal end of the tube in x and y axes are reported in Fig. 4.4(d) using squares and stars, respectively, for $\alpha = 0^\circ, 120^\circ, 240^\circ$. For $\alpha = 0^\circ$ (a horizontal hinge axis), the x displacement is zero and y displacement is maximized. For values where the loading direction is not orthogonal to the hinge axis, the displacement of the distal end of the tube qualitatively corresponds to the orthogonal of the resulting hinge axis vector (as seen in the attached video).

3.3 Prototyping

3.3.1 Material Selection

This section provides details about the fabrication of experimental prototypes used to validate the concept described in the previous section. The suitability of each prototype is evaluated by a set of three criteria: (1) the force required to pinch the tube, (2) the ratio of radial stiffness anisotropy at the flexure hinge, and (3) the ability of the tube to recover its original shape without plastic deformation after forces are removed. Since the proposed mechanism is eventually intended to be used for mobile robotic applications, the servo selected for prototyping and experimentation was small, with a stall torque of 4 Nm, constraining the maximum pinch force we could use to deform prototype tubes. While it

would be desirable to select designs that simply minimize the force required to create local deformation (criteria 1), the use of softer materials or thinner cylinder walls could lead to failure of the second criteria, which considers the ability of the flattened tube to act like a flexure hinge; this is an essential characteristic of our proposed mechanism so that hinges flex when loaded about the hinge axis yet remain stiff to orthogonal loads. The higher the stiffness ratio between these two directions, the better the hinge. The third criteria considers the ability of a design to passively recover its tubular shape without damage – essential if this mechanism is to be used repetitively in the context of robotics applications. We know from basic mechanics principles as well as texts like [60] that thinner cylinder walls, larger diameters and lower Young's modulus will lower system stiffness and permit easier pinching, but will also limit the maximum stiffness of the system for resisting deformation in unintended directions.

We selected a number of different cylindrical tubes made from thermoplastic polyurethane (TPU), polyethylene terephthalate (PET), and latex rubber (Shore hardness 35A). Looking first at the latex rubber tube, a number of drawbacks can be observed.

Although it can be deformed by a pinch force of 10 N (criteria 1) and is good at recovering its shape without damage (criteria 3), the flexure hinge created when the tube is pinched exhibits little difference in stiffness when bent in its intended orientation and a direction orthogonal to it. This is due to the thick cylinder wall needed to sufficiently stiffen the tube, indicating that the Young's modulus of the latex rubber makes it unusable for this particular SCRAM device, as it functions poorly as a simple joint (criteria 2).

PET on the other hand, is a semi-rigid, elastic material widely used for soda and water bottles; at 180 mm length, 72 mm diameter and 1 mm wall thickness, it can be deformed into a pinched tube while maintaining the ability to sustain a high degree of rigidity in directions orthogonal to pinching while easily rotating about its flexure hinge (criteria 2). An example of this tube is shown in Fig. 3.3(a). However, a number of drawbacks were

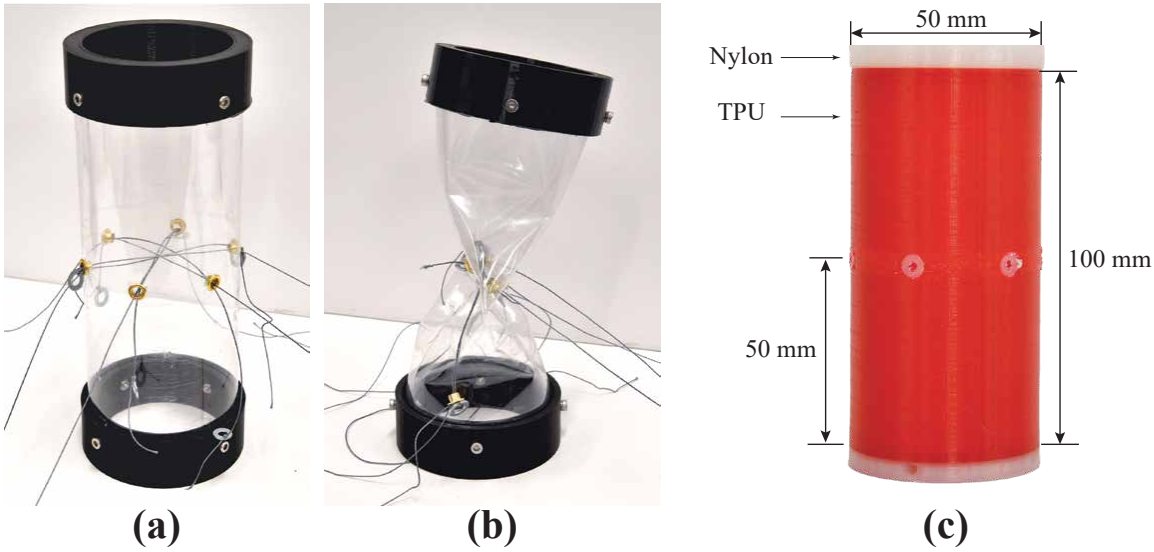

Figure 3.3: **Prototypes made from different materials.** **(a):** PET prototype. **(b):** PET prototype after deformation. **(c):** TPU prototype specifications.

observed while testing the PET tube. First, the force required to pinch the material is relatively large, which violates criteria 1. Moreover, due to the nature of the PET, some scars were created on the tube's surface which were visible after recovery, indicating high stresses had plastically deformed the material during its use as a joint, violating criteria 3. Furthermore, as shown in Fig. 3.3(b), the PET tube did not passively recover its shape, but required an external force to initiate recovery. While a thinner cylinder wall would reduce stiffness and potentially lower the local stresses that led to that plastic deformation, samples in the desired dimensions were not readily available; for these reasons the PET tube was abandoned as a suitable alternative.

TPU possesses high elasticity and high sheer strength properties, and has been broadly used in fabricating soft robots [2, 121]. In terms of its suitability as a SCRAM hinge, the pinching force required to deform TPU is lower than PET (criteria1). When pinched, the TPU tube exhibits high compliance in the intended direction of hinge motion compared to a relatively stiff behavior in other directions, making it highly suitable with regard to criteria

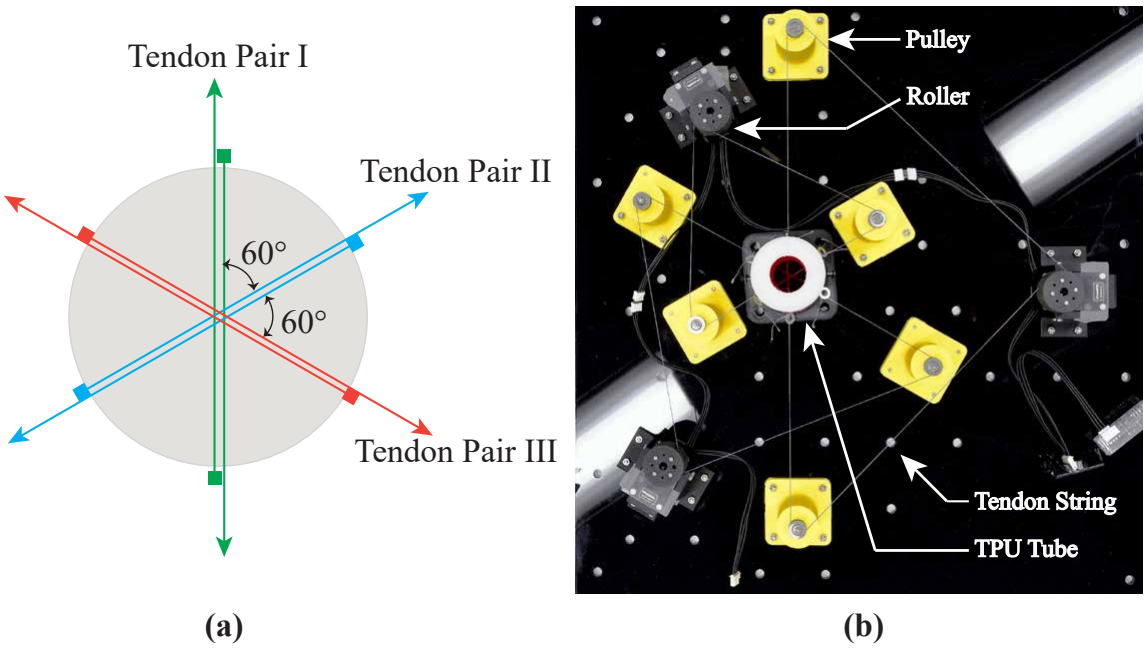

Figure 3.4: **Test setup and tendon configuration.** **(a):** Tendon string orientation. **(b):** Prototype with servos and pulleys.

2. In terms of recovery, the high elasticity of TPU also permits full, unaided recovery from its flattened state without any visible scarring (criteria 3). Additionally, because it is compatible with 3D printing processes, its shape can be adjusted and reprinted as more is learned about its performance. Owing to these merits, TPU was adopted as the material for subsequent prototypes and experiments.

3.3.2 Prototyping

The main body of the current prototype, shown in Fig.3.3(c), is 3D printed from TPU92A produced by Ultimaker [1]with an Ultimaker S5. The geometry of the tube (100 mm long, 50 mm diameter and 1 mm wall thickness)was primarily constrained by the printing capability of our printer, the size of our testbed, and the force limits of the tendon-driven

[1]Ultimaker TPU 95A

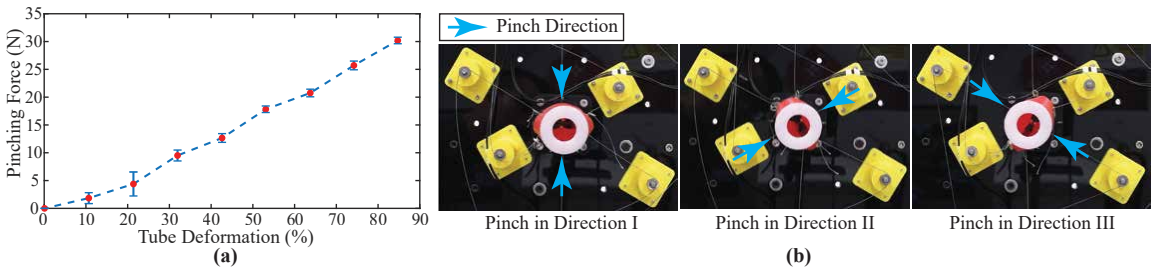

Figure 3.5: **Pinch force and the corresponding deformation. (a):** Pinch force required to reach specific tube deformation. **(b):** Pinch in three different directions with 60^o radial spacing and the hinge developed correspondingly.

actuation system.

Though this geometry was not optimized against a set of quantitative performance criteria, it was observed to qualitatively satisfy each of our stated criteria within the limitations of available materials, printing, and testing capabilities. Two rigid nylon attachment plates were co-printed to the bottom and the top of the cylinder, and six round metal grommets were radially distributed around the length midpoint of the body so that tendons could pass through the tube without cutting or abrading the material.

In order to show the potential for controlling the orientation of the resulting soft flexure hinge, this prototype is actuated using a tendon-based system to impart three separate pinching forces around the circumference of the tube. Six tendons are routed individually through one of the grommets and then routed and connected to one of three Dynamixel XM430-W350-T servos through a system of pulleys attached to ground, making it possible to symmetrically drive a pair of tendons from one servo so that three equal and opposite pairs of pinch forces may be individually applied to the tube at 60° radial spacing, matching the arrangement of the FEA simulation. The tendon distribution and the final test setup may be seen in Fig. 3.4(a) and (b) respectively. The pinching force and the amount of tube deformation are measured by the torque and the position of the servo.

3.4 Pinching Force V.S. Tube Curvature

The relationship between pinching force and tube curvature is discussed next. We approach the problem both to understand the relationship between pinching force magnitude and the amount of deformation, as well as to understand the relationship between the distribution of pinch forces across the tendons and the resulting flexure hinge's orientation.

3.4.1 Pinching Force V.S. Deformation

To understand the relationship between pinching force and tube deformation, we have measured tendon force at sample positions via Dynamixel servos. This test has been conducted with the servos operating in position control mode, wherein the servo's embedded controller applies a control signal to drive the servo to a goal position, which is tracked internally. By actuating the servo to pull the tendon a certain length, the surface of the tube correspondingly deforms.

In our test, the servo starts from a position corresponding to a fully undeformed tube, and increments by a small amount until the final tendon displacement equals the radius of the tube. The servos' position and current are recorded at each increment. Tendon tension is then calculated by recording the motor current at each step and calculating the tendon forces as a function of both the current/torque curve provided by the manufacturer[26] and the radius of the output pulley. Because each tendon is routed through a minimum number of pulleys, we assume that the majority of the current applied by each motor is transmitted into a pinching force rather than lost within the tendon system itself. The relationship between pinching force and the tube's deformation can be seen in Fig. 3.5(a). By controlling the magnitude of the pinching force, a specific amount of deformation can be established in the tube that is qualitatively consistent with our FEA results.

3.4.2 P

inching Force Distribution vs. Deformation To understand the relationship between the orientation of the pinching force and the direction of the deformation, we conducted another set of experiments, pulling different tendons aligned along different orientations in order to generate pinching forces in different directions. This was accomplished by commanding the servo (in position control mode) to pull the tendon so that appropriate pinch forces were generated to deform the structure, similar to the FEA analysis discussed in Section 3.2. As can be seen in Fig 3.5(b), the orientation of the flexure hinge changed as a function of tendon force distribution. This result also qualitatively matches with the results seen in Fig. 4.4(d) and discussed in Section 3.2.

Based on the aforementioned tests, the relationship between the pinching force and the curvature generation can be better understood. The magnitude of the pinching force is positively correlated to the flattening of the tubular structure, and the direction of the curvature depends on the orientation of the pinching force.

3.5 Evaluation of the Flexure Hinge

In this section, we evaluate the performance of the flexure hinge generated by pinching, examining joint stiffness as well as its directional displacement when loaded with with forces in varying directions.

3.5.1 Bending Stiffness Analysis

This section deals with changes in tube stiffness due to pinching. The experimental setup is shown in Fig. 3.6(a). In this test, a linear stage pushes a contact point parallel to the ground while an ATI Mini40 six-axis force-torque sensor records the forces. This was conducted over multiple trials for different displacements in both the pinched and un-

pinched configuration, as shown in Fig. 3.6(b). To better understand the difference in stiffness due to pinching, we compare the slopes of the linear regions between the pinched and unpinched states. As shown by the slopes of each linear fit, as seen in Fig. 3.6(b), the difference between pinched and unpinched configurations results in a dramatic stiffness change from $k_1 = 1812\,N/m$ to $k_2 = 148.6\,N/m$; in other words, the stiffness of the unpinched tube is 12 times stiffer than the pinched tube.

Figure 3.6 also shows that the load increases linearly as a function of forward displacement in both the pinched and unpinched configuration. Linear behavior can also be observed when moving backward, though hysteresis is present. It can be seen that the pinched configuration exhibits much more hysteresis, which we can attribute to several factors. First, because the displacements for the pinched experiment are generally larger, viscoelastic creep due to our material selection may be amplified and more noticeable. As discussed previously, TPU has been selected for its ability to recover without noticeable plastic deformation, but it may not be an ideal material in other ways. Hysteresis may also be caused by the fact that the inner surfaces of the tube may slide against each other when the system is fully pinched, which can lead to frictional losses and a new static equilibrium after bending. This is supported by the fact that after larger displacements, the tube did not fully recover while still in its pinched state; After tendon tension was relaxed and the tube recovered its initial shape, however, its performance when pinched again exhibited the same linear behavior across repeated tests.

3.5.2 Alignment of Forces, Hinge Axes, and Resulting Displacements

To validate the suitability of the flexure hinge to perform as a revolute joint, we orient the test setup so that the tube's radial axis is perpendicular to the ground. A 500 g weight is attached to the end of the structure. The servo is then commanded in velocity mode to fully pinch the tube at a constant speed. The tendons parallel with the gravity vector are actuated

in the first example, so that the resulting flexure hinge is perpendicular to the gravity vector. In order to eliminate the effect of the unpinched tendons, the other servos are driven so as to keep those tendons slack.

During this test we observe that as the tendon force increases, the tube's curvature changes, and the structure gets visibly weaker until it buckles, demonstrating a drastic change in stiffness around a newly created hinge. This procedure is shown in the supplementary video.

Two other tests have been conducted to demonstrate that the hinges generated using this concept behave similarly to a formal revolute joint, which is commonly used in robotics to provide rotation about a single-axis. In these two tests, we actuate the other two pairs of the tendon individually so that the pinching force is applied in two different directions at an angle of $\pm$ 60° relative to gravity. As before, a load of 500 g is attached to the end of the structure and the servos are commanded to to pinch the tube at a constant speed. As can be seen in Fig.3.7(a), the structure deforms as the tendon is pulled to its limit. Since the orientation of the resulting hinge varies, the direction of the end-effector's motion about the hinge axis changes concurrently in response to the same load.

3.6 Shape Recovery of the Flexure Hinge

As an essential part of hinge reconfiguration, we study the recovery of the flattened tube back to its circular cross-section. During the tests introduced in Section 3.5.A, we found that the tube was able to passively recover its shape under 500 g load when the pinching force was removed. This is due to the stiffness, geometry, and the elastic nature of TPU. This result also validates the shape recovery requirement of our selection criteria.

The tube was also evaluated at a load of 1000 g. In this case, the TPU was unable to passively recover without aid. Instead, an active strategy was used. The two tendons exerting pinching forces were first released and the other two pairs of pinch tendons were

lightly actuated to pinch the tube antagonistically in other two directions. This resulted in the tube regaining its tubular shape under load, as can be seen in Fig. 3.7(b), as well as in the supplementary video.

3.7 Conclusions and Future Work

This dissertation introduces a novel concept for tuning the stiffness of a thin-walled tube by altering the local surface curvature through pinching. Its intellectual contributions include (i) a physical implementation of this concept, (ii) understanding and evaluation of the relationship between the pinching force and the tube deformation supplied both by FEA and experiment; (iii) insights into how the combination of multiple pinching forces can be used to orient the major axis of deformation and resulting flexure hinge, demonstrated in FEA and experiment (iv) experimental evaluation of the suitability of the resulting hinge for use as a joint including its stiffness and displacement under load, and (v) prototype-based validation of active and passive shape recovery of the tube.

Future work will mainly focus on actuation, sensing, and applications of the proposed concept. To begin with, a better normalization of our FEA model will permit a more uniform distribution of tendon forces to increase consistency of deformation and hinge performance throughout 360°. This will lead to a better understanding of how our design parameters can improve system performance in order to use multiple hinges as a system. Our aim is to permit more complex, reconfigurable mechanisms such as robot arms and snake-inspired designs. We will also look into ways to improve the systems for pinching and actuating the hinge. As can be seen in Section 3.3 B, although the tendon based actuating system used in the test setup can effectively pinch the tube and verify the principle of operation, in its current state is too complex and bulky for applications outside of an experimental test bed, if we wish to integrate multiple SCRAM stages together, for example. This drawback motivates us to search for and develop more portable and simpler actuating

systems that can effectively pinch and actuate the hinge. We believe our approach of actuating internal shape and stiffness change (rather than end-effector motion), in conjunction with additional materials and geometry optimization, will eventually permit lower-power and more compact actuators to be integrated within the tubular system itself. New methods to sense local deformation will also be necessary in order to close the loop and actively control shape change in future SCRAM devices.

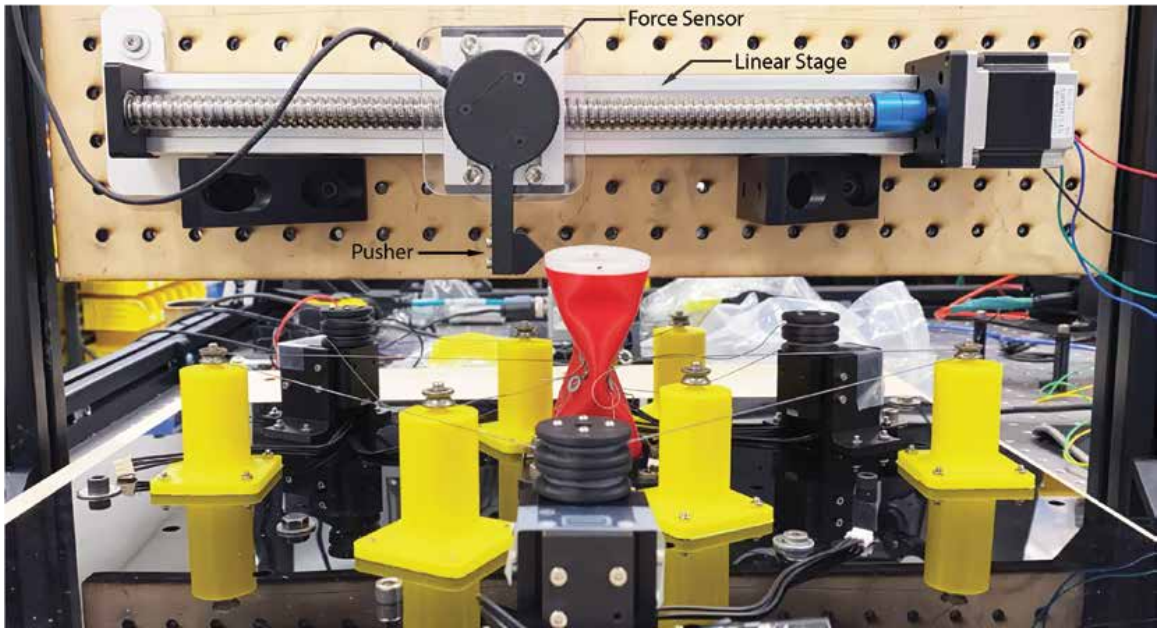

(a)

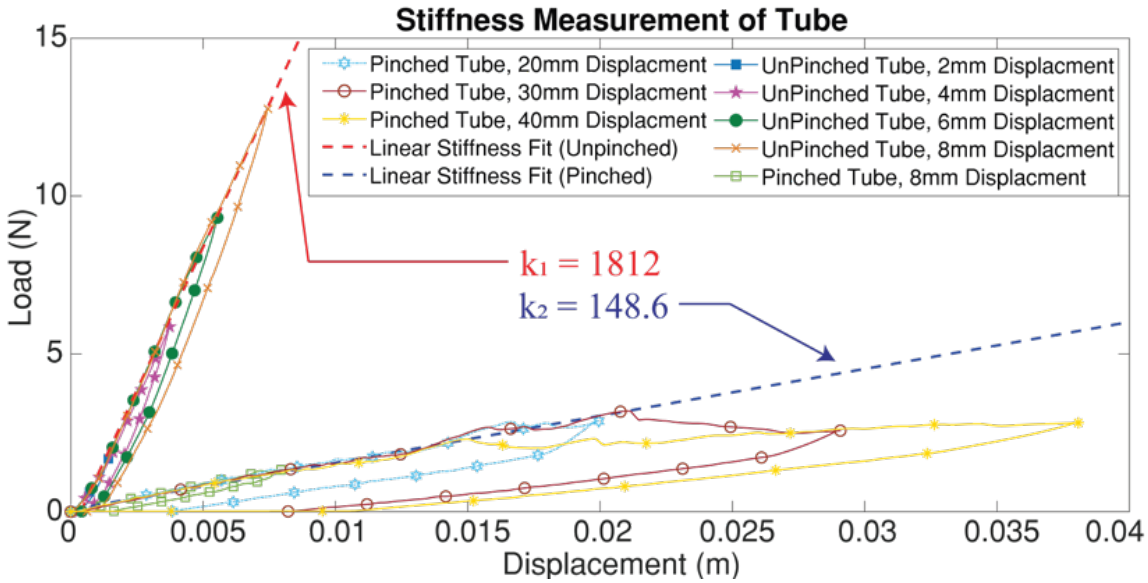

(b)

Figure 3.6: **Bending Stiffness Analysis. (a):** Test setup including linear stage, force sensor, and pusher. **(b):** Bending Stiffness comparison for pinched and unpinched tube.

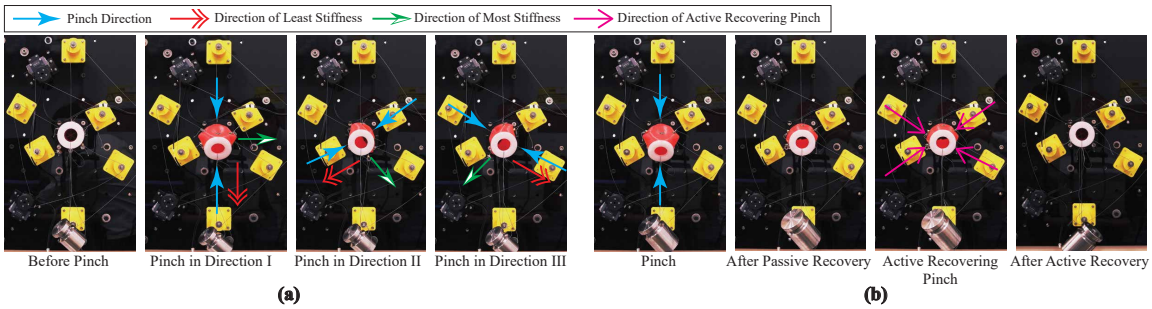

Figure 3.7: **Creation of flexure hinges and subsequent recovery. (a):** Deformation of tubes under 500 g load with differing hinge orientations. **(b):** Recovery of tubular shape (under 1000 g load) using active and passive approaches.

Chapter 4

SHAPE CHANGE PROPAGATION THROUGH SOFT CURVED MATERIALS FOR DYNAMICALLY-TUNED PADDLING ROBOTS

4.1 Introduction

While the field of soft robotics has led to a number of recent innovations in tuned-stiffness materials, less work has been done on the role curvature can play in tuning locomotion dynamics in soft systems. This work investigates a concept of using connected, curved, soft surfaces to transmit actuation effort and tune the directional stiffness of appendages in underwater swimming. This shape propagation concept leverages the mechanics of materials and studies the impact that curvature can have on the ability to transmit shape change between two different surfaces of a soft body in order to simplify the power delivery and control signals required for locomoting soft robotic systems. This has led to the development of a soft tubular device that adopts the proposed shape propagation concept that can generate forward net thrust and positive work on the underwater environment over a gait cycle. As seen in Fig. 5.1, the proposed device transmits the deformation of a central tube to two connected curved fins to produce an asymmetric paddling stroke in which the anisotropic stiffness of curved surfaces is leveraged to preferentially buckle the system in one direction. Furthermore, this device can be 3D printed in a single step without any assembly, through its integration of a revised pneu-nets pneumatic actuator.

Paddling is a locomotion strategy commonly found in organisms such as the backswimmer [39], frog [57, 33, 19], turtle [51, 63], fruit fly[98] and dog[28]. A number of studies have shed light on the use of paddling in human activities such as the breaststroke[118, 22, 46, 123] and canoeing[71]. In these examples, the leg, appendage, wing, or paddle

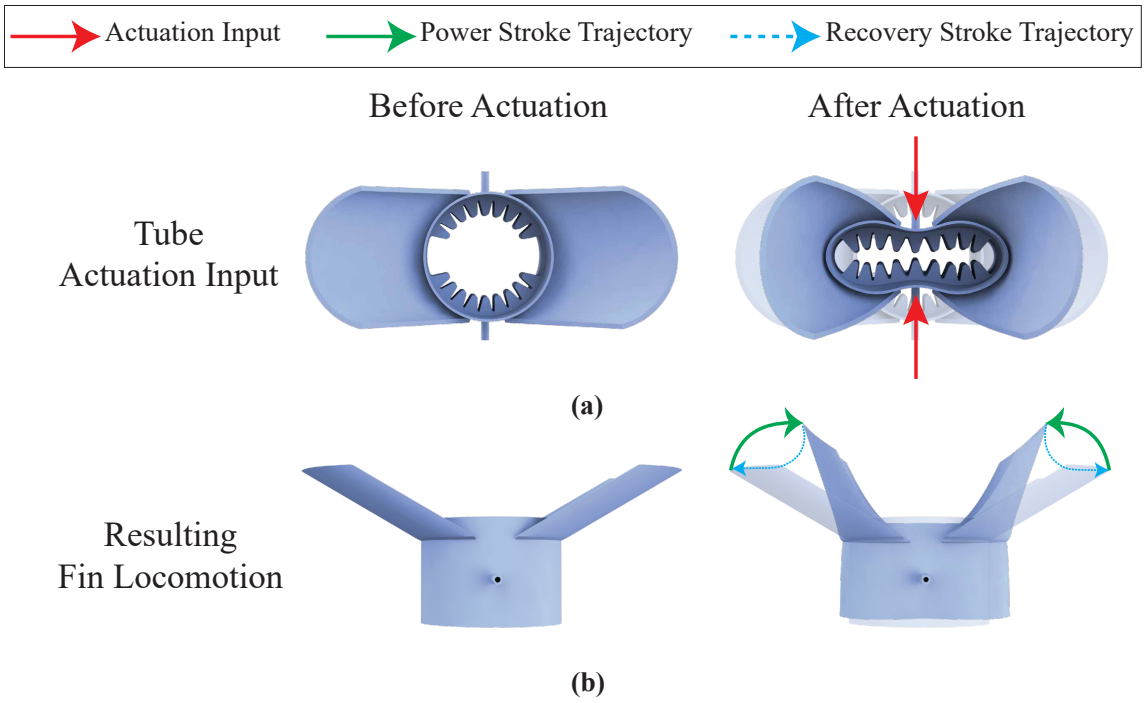

Figure 4.1: **Conceptual rendering (a):** Conceptual rendering of the tube actuation input. **(b):** Conceptual rendering of the resulting locomotion on the side fins.

moves through an asymmetric motion that generates positive average forward thrust and positive work on its surroundings. Robotic systems have also been developed that replicate paddling gaits, such as [115, 56, 66, 88, 94, 87, 31]. However, these approaches typically rely on asymmetric actuation, requiring higher degree-of-freedom designs with carefully-optimized input signals to form the desired gait. This can impact resulting systems by increasing complexity, reducing reliability – especially in underwater applications – and ultimately driving up the cost of the robot. In contrast to this surveyed prior work, we seek in this work to produce positive forward thrust using an asymmetric paddling gait via one symmetric actuation input. This is realized by tuning the stiffness of our system fin to alter the fin critical buckling limit during the paddling cycle.

To alter the curvature of thin sheet structures, a technique called curved crease folding has been well studied and used within origami, the art of paper folding. Curved crease fold-

ing uses the principle of a curved paper crease to establish and propagate curvature across two connected developable surfaces. This principle has been studied computationally [49, 25, 59, 78, 35] as well as applied to the field of graphics [23, 117], architecture[117], and robotics[79]. Curved crease folding traditionally observes a number of rules that help simplify the analysis of how curvature-based relationships are established, including the assumption of rigid and inextensible paper sheets that are infinitely thin. Combined with the assumption of flat-foldability, this assumes that gaussian curvature of curved-crease geometries must remain zero. Although curved crease folding shares some common features with the concept proposed in this work, these basic assumptions do not hold for several reasons. First, we use soft material that is extensible in all dimensions. Second, the geometries utilized in this work cannot be considered to be infinitely thin, and plays a role in the development and transmission of curvature. And finally our selected manufacturing method of 3D printing permits the generation of surfaces with both positive and negative Gaussian curvature. Nevertheless, the principle of curved-crease folding, and the rules which govern the transfer of curvature between surfaces, is a significant source of inspiration in this work.

Prior work has established that directional stiffness of a thin curved sheet can be changed by tuning its curvature [91]. This concept has been extended to soft tubular structures, in which the stiffness can be tuned by altering the tube's curvature; this has been validated using FEA and experimental approaches[54]. The mechanics of buckling and "snap-through" in curved shells has also been studied [9]. Buckling, as a principal mechanism, has been found to effectively generate locomotions in flagella[129], Venus flytraps[130, 74], and ladybird beetles[102].

Tunable stiffness permits the occurrence of anisotropic buckling, which eventually results in an asymmetric paddling gait, which has also been studied in our previous work[105], in which a new concept to generate forward thrust was proposed; by taking advantage of the nature of curved beams to preferentially buckle under loads, this concept demonstrates

how, using symmetric actuation signals, the complexity of input signals can be reduced in comparison to alternative robotic paddling swimmer designs. In this work, we have adapted the same concept to simplify actuation complexity. Like the previous work, the fin used in this work is pre-curved so that it possesses similar asymmetric stiffness and critical buckling limits; this creates a controllable, hysteretic paddling gait under certain symmetric actuator signals. Differing from the previous work where the curved beam is rigidly attached to an actuator and establishing a 1:1 relationship between a motor and its output, in this work, we are interested in utilizing the curvature change as a source of the actuation to permit the actuation transmission from pinching the tube to the paddling of the fin.

The contributions of this work are: (i) Developing a 3D printable soft tubular swimming device that utilizes the concept of curvature propagation and anisotropic buckling to produce an asymmetric paddling gait via a symmetric actuating input. (ii) Establishing a dynamic model for the proposed device to reveal the role inertia and drag play on anisotropic buckling, hysteresis behavior, and asymmetric paddling gait. (iii) Showing how a 3D printable pneu-nets based actuator can be adapted to pinch the tube.

4.2 Concept of Operation

In this section, we introduce the operational concept of the proposed device. This idea is based upon three main assumptions. The first assumption is that pneumatic, bellows-style actuators mounted on the inside of a tube may be used to pinch and deform a tube radially, as illustrated by the red arrows in Fig. 5.1a. The second states that curvature changes due to the tube's deformation may be transmitted via the principles of continuum mechanics to distally-attached curved surfaces such as the attached fins seen in Fig. 5.1b, causing these surfaces to be swept inward closer to the tube while changing curvature in the process. The third assumption is that this sweeping motion and curvature change can be used to create paddling gaits, as indicated by the green and blue arrows in Fig. 5.1b. Asymmetric

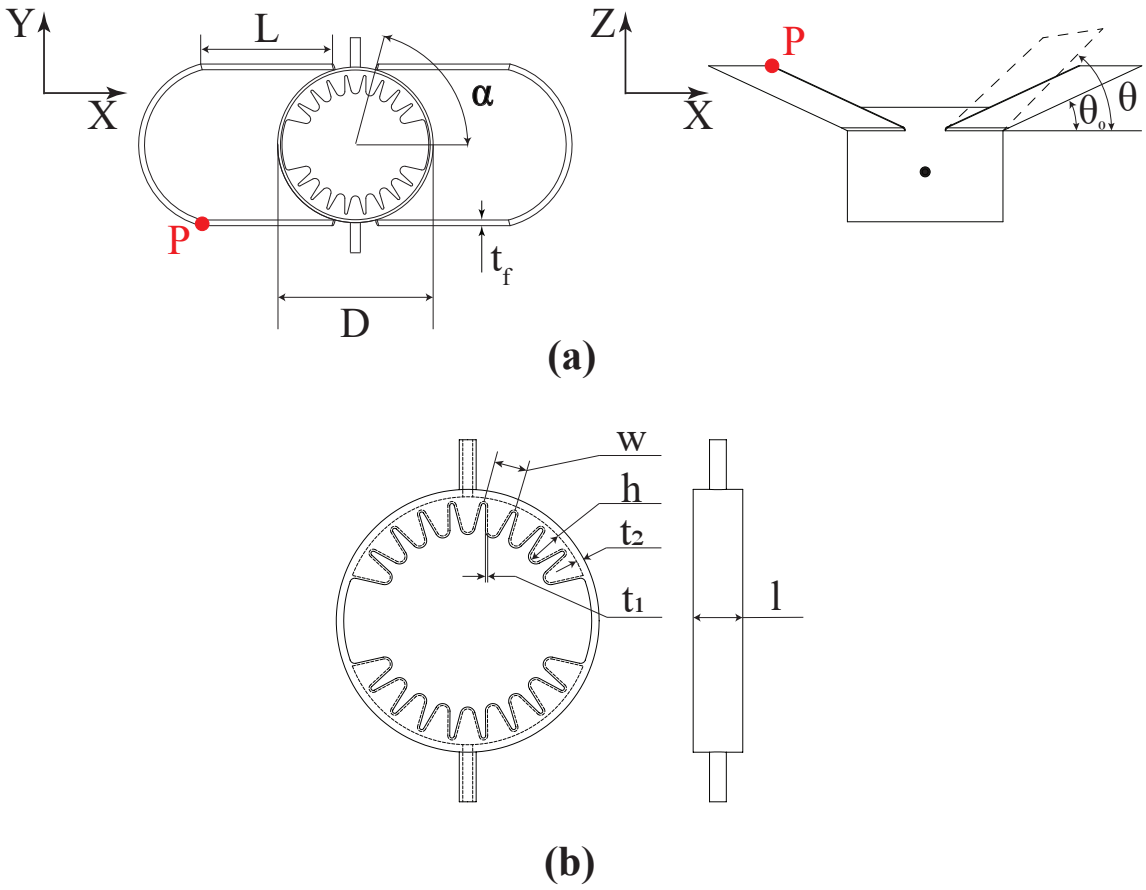

Figure 4.2: **Design variables (a):** Design variables of the swimming device. **(b):** Design Variables of the pneumatic actuator.

paddling is caused by the anisotropic buckling behavior of curved fins, which, as mentioned in the introduction, establishes a non-reciprocal motion trajectory for the fin that generates nonzero net thrust over a full gait cycle. This assumption is further supported by prior work on buckling curved beams[105], which we extend in this work by demonstrating how tuning the drag and inertia of such systems can alter the hysteresis observed in order to perform positive net work in underwater locomotion applications.

This work seeks to validate the aforementioned assumptions and demonstrate how, when connected together, the effects of propagated curvature, nonlinear stiffness, and buck-

ling can be tuned to establish and improve forward thrust and motion generation in this device. This is done in the design process by tuning several parameters, such as those seen in Fig. 4.2. Some parameters influence the overall stiffness of the tube-fin system, such as the tube wall thickness t_2, the tube diameter D, the fin thickness t_f. Other parameters, such as the actuator wall thickness t_2, the actuator chamber width w, the actuator chamber height h, and the actuator chamber length l, are responsible for establishing the force generation capabilities of the pneu-nets actuator. Other variables, such as the fin arc length (α) and the fin attachment angle (θ) define the geometric connection between the tube and fin and establish the travel and curvature-change relationships between the two surfaces. It should be noted that the initial radius of curvature of the tube and fin are set equal to each other in this study. Other variables seen within the plot in Fig. 4.2 assist in tracking and measuring displacement and deformation. These include the point P, whose motion along different axes can be used to describe the change in curvature as well as the total travel of the fin. We thus introduce y, which tracks the displacement of P along the Y-axis; this value increases as the curvature of the fin increases. The travel of point P in the X-Z plane is measured by s; the higher the value of s, the greater the travel from P's neutral position, indicating a higher range of motion.

4.3 Validating Assumption I: Pneumatic Tube Pinching Actuator

The first assumption is validated in this section through the development of a bellows-style pneumatic actuator that can be mounted inside a soft tube to flatten it along a desired axis. In previous work [54], a tendon-based, servo-driven actuation system was developed to pinch and radially deform a soft tube in multiple directions. That approach, requiring rigid exterior cable routing through pulleys mounted to the ground, proved both complex and impractical given our desire to migrate toward untethered, underwater applications. Thus in this work we have adapted a pneumatic actuator design inspired by the class of

commonly-used pneumatic elastomeric actuators called pneu-nets[50] so that it can be co-printed within a soft tubular body. Pneu-nets actuators have been applied to a variety of soft robotic applications, due to their relatively compact size, flexibility, and good actuating power[42]; they have also been extensively modeled for the purposes of increasing performance across a number of criteria such as force, power, and displacement [139, 80]. Though early pneu-nets were cast in soft rubber, more recent designs have been subsequently adapted for 3D printing[139, 90]. In contrast to prior work – in which actuators are typically flat in their unactuated state and curve when actuated – we have adapted the geometry of our design so that it may be co-printed within a soft tube in order to flatten when inflated.

The process of developing the actuator starts by understanding how the parameters relating to device geometry (as seen in Fig. 4.2b) impact performance. The five key variables include the number of chambers on each side, n, chamber wall thickness (t_1), height (h), width (w), and length (l). The thickness of the chamber wall(t_1) influences the ability of the actuator to retain pressure without leaking, and is influenced both by the material as well as the resolution of the 3D printer. A thinner chamber wall requires lower pressures to deform but results in leaking and poor seals due to the limitation of the 3D printing process. Thus, given the resolution of our 3D printer, t_1 was set at 0.4 mm. A number of different prototypes with variable number of chambers, chamber heights, and chamber widths were then prototyped and evaluated against each other. By inflating the prototypes to the same pressure and comparing the deformation of each, we reached the design parameters as shown in Table. 4.1.

A variety of materials were considered for use in the actuator against a number of design constraints such as stiffness, compatibility with 3D printing, and impermeability with water and air. These constraints ultimately helped focus our search on a small set of materials. With regard to material stiffness, our goal was to select a material that reduced

Table 4.1: Parameters in Final Prototype

Variable	Parameter	Variable	Parameter
D (mm)	50	L(mm)	50
α (degree)	65	θ (degree)	60
w (mm)	5	h (mm)	5
t_1 (mm)	0.4	t_2 (mm)	1.5
l (mm)	14	t_f (mm)	2
n	9		

internal losses due to stretching, while being able to transmit curvature changes over longer distances. Compatibility with 3D printing was considered, not just with regard to temperature, extruder size, and other process characteristics, but with the quality of resulting small feature sizes – such as wall thickness – that impacted the ability of the resulting bladders to operate under high pressures without leaking or popping. Finally, actuator performance was ultimately evaluated by each actuator's respective ability to repeatedly and quickly deform the tube it was mounted within. Based on the above desired characteristics and constraints, two different materials were compared in-depth: thermoplastic polyurethane (TPU) with a shore hardness of 95A[127], and thermoplastic elastomer (TPE) with shore hardness of 92A [1]. To select the material that performed best against our various criteria, we printed two prototypes of the same geometry using both materials, as shown in Fig. 4.3a. In order to compare each material's impermeability to air and water, we compared the layer-to-layer bonding characteristics between the two materials. The quality of the bond between successive layers of TPE was observed to be both smoother and tighter than TPU, which may

[1] Arkema 3DXFLEX™ TPE

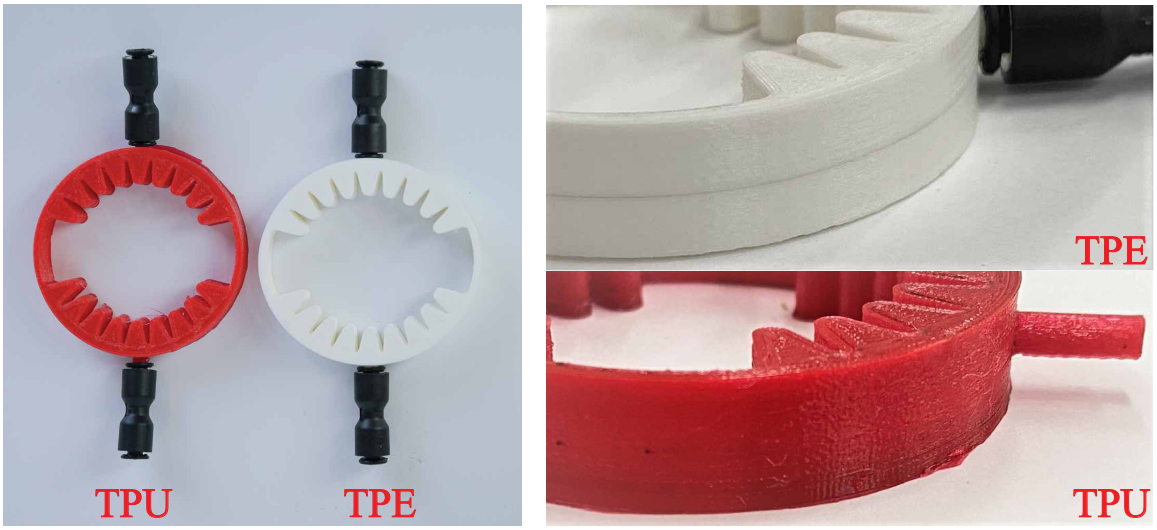

Figure 4.3: **Material Assessment. (a):** The proposed actuator made of TPU and TPE. **(b):** Comparison of the layer bonding performance.

be attributed to the lower melting temperature of TPE (147 $^{\circ}C$) vs TPU (220 $^{\circ}C$). This can be seen in Fig. 4.3b; both prototypes were printed using the same design parameters and the manufacturer's recommended printing parameters. Hence, TPE was selected for the final device.

4.4 Validating Assumption II: Curvature propagation between tube and the attached fins

In this section, we validate the second assumption via FEA. The second assumption is difficult to study using first principle derivations and analytical expressions for a number of reasons. First, the geometries involved – three-dimensional surfaces and curved attachment geometries – are complex problems difficult to represent analytically, especially when working with soft or flexible materials in a fluid environment. Thus we have taken the approach to use FEA to understand the impact of curvature and compliance on deformation in soft structures. For our use, FEA permits the modeling of soft continuum mechanics and

thus benefits the study on validating the proposed assumption and exploring the relation between design variables and paddling gaits.

4.4.1 Concept Validation

To validate the concept that the tube's deformation can be propagated and transmitted to actuate the paddling gait of the fins as well as to alter fin curvature, we conducted a FEA simulation to analyze the fin displacement during the deformation of the tube. The FEA analysis was conducted in Ansys Mechanical [2] using static structral analysis with force convergence criteria. The mesh size is 0.002 m, the number of meshing elements is 68578, the total analysis step is 200, and the analyzing time for each study takes around 25 min using a 24 thread computing workstation.

In order to develop a durable connection between the fin and the tube, the fin's radius of curvature in its neutral configuration is set to equal the radius of the tube. In the simulation, the tube is pinched along the Y-axis at the midpoint of the tube in 200, 0.165 mm increments until the Y-axis displacement reaches 33 mm, or 95% of the tube's deformation range; throughout this process the fins sweep inward and their curvature increases. The FEA result at the initial and the final step is shown in Fig. 4.4d and Fig. 4.4e, respectively. To measure this effect, the maximum planar X-axis, Y-axis, and Z-axis displacement of the fin was analyzed by measuring the displacement of point P (shown in Fig. 4.2a). As shown in Fig. 4.4a, as the tube is increasingly pinched, the fin's displacement grows accordingly. The fin's planar travel, calculated by the total displacement in the X-Z plane, indicates the paddling stroke of the fin, while the Y-axis displacement represents the fin's curvature change during the deformation of the tube. This result validates the proposed concept that the deformation of the tube can be propagated to produce the fin paddling gait as well as to alter the curvature of the fin. The animation of this result is shown in the supplementary

[2] Ansys®, Inc. Mechanical Products 2019 R3

video.

4.4.2 Design Configuration VS Paddling Performance

In order to evaluate the design configuration and assess paddling performance, we seek to explore the relationship between α, θ, and the fin's maximum travel, s (as defined in Section 4.4). Determining the role these two variables play on s establishes the effective transmission ratio between the tube's deformation and the forces exerted at the fins, which can be useful for tuning the relative loading of the structures to induce buckling and hysterisis. Furthermore, we also study the role these two variables play in changing y, the curvature of the fin. Understanding how curvature change during the fin's sweep affects its nonlinear stiffness profile as well as its critical buckling limits in positive and negative bending are useful in design.

To understand the relationship between α, y, and s during the deformation of the tube, six simulations were conducted with different values of α for the same tube displacement (0-33 mm). Attachment angle θ is held constant at 75°; all other design parameters are shown in Table 4.1. As can be seen in Fig. 4.4b, the impact of α on y and s is negligible.

The relationship between θ, y, and s was also studied across six designs where θ was varied between 35°-75°. In this case α was held constant at 75°, while the remaining design parameters are shown in Table 4.1. The results, shown in Fig. 4.4c, reveal a high correlation between attachment angle (θ) and travel (s) without a significant effect on curvature change (y). Based on these results as well as the size limitations of the 3D printer, we selected the design parameters for the final prototype, which are shown in Table 4.1.

4.5 Validating Assumption III: Curvature Change in Fins and the Nonreciprocal Paddling

In this section, we validate the third assumption experimentally and with a derived dynamic model. The actuator described in Section 4.3 is embedded within a longer tube attached to two curved fins, as studied in the FEA model described in Section 4.4. The device is manufactured on an Ultimaker S5 Pro 3D printer using 3DXFlex TPE filament[3]. The final prototype is shown in Fig. 4.5d.

4.5.1 Evaluation of Fin Buckling Limits

As discussed previously, the buckling of curved beams can be influenced by the propagation of curvature from the central tube when it is pinched. To generate positive forward thrust, the buckling limit supporting the drag forces experienced during the power stroke (opposite-sense) must to be higher than the buckling limit experienced by the drag forces during the recovery stroke (equal-sense), as indicated in Fig. 4.5f.

The fin's critical buckling limit was obtained with the prototype to validate this third assumption. As seen in the FEA test in Section 4.4.1, when the tube deforms, the curvature of the fin changes accordingly, resulting in a configuration-dependent fin buckling limit. In this test, the fin's buckling limit was thus obtained at different curvatures. The test setup can be seen in Fig. 4.5f. The main tube's deformation was controlled by regulating the air pressure into the actuator, deforming the tube incrementally at five pressure values from 0-40 psi until it reached its flat state. The tube's displacement can be measured by the position change of two markers attached to the fixture. The result shown in Fig. 4.5e shows the relationship between inflation air pressure and the tube's deformation. At each pressure, a push plate driven on a linear rail pushed the fin over 20 mm in both directions from the fin's

[3] Arkema 3DXFLEX™ TPE

neutral configuration while the force was recorded. In order to receive a reliable static result, the test was conducted five times for each pressure configuration. The shaded error bar plots in Figs. 4.5a, b show the force data collected in the equal and opposite sense across for each pressure value. As can be seen in Fig. 4.5a, when the push plate moves in the opposite sense direction, representing the power stroke, the maximum force reaches 5.02 N. In contrast, as seen in the Fig. 4.5b, in the equal-sense direction (representing the recovery stroke), the maximum drag reaches only 0.32 N. To further highlight the asymmetric buckling limit on each side of the fin, the maximum drag experienced in both directions from Figs. 4.5a, b has been plotted in Fig. 4.5c. The difference in buckling limits between the two orientations of the fin demonstrates the anisotropic behavior made possible via the fin's curvature. The trend found in Fig. 4.5c indicates that, as the tube deforms, and the fin moves closer to the body, the increased curvature change raises the buckling limit in the opposite sense while weakening the buckling limit in the equal sense.

4.5.2 Swimming Thrust

Based upon the validity of the three assumptions above, the proposed device should be expected to be able to swim forward. In this section, we validate this hypothesis experimentally by measuring the thrust generated by the prototype as well as the maximum swimming speed. The net forward thrust is measured using the prototype in Fig. 4.5d. The device is attached to a force sensor and then fixed in the water, as shown in Fig. 4.6a. During the test, the air pressure is regulated to 60 psi to make sure that the tube can be fully deformed. A 2-position solenoid valve (NITRA, AVS-3212-24D) is selected to control the air inflation and deflation. The air inflation and deflation cycle is commanded at different frequencies while the thrust generated by the device is recorded. After running multiple sets of tests at different frequencies, the highest thrust was obtained at the solenoid's maximum cycle speed of 1 Hz. The thrust over time for this case is shown in Fig. 4.6c. This plot shows

that the positive forward thrust produced by the fin during the power stroke reaches $1.2N$, while the minimum thrust value, obtained during the recovery stroke reaches $-0.98N$; the net thrust averaged over a full cycle is $-0.05N$. Because of low drag and inertial loads acting on the fin, buckling in the fins was not readily observed during the test. When allowed to swim freely, the prototype traveled a negligible distance over a large number of cycles.

In order to induce buckling and generate more asymmetric thrust, a fin extension (called the "load fin") was attached to the device, as shown in Fig. 4.6b. It is made of fiberglass and weighs 2.05 g. The test was then repeated at the same air pressure and frequency; the result is shown in Fig. 4.6d. Due to the increased drag from the load fin, the peak thrust during the power stroke increases to 2.6 N, but – due to buckling during the recovery stroke – the peak minimum thrust drops to -0.47 N. Overall net thrust, averaged over the full cycle, increases from -0.05 N to 0.23 N. This increase in net forward thrust is also reflected in better swimming results; when the system with attached load fins swam freely in the tank it reached an average forward swimming speed of 53 mm/s, which is 1.33 body length per second. Based on the Reynolds number of a flapping wing in fluid, formulated from [136, 76], the Reynolds number of the device was calculated using $Re = \frac{\bar{u}\bar{c}}{\nu}$, where $\bar{u}, \bar{c}$ and ν are the mean translational velocity of the wing tip, the mean chord length, and the kinematic viscosity of the fluid, respectively. In this proposed system, the mean translational velocity of the wing tip $\bar{u}$ is analysed from the slow motion video. We measured the velocity at two locations of the fin under both power stroke and recovery stroke. For the tip of the load fin, which is the point b in Fig. 4.6b, the translational velocity at the power stroke is $\bar{u} = 29.76\ mm/s$, the translational velocity in the revovery stroke is $\bar{u} = 24.2\ mm/s$. This leads to the Reynolds number within the range of 2024 to 2490. As for the tip of the TPE fin, which is the point a in Fig. 4.6(b), $\bar{u} = 19.2\ mm/s$ at the power stroke cycle, and $\bar{u} = 16.2\ mm/s$ in the recovery stroke. The Reynolds number of the system is then calculated to vary from 855 to 1014. This indicates that the system flow regime changes

from laminar to turbulent.

4.5.3 Dynamic Modeling

In this section, we describe the dynamic modeling of the system, focusing on the curved fins' asymmetric buckling behavior and its effect on thrust generation; studying the system's dynamic behavior under similar conditions with the experimental swimming thrust tests covered in Sec. 4.5. In the proposed dynamic model (Fig. 4.6e, each half of the system is represented by three planar rigid links (x_1, m_1, and d_2, m_2, and d_3, m_3) with point masses located at the links' midpoints. Tube deformation is modeled as a prismatic joint, while each fin is modeled by two rigid links that are connected by pin joints and a nonlinear torsional spring.

We first experimentally identify a model describing the effect of the pneumatic activation and the curvature propagation on the attachment (x_1) and its rotation (θ_1). These parameters are measured using the experimental setup in Fig 4.5e, across input pressures ranging from 0-40 psi. The fins' rotation about the tube is modeled as a function of x_1, which is derived from experimental measurements. In our dynamic model, we use a combination of a horizontal input force and a spring-damper mechanism in order to match the variation of x_1 in time to best fit the experimentally-collected motion of the fins' proximal connection.

Using the above relations, the pneumatic actuation, tube deformation, and fin configuration can be modeled under no-load conditions. The distal portion of the fin's asymmetric deformation and stiffness under load (K) are next modeled. Using the nonlinear behavior of the curved fins (Figs. 4.5a, b) and the fins' configuration for each tube deformation, the fins' equal and opposite-sense bending under load are represented as a torsional spring with variable stiffness; this is a function of the tube's deformation (x), fin orientation (θ), and curvature (y). A two-term exponential function is applied to fit experimentally-collected

data correlating the measured stiffness (K) against all configurations.

Using a flat plate model derived from [99], the forces on the fin due to the fluid are estimated as

$$F_{w_D} = \rho u^2 A \sin^2 \alpha \tag{4.1}$$

$$F_{w_L} = \rho u^2 A \cos \alpha \sin \alpha, \tag{4.2}$$

where ρ, u, A, and α are the density of fluid, the relative velocity of the plate, the area of the plate, and the angle of attack of the wing, respectively. F_{w_D} and F_{w_L} correspond to the drag and lift components of aerodynamic forces acting on the plate. The total force on a flat plate is estimated as

$$F_w = \rho u^2 A \sin \alpha, \tag{4.3}$$

where α is 0 when parallel to the flow and 90° when perpendicular (in 2D) [99]. This force is perpendicular to the wing and acts as the fluid's dynamic load on the distal end of the curved beam. Based on previous work, we have shown that the error between a flat plate model and a Computational Fluid Dynamic model is less than 15% for a device at a similar scale and speed, with a maximum Reynolds number less than 7200 [105]. When the system is within the laminar regime, the flat plate model has a high correlation with the CFD result. Thus, we believe that the flat plate approximation holds well in this case as well, especially since it reduces computational complexity and simulation time.

The dynamic model is then evaluated by comparing the model's thrust estimate against data collected experimentally. By defining rigid constraints connecting the main body of the robot to ground, the forces exerted on the environment when a fin is actuated can thus be measured. Two cases are considered: the thrust generated by the fins alone (Fig. 4.5h), and with the extra load fins attached (Fig. 4.5i). Similar to the experiment, the results show that the positive net thrust is generated due to the asymmetric stiffness model identified for k (Fig. 4.6h), however, buckling is not obvious in the first case due to the smaller

inertias and lower drag acting on the fins (Fig. 4.6g). The maximum and minimum thrust estimated by the model for this case are 1.2 N and -0.72 N, respectively. Fig. 4.6f,h show the model's estimate of a fin's motion and thrust generated across multiple cycles in the second case, respectively. These data reveal that the contribution of inertia and drag from the load fin increases the loading on the beam, forcing it to undergo buckling. This results in a minimum thrust of -0.38 N during recovery, smaller than case 1. By contrast, the maximum positive thrust increases to 2.58 N.

Comparing the simulation and experimental results show that the proposed dynamic model is capable of estimating the system behavior for both cases and can effectively implement the nonlinear behavior of the curved fins. We believe this model will inform future design optimization aiming to increase the efficacy of the proposed mechanism.

4.6 Conclusions and Future Work

This work summarizes our current work in understanding how to leverage curvature change, shape propagation, buckling, and hysteresis in soft systems to reduce the actuation and control complexity for swimming. Through the use of the dynamic models presented herein, we have demonstrated the potential for further improving performance in Soft, Curved, Reconfigurable Anisotropic Mechanisms, or SCRAMs, by showing how small changes in loading conditions can induce larger changes in thrust and work generation. Finally, by creating a monolithic, 3D-printed prototype, we have demonstrated how future designs may be printed on demand as the result of a more integrated optimization pipeline.

Future work will focus on untethered, autonomous swimming applications in which multiple fins are attached to a single power source; we seek to apply the concept of pneumatically pinched tubes to further increase the available degrees of freedom in such systems and reconfigure such robots for multi-modal locomotion in a variety of media. This will

require much tighter integration of simulation and modeling to include fluid or granular interactions as well as more optimized design geometries to obtain more energy-efficient locomotion. Furthermore, we need to enhance the versatility of fluid dynamics modeling to cover both laminar and turbulent regimes; this will enable us to model system behavior at various scales and actuation speeds.

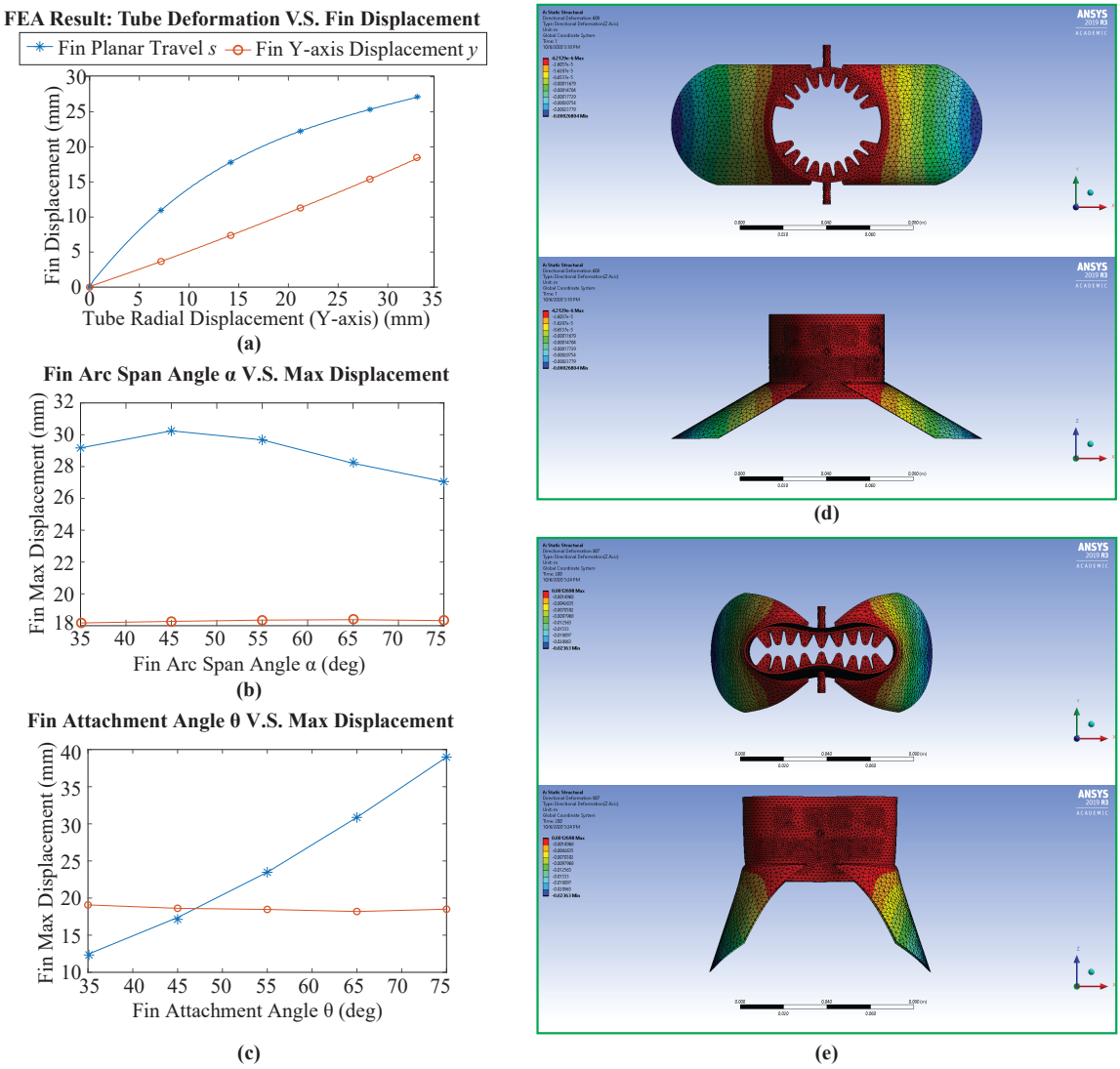

Figure 4.4: **FEA Validation.** **(a):** Concept validation via FEA. **(b):** FEA result of the relation between the fin arc length angle and the fin max displacement along Y-axis and the fin's max travel. **(c):** FEA result of the relation between the fin attachment angle and the fin max displacement along Y-axis and the fin's max travel. **(d):** FEA result at initial step. **(e):** FEA result at final step.

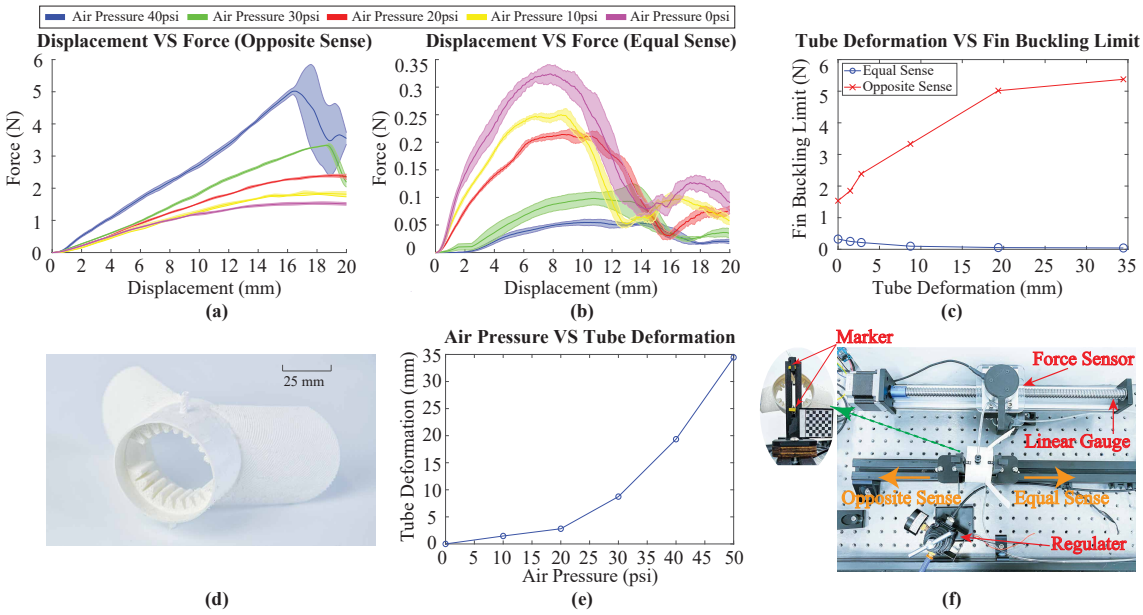

Figure 4.5: **Fin Buckling Test.** **(a):** The fin drag force data collected when the pusher moves in opposite sense under different tube deformation states. **(b):** The fin drag force data collected when the pusher moves in equal sense under different tube deformation states. **(c):** The fin critical buckling limit in both opposite sense and equal sense under different tube deformation. **(d):** The final prototype. **(e):** The tube deformation under different inflation air pressure. **(f):** The test setup.

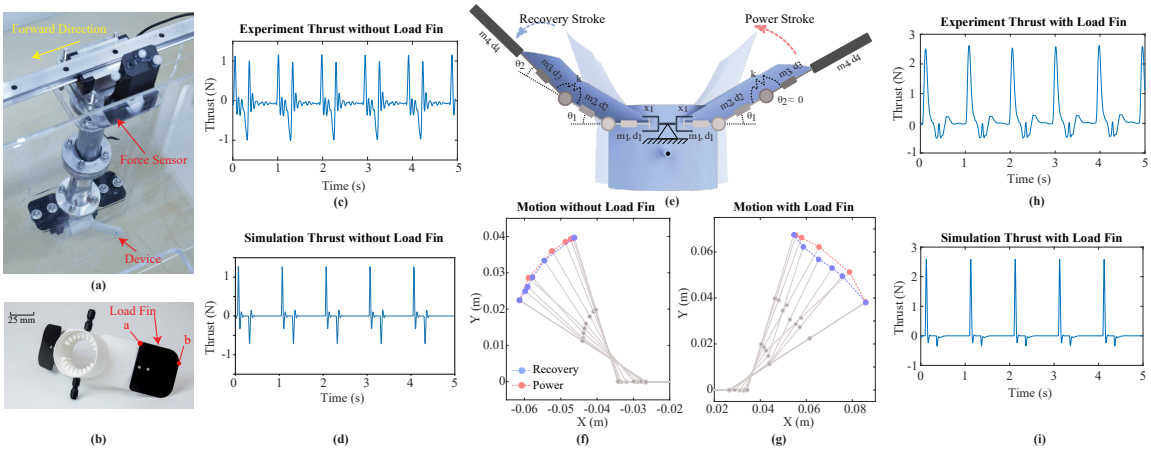

Figure 4.6: **Swim Test (a):** The thrust test setup. **(b):** The device with the load fin. **(c):** The thrust measured without load fin at frequency = 1 Hz. **(d):** The thrust measured with load fin at frequency = 1 Hz. **(e):** The proposed dynamic model. **(f):** The simulation trajectory of the paddling gait with load fin. **(g):** The simulation trajectory of the paddling gait without load fin. **(h):** The simulation thrust without load fin. **(i):** The simulation thrust with load fin.

Chapter 5

TUNABLE DYNAMIC WALKING VIA SOFT TWISTED BEAM VIBRATION

5.1 Introduction

Actuation and its transmission through soft robotic systems have driven extensive study in recent decades [27, 131, 29]. Unlike actuation in traditional rigid-body robotic systems – which relies on motors, gears, shafts, and belts to actuate and transmit power – the morphology of soft actuators can be deformed to subsequently alter body shapes and drive robots by stimulating or deforming soft materials. While numerous soft actuators have been developed to drive soft robots in applications like human-robot interaction, bio-inspired robots, and wearable robotic systems, the power of these systems is usually low and actuators are usually bulky. Moreover, due to the non-linearity of hyper-elastic materials and the complexity of powered soft systems, dynamic modeling is challenging and thus can be underutilized during design.

In this work, we propose a novel actuating method for walking robots using the coupled compliance of soft twisted beams with ground contact. This mechanism transforms simple, periodic inputs into complex cyclic motion under contact with the ground. More specifically, we show how this phenomenon can be adopted to generate tunable bidirectional walking via the input frequency. This study fits under the umbrella of a new class of devices we call ”Soft, Curved, Reconfigurable, Anisotropic Mechanisms” (SCRAMs), which we have previously studied in the context of pinched tubes[53, 55, 52], and buckling beams[106, 107]. By taking advantage of the shape and material properties in soft structures, complex actuation signals for generating complex motion can be consolidated and simplified.

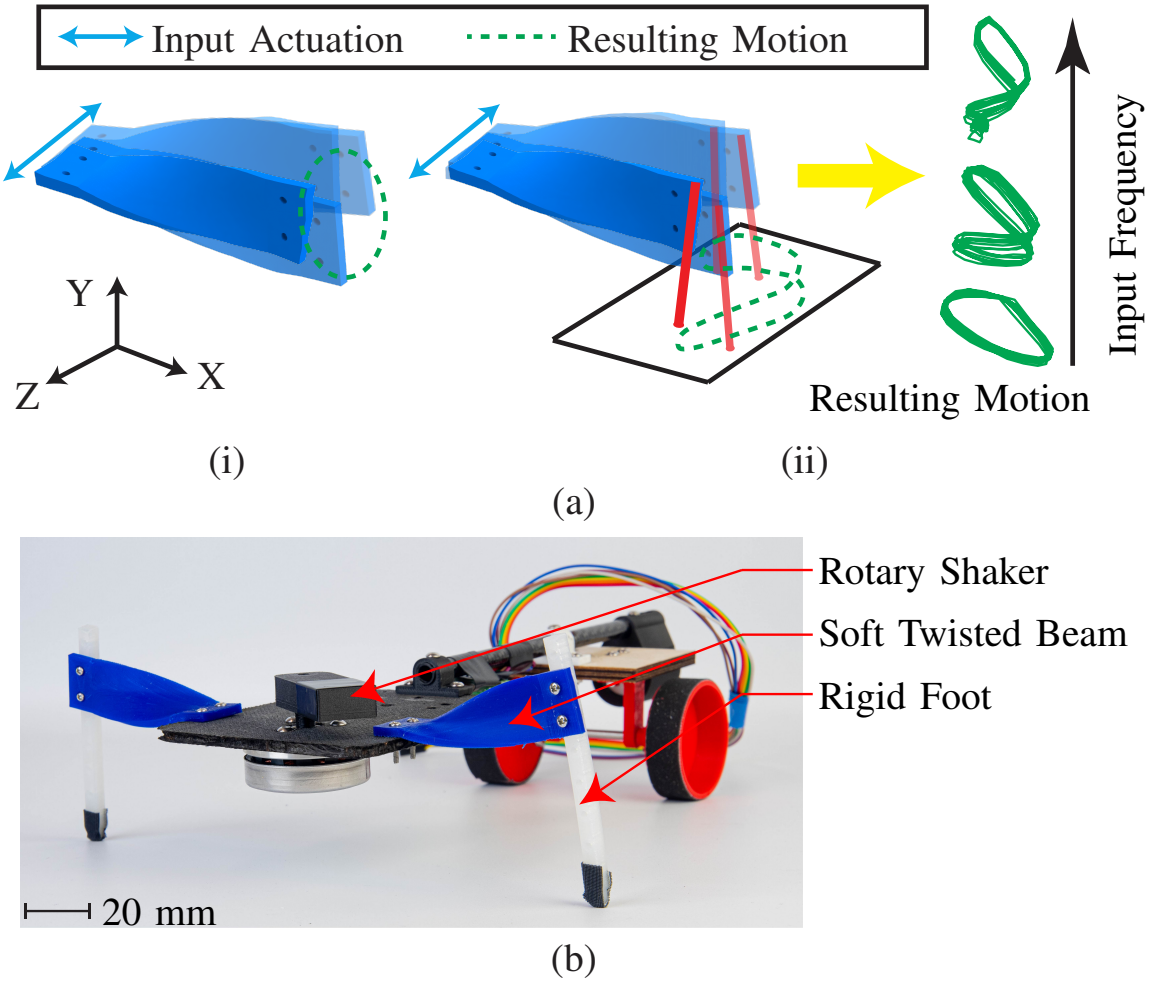

Figure 5.1: **Concept demonstration and beam design. (a):** Conceptual demonstration of the operation principle: (i) without terrain contact; (ii) with terrain contact. **(b):** Walking robot prototype.

Fig. 5.1(a) demonstrates the proposed concept. In (i), a soft, twisted beam under a linear vibratory input (shown by the blue arrow) generates a repeating, semicircular trajectory at the tip (shown in dashed green lines). With terrain contact, this motion results in a more complex motion that can be controlled and further adapted for robot walking (ii) using the prototype as shown in Fig. 5.1(b).

5.1.1 Contributions

The contributions of this work may be summarized as follows: 1) A new mechanism has been proposed for generating walking locomotion using soft twisted beams under interaction with the ground; 2) A new computationally-efficient pseudo-rigid body (PRB) model has been developed that accurately describes the dynamic behavior of the highly nonlinear system. We then 3) demonstrate how walking direction and speed can be tuned by the frequency of the input actuator both experimentally and in simulation.

5.2 Static Stiffness Test

Here we show the static stiffness test in Fig. 5.2. These results support Section 3.1 of the primary manuscript.

The static, fixed-displacement test was conducted to measure each beam's shear force and bending moment at different positions on beams with $\phi = 0^\circ$, $\phi = \pm 45^\circ$, and $\phi = \pm 90^\circ$. The test setup is shown in Fig. 5.2(f). The proximal end of the beam was fixed to the ground while the distal end was attached to a UR-5e robotic arm, which moved the beam's end-effector 5 mm along the global y-axis and z-axis and rotated the beam $\pm 15^\circ$ about the global x-axis. The forces and torques about each axis were collected with a six-axis, ATI Mini 40 force-torque sensor. The sensor's mounting location is shown alongside the rest of the test setup in Fig. 5.2(f).

Fig. 5.2(a)-(e) show the force and torque data collected during the static stiffness test with respect to changing values of ϕ. We compared the force and moment behavior in first column (Fig. 5.2(a)(c)) against the second column (Fig. 5.2(b)(d)) to understand the impact of beam chirality. The first row (Fig. 5.2(a)(b)) is compared against the second row (Fig. 5.2(c)(d)) to highlight the impact of ϕ's magnitude. Fig. 5.2(e) shows baseline data from the un-twisted beam.

Using deflection along the y-axis as a case study, we see very different behavior between untwisted beams ($\phi = 0^\circ$, shown in Fig. 5.2(e)), beams with $\phi = \pm 45^\circ$, and beams with $\phi = \pm 90^\circ$) under a simple translation in the y-direction. By comparing the reaction forces corresponding with $\phi = \pm 45^\circ$ (the second row of Fig. 5.2(c) and (d)) against the force data from beams with $\phi = \pm 90^\circ$ (the first row of Fig. 5.2(a) and (b)), we can see that the orthogonal forces measured for beams with $\phi = \pm 90^\circ$ are higher than beams with $\phi = \pm 45^\circ$. Furthermore, the coupled reaction torques about the y and z-axes are much different in the $\phi = \pm 90^\circ$ beams than the $\phi = \pm 45^\circ$ beams. This highlights the impact of the twist angle on coupling behavior. Additionally, by comparing the forces between positive and negative twist angles, which is contrasted byFig. 5.2(a) and (c) against Fig. 5.2(b) and (e), the coupling behavior is observed to exhibit mirrored behavior. This result reveals the potential of reversing the coupling behavior of the twisted beam by switching the chiral direction.

5.3 Static Stiffness Modeling

To understand the coupling behavior in the system, we developed a stiffness matrix for the static values obtained for the $\phi = \pm 90^\circ$ twist angle beams. Based on Hodges' work [44], the conventional quadratic stiffness model with bending forces and shear moments in three directions can be represented as

$$\begin{bmatrix} F_x \\ F_y \\ F_z \\ M_x \\ M_y \\ M_z \end{bmatrix} = Q \begin{bmatrix} X_x^2 \\ X_y^2 \\ X_z^2 \\ \theta_x^2 \\ \theta_y^2 \\ \theta_z^2 \end{bmatrix} + K \begin{bmatrix} X_x \\ X_y \\ X_z \\ \theta_x \\ \theta_y \\ \theta_z \end{bmatrix} \tag{5.1}$$

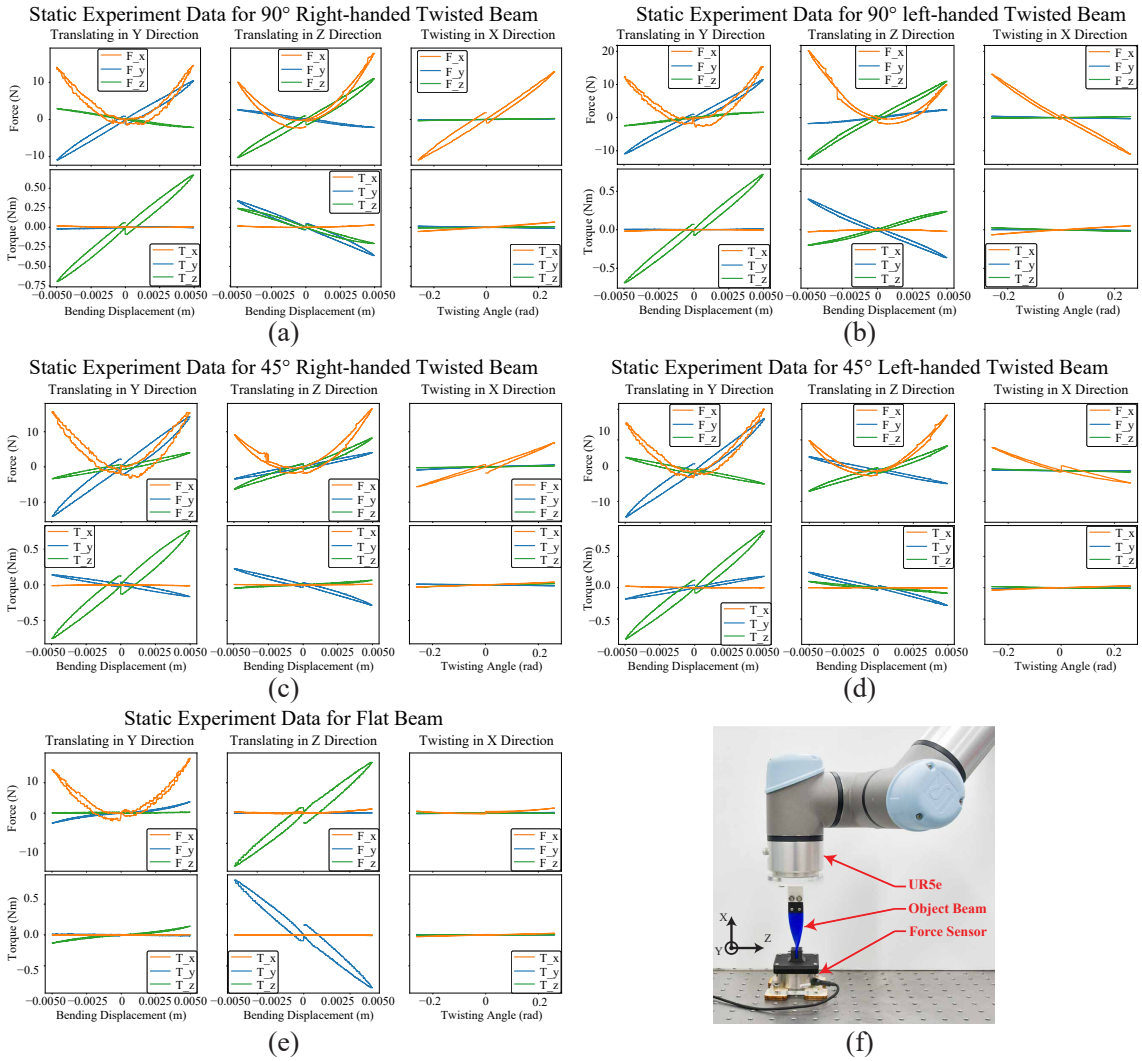

Figure 5.2: Static stiffness test

where

$$Q = \begin{bmatrix} p_{xx} & p_{xy} & p_{xz} & q_{xx} & q_{xy} & q_{xz} \\ p_{yx} & p_{yy} & p_{yz} & q_{yx} & q_{yy} & q_{yz} \\ p_{zx} & p_{zy} & p_{zz} & q_{zx} & q_{zy} & q_{zz} \\ r_{xx} & r_{xy} & r_{xz} & s_{xx} & s_{xy} & s_{xz} \\ r_{yx} & r_{yy} & r_{yz} & s_{yx} & s_{yy} & s_{yz} \\ r_{zx} & r_{zy} & r_{zz} & s_{zx} & s_{zy} & s_{zz} \end{bmatrix}, \tag{5.2}$$

$$K = \begin{bmatrix} k_{xx} & k_{xy} & k_{xz} & m_{xx} & m_{xy} & m_{xz} \\ k_{yx} & k_{yy} & k_{yz} & m_{yx} & m_{yy} & m_{yz} \\ k_{zx} & k_{zy} & k_{zz} & m_{zx} & m_{zy} & m_{zz} \\ t_{xx} & t_{xy} & t_{xz} & n_{xx} & n_{xy} & n_{xz} \\ t_{yx} & t_{yy} & t_{yz} & n_{yx} & n_{yy} & n_{yz} \\ t_{zx} & t_{zy} & t_{zz} & n_{zx} & n_{zy} & n_{zz} \end{bmatrix} \tag{5.3}$$

After observing the test result in Fig. 5.2, the quadratic relation only applies to the force in the Z direction when bending in both X and Y directions. Therefore, we reduced the Q matrix only to capture these two forces. The simplified Q matrix is

$$Q' = \begin{bmatrix} 0 & 0 & 0 & 0 & 0 & 0 \\ 0 & 0 & 0 & 0 & 0 & 0 \\ p_{zx} & p_{zy} & 0 & 0 & 0 & 0 \\ 0 & 0 & 0 & 0 & 0 & 0 \\ 0 & 0 & 0 & 0 & 0 & 0 \\ 0 & 0 & 0 & 0 & 0 & 0 \end{bmatrix} \tag{5.4}$$

The stiffness model can be further simplified to a linear model if we assume that the displacement at the end effector is entirely the result of bending about the x, y, and z axes,

rather than stretching. The simplified linear model can be represented as:

$$\begin{bmatrix} F_y \\ F_z \\ M_x \end{bmatrix} = K' \begin{bmatrix} X_y \\ X_z \\ \theta_x \end{bmatrix}, \text{where} \tag{5.5}$$

$$K' = \begin{bmatrix} k_{yy} & k_{yz} & m_{yx} \\ k_{zy} & k_{zz} & m_{zx} \\ t_{xy} & t_{xz} & n_{xx} \end{bmatrix}. \tag{5.6}$$

where k terms represent the linear coupling between orthogonal directions in N/m, m terms represent the coupling between twist and force in N/rad, t terms represent the coupling between linear displacement and moment in N-m/m, and n_{xx} represents the coupling between twist and moment in N-m/rad.

We collect terms with the relationship by fitting the data collected from Sec. 5.2 into the model. The K' matrix was developed for beams with $\phi = 0°$, $\phi = \pm 45°$, and $\phi = \pm 90°$, respectively as below.

$$K'_{\phi=0^o} = \begin{bmatrix} 5504.72 & 28.19 & -0.20 \\ 10.79 & 559.69 & 0.73 \\ 0.04 & 0.66 & 0.10 \end{bmatrix} \tag{5.7}$$

$$K'_{\phi=45^o} = \begin{bmatrix} 1335.00 & 681.35 & 1.00 \\ 714.29 & 2600.24 & 2.63 \\ 0.25 & -0.29 & 0.13 \end{bmatrix} \tag{5.8}$$

$$K'_{\phi=-45^o} = \begin{bmatrix} 1340.93 & -811.05 & -1.77 \\ -834.86 & 2951.52 & -0.41 \\ -0.65 & -2.24 & 0.13 \end{bmatrix} \tag{5.9}$$

$$K'_{\phi=90^o} = \begin{bmatrix} 2231.54 & 439.96 & 0.83 \\ 457.14 & 2113.52 & -1.37 \\ 0.68 & 1.32 & 0.22 \end{bmatrix} \tag{5.10}$$

$$K'_{\phi=-90^o} = \begin{bmatrix} 1993.62 & -537.18 & 1.12 \\ -505.81 & 2003.95 & 0.62 \\ 1.37 & -1.31 & 0.23 \end{bmatrix} \tag{5.11}$$

To better understand the static coupling behavior in beams, we compare the elements of K' in Table 5.1. We can see that k_{yy} and k_{zz} terms are larger in beams where $\phi = 0^\circ$, while k_{yz} and k_{zy} coupling terms are relatively low. This means that the un-twisted beam deforms principally along the direction of the input rather than along orthogonal directions. However, beams with $\phi = \pm 45^\circ$ and $\phi = \pm 90^\circ$ show relatively higher coupling in k_{yz} and k_{zy} terms. This means that beams with $\phi = \pm 45^\circ$ and $\phi = \pm 90^\circ$ not only deform and react in the direction of input forces, but in other directions as well. This result demonstrates how single-direction forces can be transformed into a coupled set of resultant forces in orthogonal directions via twisted soft beams, and where, even in simple models, where the parameters that describe this phenomenon reside.

Table 5.1: Twisted Beam Static Stiffness Coefficient

Beam Configuration (ϕ)	k_{yy}	k_{yz}	m_{yx}	k_{zy}	k_{zz}	m_{zx}	t_{xy}	t_{xz}	n_{xx}
0°	5504.72	28.19	-0.20	10.79	559.69	0.73	0.04	0.66	0.10
45°	1335.00	681.35	1.00	714.29	2600.24	2.63	0.25	-0.29	0.13
−45°	1340.93	-811.05	-1.77	-834.86	2951.52	-0.41	-0.65	-2.24	0.13
90°	2231.54	439.96	0.83	457.14	2113.52	-1.37	0.68	1.32	0.22
−90°	1993.62	-537.18	1.12	-505.81	2003.95	0.62	1.37	-1.31	0.23

5.4 System Modeling

We conduct a series of FEA-based dynamic simulations with PyChrono [120], demonstrating how input frequency, beam chirality, and the magnitude of beam twist angle alter the dynamic motion of the beam. A simplified pseudo-rigid-body (PRB) model is then proposed and evaluated for improving simulation speed in the presence of contact.

5.4.1 Dynamic Modeling Using FEA Approach

FEA model setup: We developed a FEM-based dynamic model, which consists of a 120-element mesh generated from a single layer of 6-field Reissner-Mindlin shells, seen in Fig. 5.3(a). The mesh geometry replicates the beam design outlined in Sec. 5.5; the material properties for TPU came from its datasheet.

The input actuator shakes the proximal end of the beam along the z-axis as shown in Fig. 5.3(a). The input signal is

$$x = A\sin(2\pi ft), \tag{5.12}$$

where x is the actuation travel position with the unit of mm, f is the rotating frequency of the motor in Hz and A is the amplitude in mm with $A = 2\,\text{mm}$.

Input Frequency V.S. Resulting Motion: The coupled stiffness of twisted beams can be exploited by exciting it at specific frequencies to create highly differentiated motion. To demonstrate this effect, we swept the input frequency from $f = 1\,\text{Hz}$ to $f = 45\,\text{Hz}$ in 1 Hz increments. The trajectory of the beam's distal end was recorded throughout the simulation and is shown in Fig. 5.3(d). While the resulting trajectory is in three dimensions, the Y-Z plane motion is observed to dominate the resulting behavior. Thus Y-Z plane trajectories were demonstrated throughout the study. As can be seen, the beam's trajectory varies significantly in shape and size as a function of input frequency. At certain input frequencies such as 9 Hz, 17 Hz, 25 Hz, the trajectory exhibits an oval-like shape, whereas

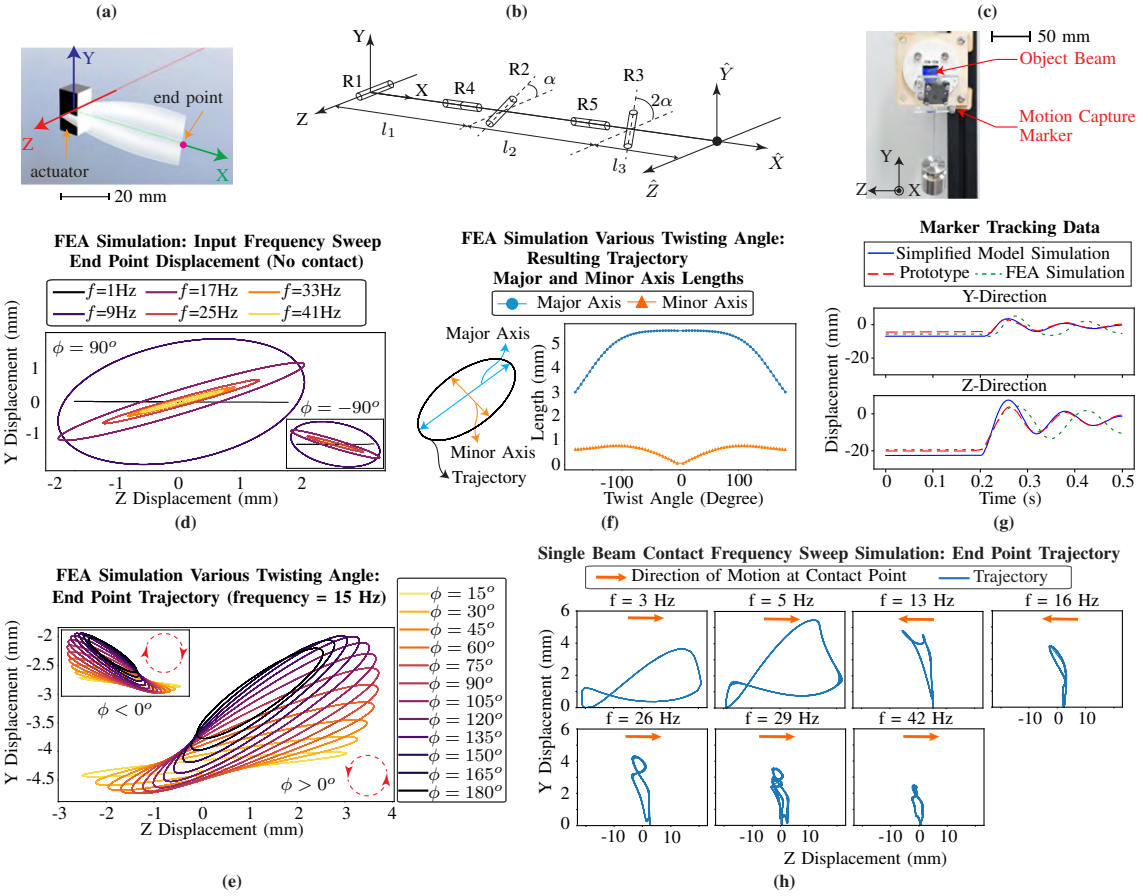

Figure 5.3: **Results from FEA simulations. (a):** Beam FEA mesh model; **(b):** The proposed analytical model; **(c):** The lab test setup for simplified model fitting; **(d):** Beam end point trajectory results from frequency sweep simulation using FEA simulation; **(e):** Beam end point trajectory results from FEA simulation with twist angle from $\phi = -180^o$ to $\phi = 180^o$; **(f):** Major and minor axis lengths of beam end point trajectory with respect to twist angle ϕ; **(g):** Example marker tracking data from calibration experiments; **(h):** Beam end point trajectory results from frequency sweep simulation with contact using the proposed analytical model;

at frequencies such as 1 Hz and 41 Hz the trajectory appears more linear.

Beam twist V.S. resulting trajectory: A beam's magnitude of twist plays an important

role in the generation of elliptical motion, while its chirality (twist direction) can be used to mirror the patterns observed at different magnitudes. We explored the relationship between beam twist angle ϕ and its resulting trajectory through a pair of studies. In the first study, we modeled a series of beams with identical dimensions but a range of twist angles from $\phi = 0^\circ$ to $\phi = 180^\circ$ with a step of 5°. The input amplitude and frequency was held constant at $f = 15\,\text{Hz}$ and $A = 2\,\text{mm}$. The distal end's trajectory was recorded during the simulation; the selected result is shown in Fig. 5.3(e). As the twist angle ϕ increases, the output trajectory's orthogonal motion (along the Y axis) grows. To better understand the nature of the shapes generated, we approximated each trajectory as an elliptical path using a least squares minimization function [128], identified the major and minor axes of the approximate ellipses at each frequency, and then measured their length. The results, shown in Fig. 5.3(f), highlight how twist magnitude and the resulting coupling of stiffness play a role in the evolution of elliptical paths in twisted beams. Based on this result, the twist angle ϕ of the prototype beams is set as $\phi = 90^\circ$ and $\phi = -90^\circ$ for the more distinguished spans in both major and minor axis.

In the second set of simulations, we compared beams of equal magnitude but opposite direction ($\phi_1 = -\phi_2$). As seen in Fig. 5.3(e), beams of equal magnitude but opposite chirality result in trajectories mirrored across the Y-axis, the beams' axis of symmetry (path shape and direction of motion, as highlighted in Fig. 5.3(e) by the red dashed arrows).

5.4.2 Pseudo-rigid-body Modeling

While the FEA simulation qualitatively validates the proposed concept, its shortcomings have limited its further use. First, accurate FEA simulation relies on well-defined meshes and models that precisely describe the stiffness and damping of materials. Prototyping with 3D printing introduces variation within the beam and between different beams, with highly viscoelastic soft materials, resulting in a poor fit from our FEA model. To

address this, the FEA simulation must be calibrated to each prototype – a computationally expensive endeavor. Considering our use-case for terrestrial simulation, the addition of contact makes FEA models even less feasible. Hence, in order to simulate faster while accurately exploring the dynamic system's behavior with contact, a simplified model using the pseudo-rigid-body (PRB) model is then proposed to describe the dynamic behavior of twisted beams over time. The principal differences between this approach and the FEA model are that, by reducing the number of degrees of freedom (DOF) through a set of principled assumptions about deformation, a more computationally efficient PRB representation can be used within off-the-shelf rigid body simulators, which solve problems of contact and friction more efficiently, allowing us to more thoroughly explore the system-level dynamics of the walking robot. An evolutionary-optimization-based fitting process can then be more easily applied to quickly fit the model to each prototype's captured properties, allowing us to simulate system motion with higher accuracy.

Pseudo-rigid-body model setup: Off-diagonal coupling parameters, along with hyperelastic material models, make the dynamics of twisted soft systems more complex than classical approaches such as Euler–Bernoulli models can approximate. Fundamental research has analyzed the behavior of pre-twisted beams using variational formulations [44] and geometrically intrinsic dynamic models [45], for the dynamics of stiff, pre-twisted beams. Banerjee demonstrates the use of approximate representations of twisted beam dynamics using simplified models with two cooperative linear motions across two mutually-orthogonal planes [7]. Other work by Howell also demonstrates the suitability of cantilever-style PRB models for large deflections [47, 48]. Due to this prior art, the PRB model with revolute springs attached to a number of joints subdividing the beam was selected to describe the two-DOF orbit at the beam's distal end. The design parameters, stiffness, and damping values were then calibrated to match the manufactured prototype's behavior. Although the kinematics are specifically selected for analyzing the dynamic behaviors ob-

served in our system, making it less general, the computational cost savings over more general approaches permitted more and better fitting to our prototype and enabled more parameter exploration.

We use a linear spring-damper model of the form $\tau = k\theta + b\dot{\theta}$ to describe the moments about each joint, where τ represents the torque about each joint, k represents the linear spring constant in bending, b represents linear joint damping, and $\theta, \dot{\theta}$ represent the local rotation and rotational velocity, respectively, of each joint from its unloaded, natural shape. Since the cross-sectional area of each beam is constant along its axial length, the spring stiffness constant k represents a distributed bending stiffness about three revolute joints – R1, R2, and R3 – which are distributed perpendicularly along the beam's axial direction, as seen in the complete model in Figure. 5.3(b). Two additional revolute joints – R4, and R5 – are aligned with the beam's local axial direction and capture the twist of the beam, represented by ϕ. The same spring-damper model is also applied to represent the twisting stiffness between these two joints.

Together, these joints exhibit the same coupled stiffness of twisted beams observed in experiments. Based on the results from [47, 48], the location of joints in a compliant, cantilever-style PRB model under large deflections should not be evenly distributed along the beam; we thus parameterize l_1, l_2, l_3 as the distances between R1-R2, R2-R3, and R3 - distal end, respectively. The total length of the beam, $l = l_1 + l_2 + l_3 = 50\,\text{mm}$, is identical to the prototype. Mass is evenly distributed using $\rho = 1210 kg/m^3$ (the density of TPU), with an assumption of constant cross-sectional area. The sum of all links' mass is equal to the prototypes' mass of $m = 5.17\,\text{g}$.

Model fitting: A set of dynamic experiments was conducted to obtain the motion of the end of the beam when released from an initial deformed state. The test setup can be seen in Fig. 5.3(c). At the beginning of the test, the beam was deformed with a 200 g load applied to the end. The load was instantaneously released from the beam while the

position of the beam's tip was recorded as the beam returned to rest at its natural unloaded position. Three optical tracking markers were attached to the end of the beam to obtain the tip's motion. After the data was recorded, a differential evolution optimizer [111] was implemented to fit the model variables (k, b, l_1, l_2, l_3) by minimizing the averaged error between simulation marker position data (M_i) and the reference data from experiments ($\hat{M}_i$) and objective function

$$Min\left\{\sqrt{\sum_{j=0}^{n-1}\sum_{i=1}^{3}\left[(M_i(j)-\hat{M}_i(j))^2\right]/(3n)}\right\}. \tag{5.13}$$

The optimization variable set is defined by (k, b, l_1, l_2, l_3), where $l_3 = 50 - l_1 - l_2$. In this fitting progress, the proposed model was simulated in MuJoCo [124] and Python. We observed that l_1 tended to converge at the minimum bound of 1 mm; We therefore simplified the model by setting $l_1 = 0$, which yields the variable set as (k, b, l_2, l_3), where $l_3 = 50 - l_2$. The optimizer finally converged with an averaged dynamic tracking error of 9.38%, where $k = 0.340\,\text{N·m/rad}$, $b = 0.0029\,\text{N·m/(rad/s)}$, $l_2 = 23.66\,\text{mm}$, $l_3 = 26.34\,\text{mm}$.

To compare the two models with the prototype, we conducted the FEA simulation using the same test setup as shown in Fig. 5.3(c). The marker tracking data from the test is shown in Fig. 5.3(g). As can be seen, the proposed simplified model with calibration outperforms the FEA model on tracking the dynamic motion of the twisted beam prototype. The averaged dynamic tracking error using the simplified model is 9.38%, and 34.79% using the uncalibrated FEA model. The average time cost for a 10 s simulation with an Intel i9-7900K CPU and 32GB RAM was also shortened from 82.5 s with the FEA model to 1.2 s using the PRB model.

Simulation of single beam vibration with contact: Using the newly proposed PRB model, we conducted a series of beam vibration simulations with contact in MuJoCo. The test setup is identical to that described in Sec. 5.6.3. During the simulation, the slider is actuated to sweep from $f = 1\,\text{Hz}$ to $f = 45\,\text{Hz}$ using (5.12) with amplitude $A = 2\,\text{mm}$

while the beam's endpoint position is recorded. The resulting trajectory and the direction of motion at the contact point are shown in Fig. 5.3(h). As can be seen, the resulting motion differs from the free vibrating beam due to contact with the floor. A figure '8' loop is observed at the input frequency $f = 16\,\text{Hz}$ and $f = 26\,\text{Hz}$. Moreover, the direction of motion at the contact point, as indicated by orange arrows, also alters as a function of the input frequency.

5.5 Design and Manufacturing of the Prototype Beam

We designed and manufactured a series of prototypes to validate the proposed concept. 3D printing was selected to reduce manufacturing time and to permit a broad design space. Because hard printable plastics must be printed with very thin geometries and at higher precision to achieve the desired range of leg stiffnesses, we selected soft printable materials that could be printed at millimeter to centimeter scales, more than 30 layers thick, while achieving the desired range of leg stiffness in all dimensions, in order to ensure a wide design space. We compared two commercial soft filaments: thermoplastic elastomer (TPE)[1] with a Shore hardness of 92A, and thermoplastic polyurethane (TPU)[2] with a Shore hardness of 95A. The Young's modulus of the TPE is reported as 7.8 MPa in the datasheet, whereas the Young's modulus of the TPU is reported as 26 MPa. Although the difference in the hardness between the two materials is relatively small, the TPU 95A 's higher stiffness supports our target payload and deflects less at the same dimensions compared to the TPE, while demonstrating the dynamic behavior desired for terrestrial locomotion. Thus, we selected the TPU 95A as the prototyping material.

Based on the results from Sec. 5.4.1, a number of prototypes with $\phi = 90^\circ$ and $\phi = -90^\circ$ were manufactured with all other design parameters held constant, as shown in Fig. 5.7(b).

[1] Arkema 3DXFLEX™ TPE

[2] Ultimaker TPU 95A

The beam is right-handed chiral if $\phi > 0$ and left-handed if $\phi < 0$. The design diagram is shown in Fig. 5.7(a); design parameters can be found in Table 5.2.

Table 5.2: Twisted Beam Design Parameters

Parameter	Symbol	Value	Unit
Beam length	l	50	mm
Beam width	w	20	mm
Beam thickness	t	3	mm
Beam total twist angle	ϕ	90	degree
Beam segmental twist angle	α	45	degree

5.5.1 Contact Friction V.S. Resulting Motion

The different motion patterns of the shaking beam can be attributed to the prevailing friction conditions. To investigate the impact of the friction coefficient on the system's behavior, we conducted a series of MuJoCo simulations with varying contact friction conditions. The outcomes are depicted in Fig. 5.4(b) and (c). In our MuJoCo model, we employed the elliptic cones contact model with six dimensions to represent the contact. This model utilizes five parameters $\{f_1, f_1, f_2, f_2, f_3\}$, as shown in Fig. 5.4(a), to describe the friction coefficient of the contact surface. Here, f_1 corresponds to the tangential friction coefficient in the -X and -Z directions, f_2 represents the rotational friction coefficient along the -X and -Z axis, and f_3 denotes the torsional friction coefficient along the -Y axis. We conducted simulations using the proposed simplified model in MuJoCo to investigate the impact of varying tangential friction coefficient f_1, which are presented in Fig. 5.4(b), and the impact of different rotational friction coefficient f_2, which are shown in Fig. 5.4(c). The results demonstrate the significant influence of both tangential and rotational friction

coefficients on the resulting motion. As the friction coefficient increases, the resulting trajectory diminishes in scale due to higher energy loss, and the contact location also shifts with alterations in the friction coefficient. This outcome underscores the pivotal role of the friction coefficient in determining the resulting motion and emphasizes its relevance for further investigation.

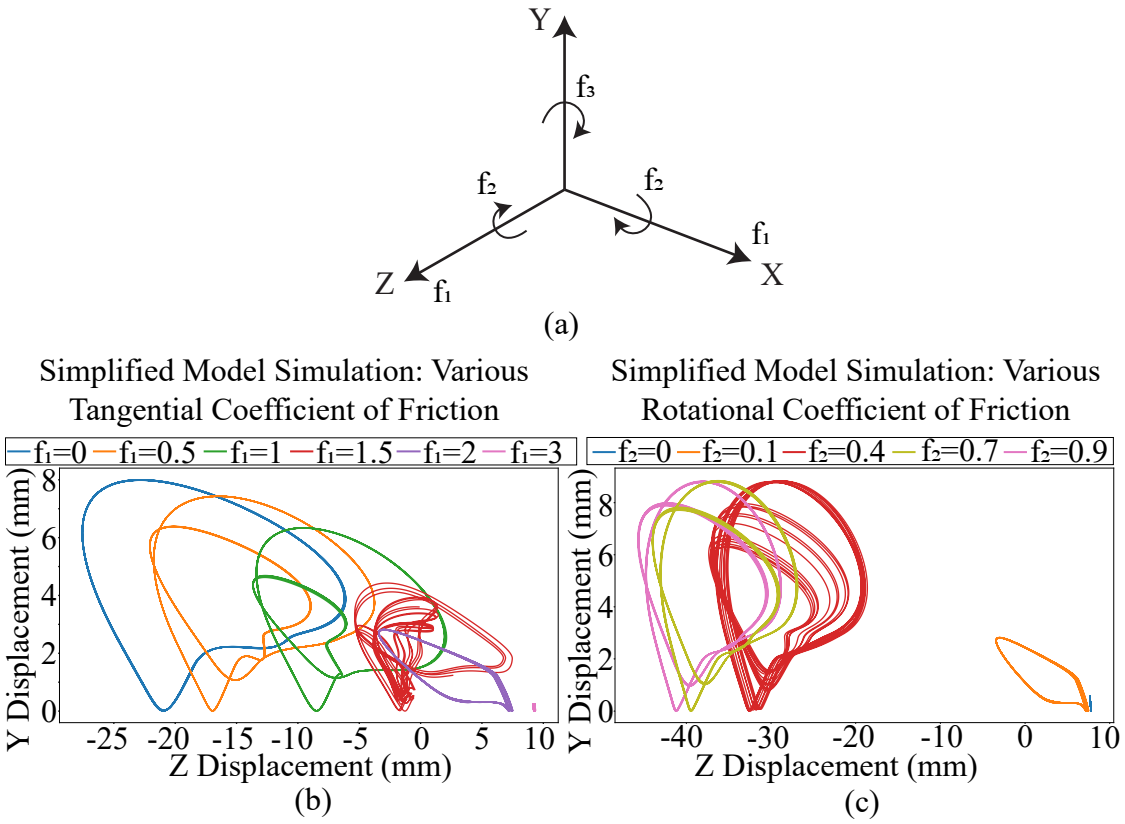

Figure 5.4: **Single beam contact simulation with various contact friction conditions. (a):** Contact Model; **(b):** Resulting motion with various tangential friction coefficients; **(c):** Resulting motion with various rotational friction coefficients.

5.6 Prototype Tests

The results of our experiments demonstrate how vibrating, twisted beams with terrain interactions exhibit similar behavior in real life to model-based results.

5.6.1 Frequency Sweep Test

This set of tests shows how the beam responds differently at varying input frequencies as a function of its chirality. We conducted tests on two beams with $\phi = \{90^\circ, -90^\circ\}$. For each test, the motor's frequency was swept from 1 Hz to 45 Hz in increments of 1 Hz. The results may be seen in Fig. 5.5.

The two plots on the left of the Fig. 5.5 show the major and minor axis lengths of the approximated ellipsoidal path at each frequency, which vary significantly across the range of input signals. A few frequencies of note are highlighted in green and brown, respectively. Because we are interested in generating positive net work through ground interactions, we are interested in frequencies that produce large, circular paths (where the magnitudes of axis lengths are high and the ratio of major:minor axis lengths is closer to 1:1). These frequencies, highlighted in green, can be contrasted against frequencies where the minor axis' length is closer to zero, producing a linear trajectory, noted in brown. The path orientation of the end effector's trajectory is also noted in each green plot by orange arrows in Fig. 5.5. We can conclude that, as in our simulation results in Sec. 5.4.1, the beam's chirality determines this orientation. This is confirmed by comparing Fig. 5.5(a) and (b) across all elliptical paths.

5.6.2 Offset Load Test

The design and placement of leg masses can play a significant role in the dynamics and harmonics of twisted beams as well. This section highlights how inertia can amplify the motion seen previously, as well as influence the production of frequency-dependent orientation changes in the output trajectory. We interpret this as a result of the complex interactions with the beam's coupled, chiral stiffness.

We conducted four frequency sweep experiments on two beams with $\phi = \{90^\circ, -90^\circ\}$.

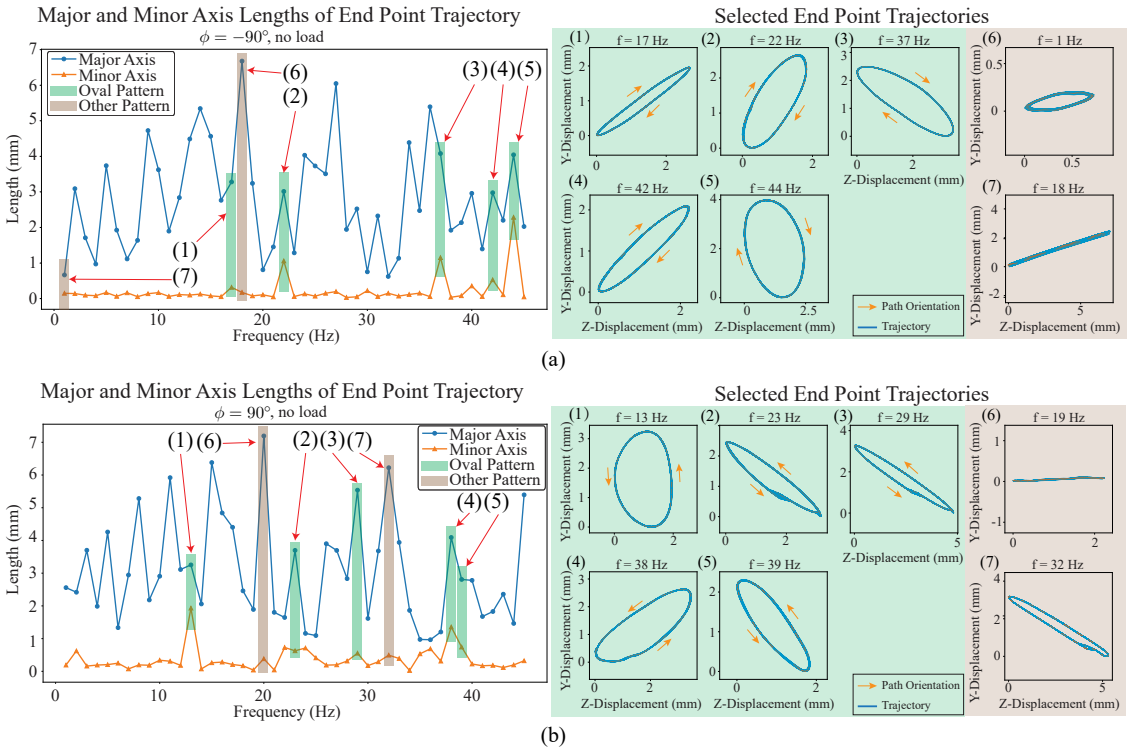

Figure 5.5: **Results from frequency sweep tests: major and minor axis lengths of the beam end point trajectory and selected end point trajectories (a):** Twist angle $\phi = -90°$. **(b):** Twist angle $\phi = 90°$.

In each test a 20 g load was attached to a different corner of a plastic, 3D-printed frame (which we call the load frame), as shown in Fig. 5.7(b). Detailed end point trajectories at each frequency can be found in Section 4 of the supplemental document. Here for demonstration, we processed data with $\phi = -90°$. The processed results are shown in Fig. 5.6. Compared to the data from the unloaded beam in Fig. 5.5, we can see that the trajectories are qualitatively more elliptical at lower frequencies. Moreover, compared to the unloaded experiment, we see in all four cases that the path orientation reverses at least once through all the sampled frequencies. The specific frequency at which this reversing effect occurs is clearly a function of the loading conditions, this demonstrates how inertia and mass can play an important role in producing highly differentiated output trajectories

as a function of frequency.

5.6.3 Single Beam Contact Test

This experiment demonstrates how the output trajectory and its orientation can be influenced by the input signal driving frequency in the presence of highly nonlinear ground interactions. This section demonstrates a relatively constrained, prescribed experiment, whereas the next section demonstrates the same phenomonon observed in a less prescribed manner with a free-walking platform.

The test setup in Fig. 5.7(c) and (d) shows a linear stage whose oscillating, forward-backward motion is dictated by the rotating crank of a brushless motor[3]. The motor is controlled by an ODrive[4] motor control board. We again use (5.12) to control the speed of the motor, with $A = 2\,\text{mm}$, and $f = \{1-40\}\,\text{Hz}$. The beam is mounted to the linear stage and optical tracking markers are mounted to the proximal and distal ends of the beam. An OptiTrack Prime 17W optical motion tracking system is then used to track the position of the system at a rate of 360 Hz. A plate with four load cells mounted perpendicularly in sets of two, to measure contact forces between the leg and ground along the Y and Z axes, as shown in Fig. 5.7(c) (normal and tangential to the ground, respectively). The test setup is shown in Fig. 5.7(d) and the test results are shown in Fig. 5.8. The beam sample with $\phi = 90^\circ$ was used, and the mass of the foot is represented by a 20 g load attached to the lower left corner of the load frame. The length of the rigid foot is 66.5 mm, and the distance between the translational stage and the plate is $h = 72\,\text{mm}$ as shown in Fig. 5.7(c). Therefore the contact distance between the foot at its unload, natural position and the plate, as depicted by h' in Fig. 5.7(c) is fixed at 5.5 mm.

Typical trajectories have been selected and plotted in Fig. 5.8(a). As can be seen, the

[3]ODrive Dual Shaft Motor D6374 - 150KV

[4]Odrive V3.6 High Performance Motor Control.

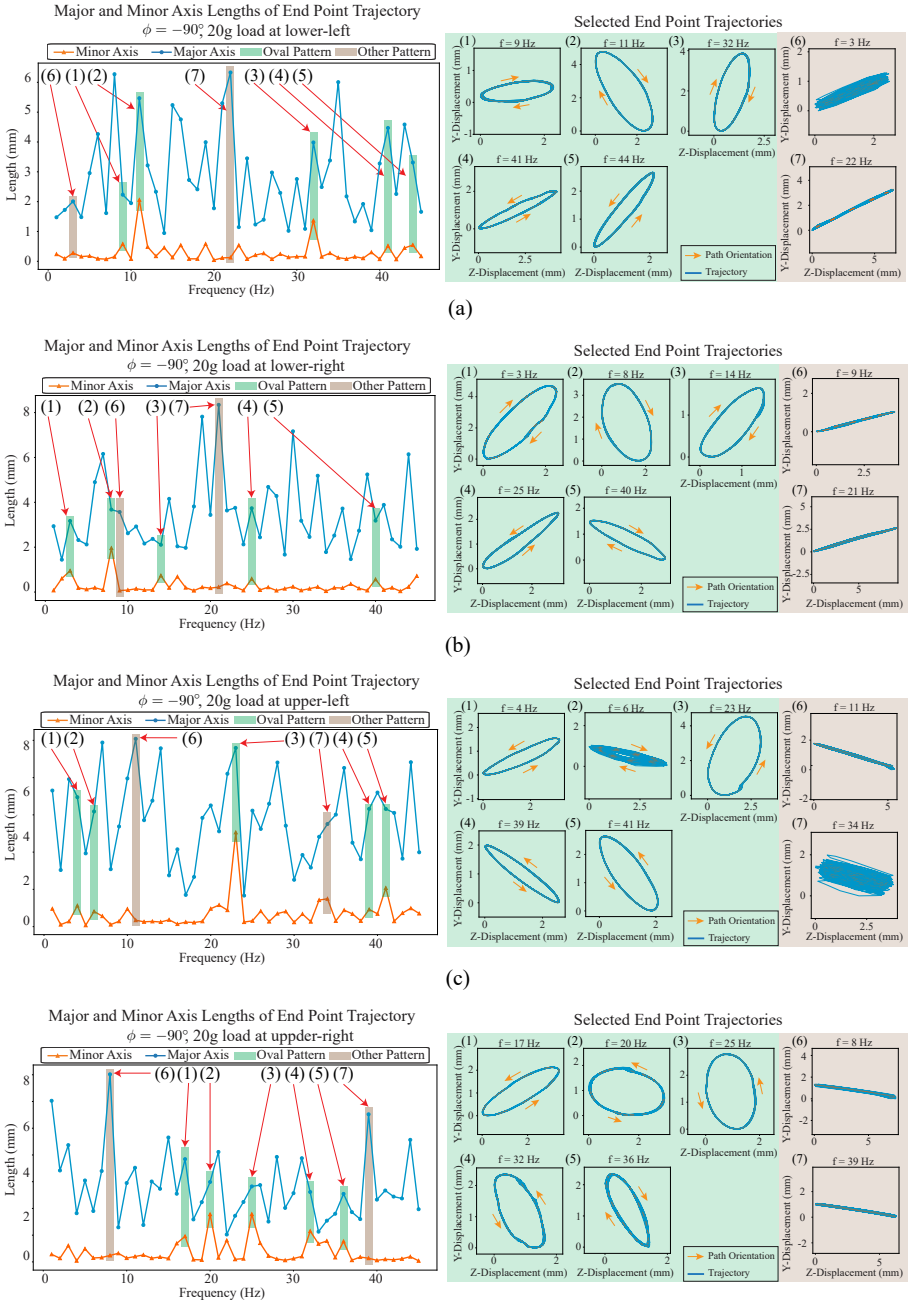

Figure 5.6: **Results from offset load tests: major and minor axis lengths of the beam end point trajectory and selected end point trajectories with twisted angle $\phi = -90°$. (a):** Offset load at lower-left. **(b):** Offset load at lower-right. **(c):** Offset load at upper-left. **(d):** Offset load at upper-right.

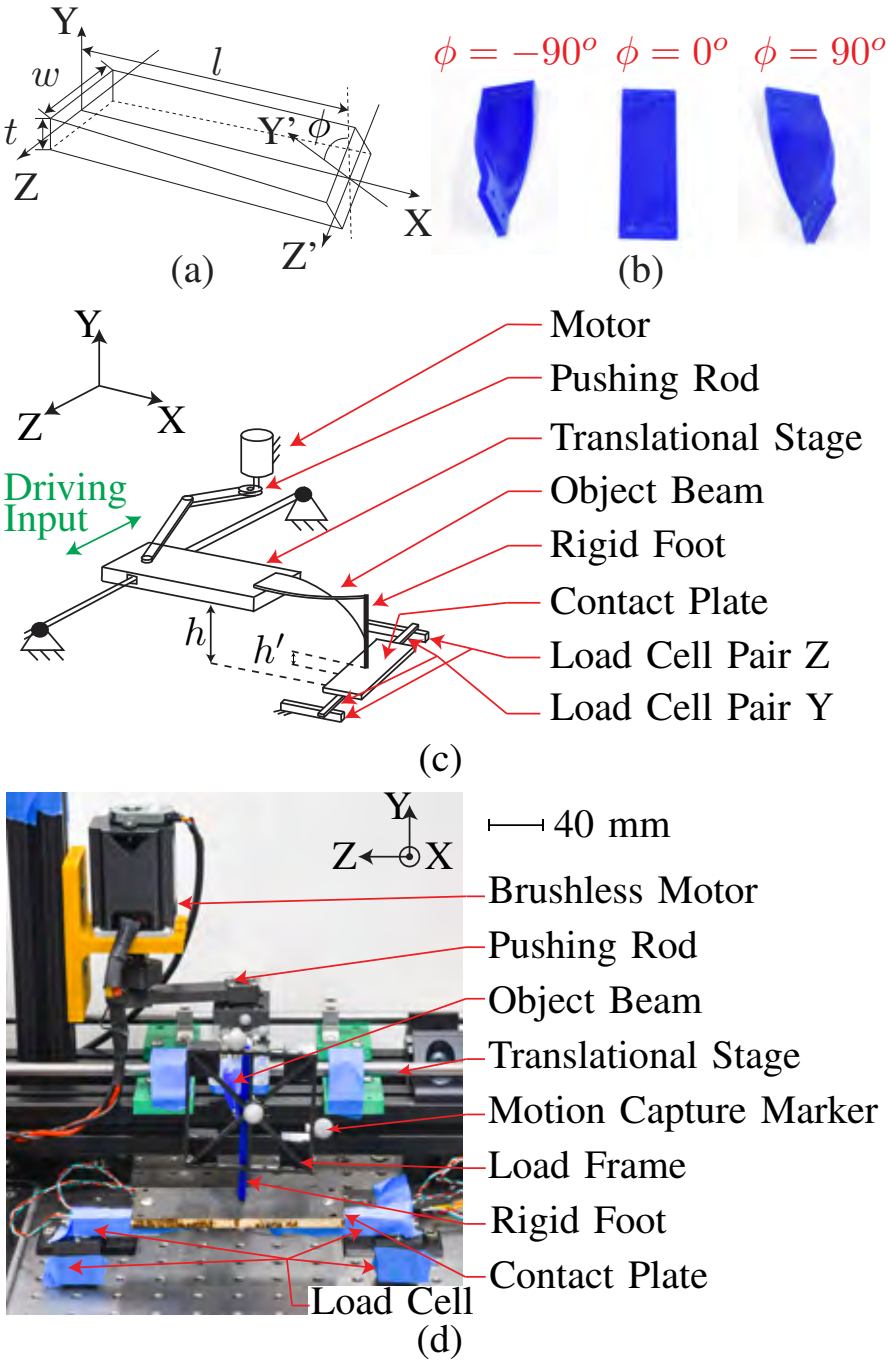

Figure 5.7: **Lab test setups. (a):** Design diagram of the twisted beam. **(b):** Beam prototype samples. **(c):** Sketch of lab test setups. **(d):** Lab test setup for single beam contact tests

trajectory evolves as a function of input frequency. In the low-frequency region, where the input frequency is less than 18 Hz, contact interactions dominate the motion observed in the leg, because the "foot" never breaks contact with the ground. This results in trajectories which are a flat line along the Z axis. As the input frequency increases to 26 Hz, ground contact becomes more intermittent and the leg's motion becomes dominated by its own dynamic properties. This results in trajectories that look like a figure '8', or a loop with a single inversion. At the point of contact, the inverted trajectory results in a change in the direction of motion, shown by the orange arrows in Fig. 5.8(a). At frequencies higher than 38 Hz, the trajectory inverts a second time and the direction of motion at the point of contact reverses again.

The tangential forces measured by the load cells also capture direction changes at the same transition frequencies. In Fig. 5.8(b), two typical force data are plotted at frequencies of 26 Hz and 40 Hz. By comparing the tangential forces, one can see that the direction is opposite, in line with the change in motion observed in Fig. 5.8(a). The vertical force data can be used to capture the contact frequency, which is not necessarily the same as the driving frequency. Since contact dominates at frequencies below 18 Hz, we focus on frequencies from 18 Hz to 44 Hz. The result is shown in Fig. 5.8(c). We highlight three distinct shapes observed with different colors. In each regime, the contact frequency increases with the input frequency. At the transition frequencies noted previously (26 Hz and 38 Hz), the contact frequency drops by ($\frac{1}{2}$ and $\frac{1}{3}$, respectively), the same frequencies at which the foot's trajectory inverts itself and then reverses its direction of motion (and force) on the ground.

It should be noted that this experiment was conducted at a fixed height off the ground. The next section explores how a less-constrained system exhibits similar behavior to produce controllable, walking gaits.

5.6.4 *Walking Tests*

This test demonstrates how the proposed twisted beam can be leveraged to produce a controllable walking gait that can be easily tuned from a single vibrational input.

Two twisted beams serve as robot legs with $\phi = 90^\circ$ and $\phi = -90^\circ$, respectively, are mounted in a mirrored fashion across the robot's sagittal plane to a carbon fiber plate. A Maxon brushless motor[5] along with a 40 g offset load is fixed to the plate, serving as a rotary actuation input. The test setup is shown in Fig. 5.9(a). A vertical slider connects the robot to two translational stages so that the motion of the robot is constrained along the x-axis and about the yaw axis, while the motion about and along the roll, pitch, z-axis, and y-axis is permitted. A cart with a 100 g load is attached to the robot's tail for support and balance. The total length of the walking platform is 295 mm; the total weight is 323 g.

During this test, the motor was commanded to drive the robot at various frequencies from 1 Hz to 80 Hz in 1 Hz increments. A high-speed camera [6] was used to record the position of the robot at the rate of 1000 fps. Test videos can be found in the supplemental video. Fig. 5.9(b) presents a cycle of the walking gait at the actuating frequency of 65 Hz. Fig. 5.9(c) shows the trajectory of the robot in 1 second. In this test, the robot reached the averaged walking speed of 156.3 mm/s with a 65 Hz actuating input frequency. In addition to walking forward, the robot was also able to move backward at a speed of 35.7 mm/s at an input frequency of 23 Hz. The actuation frequencies used for walking forward and backward in these tests differ from the single beam contact test result as shown in Fig. 5.8(c). This difference can be attributed to 1) Different weight of the driving object, as a single beam is less than 50 g while the walking system is 323 g with two beams; 2) Different contact circumstances, as the timing of two feet contacting the ground can influence each other in as yet unstudied ways; and 3) External friction from the walking test platform. This

[5]Maxon EC 45 flat Ø42.9 mm, brushless, 30 Watt, with Hall sensors

[6]Edgertronic SC1, https://www.edgertronic.com/our-cameras/sc1

result demonstrates how foot motion can be tuned by altering a single actuator's input frequency, showing potential for controlling the walking direction and speed of a fully legged terrestrial robot.

5.7 Discussion

Our results demonstrate, through simulation and single beam experiments with contact, that the coupled stiffness of twisted beams can be easily controlled to generate a variety of complex motions by simply changing the beam's input frequency. The results presented above suggest a rich space for control, even from simple actuation sources. These experiments also reveal how highly nonlinear ground contact influences the system's dynamic behavior, which supports the design of walking robots inspired by this phenomenon.

Our experiments progressively move from single beam contact tests to less-constrained studies of system motion with multiple legs in contact with the ground. Through the successive release of constraints, we have demonstrated that the underlying dynamics continue to be influenced by both beam design parameters and input signals. As we continue to release constraints and add legs, we anticipate further challenges with regard to the synchronization of multi-legged systems against the complexity of multiple points of contact vibrating at high speed against the ground. We believe that these topics are outside the scope of the current study, in which we have primarily focused on the role of design and actuation inputs on single-beam behavior.

Some limitations have also been observed throughout the study. To begin with, we observed that the beam heats up over the course of a long data collection run, which alters material properties such as stiffness and elasticity, impacting results. To address this issue, future designs will integrate materials with lower viscoelastic loss modulus, higher temperature coefficient of Young's modulus, and optimized geometries to reduce shear stresses under vibration, in order to reduce the impact temperature plays on the system's shifting

dynamic properties. Another limitation of this work is the lack of a full-body simulation of a multi-legged robot. Simulating our system is challenging because it involves multi-point, soft-body contact with the ground – highly nonlinear interactions that require heavy computation. We plan to employ the newly proposed simplified beam model to simulate the system-level dynamics at faster rates. Once developed, this simulation would permit mechanical design optimization and controller design for understanding the full suite of capabilities in this new legged robot.

5.8 Conclusion

In this work, a mechanism for propagating vibration through soft twisted beams with ground contact is proposed for simplifying the actuation of walking robots by taking advantage of these beams' dynamically-coupled anisotropic stiffness. A simplified model has also been proposed to quickly simulate the nonlinear dynamic behavior of soft twisted beams. Using dynamic simulation and experimental approaches, we have shown that the coupled stiffness of twisted beams with terrain contact can be controlled to generate a variety of complex trajectories by changing the frequency of the input signal. This work also reveals how highly nonlinear ground contact influences the system's dynamic behavior, supporting the design of walking robots inspired by this phenomenon. Future work will explore manufacturing and design strategies for improving consistency between SCRAM elements and minimizing energy loss due to heat. Future work will also include studies on extending the versatility of this concept for locomotion in various media like water and air with gaits like swimming and flapping.

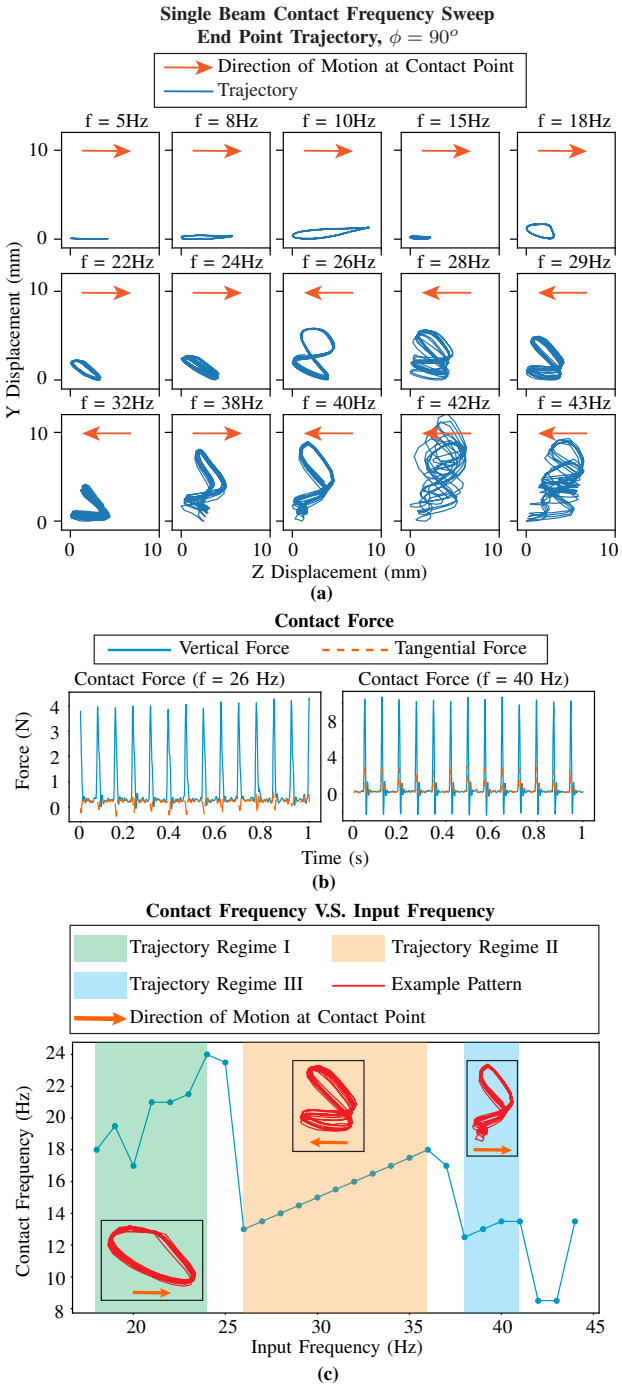

Figure 5.8: **Results from single beam contact tests. (a):** Selected end point trajectories. **(b):** Contact force data in two directions. **(c):** Single beam contact test result: contact frequency as a function of the input frequency.

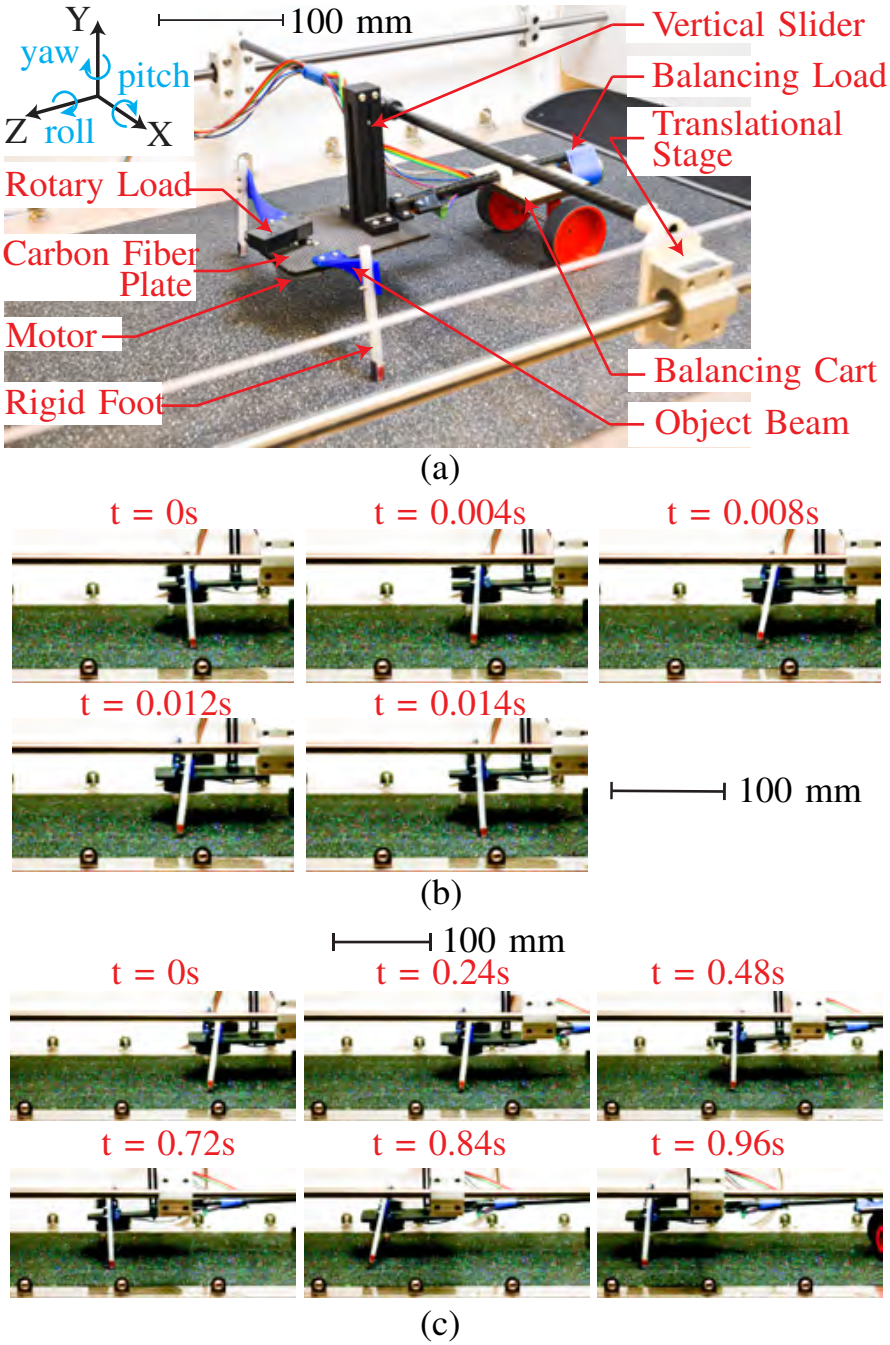

Figure 5.9: **Results from walking tests. (a):** Walking test setups. **(b):** One cycle of walking gait when walking forward. **(c):** Walking trajectory in 1 sec.

Chapter 6

MODELING SCRAMS USING PSEUDO-RIGID BODY MODELING

6.1 Introduction

In recent years, there has been a notable surge in research interest regarding the modeling of soft robotic systems. This is primarily driven by the substantial challenge and growing need to accurately model and simulate the intricate nonlinear and hysteresis characteristics exhibited by soft structures. The conventional approach to modeling and simulating soft robotic systems involves using the finite element method (FEM). While FEM allows for analyzing structural strength and dynamic behavior across various scenarios, it necessitates a large number of nodes to mesh and represent the high degrees of freedom associated with soft structures. As a result, this computational requirement leads to significant costs and introduces undesirable delays in online control algorithms. Additionally, FEM relies heavily on precise material properties for accurate calculations, which can be problematic due to manufacturing variations among different components.

The aforementioned limitations also present significant obstacles in the design optimization and dynamic simulation of SCRAM devices, particularly in the context of our study where we focus on swimming and walking robots. These applications involve interactions with various media such as water, ground, and granular materials, which further amplify the computational costs and render the finite element method (FEM) impractical. Therefore, there is a pressing need for a simplified, computationally efficient, and precise modeling approach that can effectively simulate and capture the dynamic behavior of SCRAM devices during swimming and walking.

As can be seen in the aforementioned studies, I applied a simplified modeling method

using a pseudo-rigid body (PRB) model to simulate the dynamic behavior of SCRAM robots. Differing from the FEM models, the proposed PRB model uses discrete rigid bodies connected by spring-damper joints to replicate the specific dynamic behavior. By reducing the number of degrees of freedom (DOF) through a set of principled assumptions about deformation, a more computationally efficient PRB representation can be used within off-the-shelf rigid body simulators, which solve problems of contact and friction more efficiently, allowing us to explore the system-level dynamics of the SCRAM robots more thoroughly.

Using the aforementioned case studies as illustrative examples, this section seeks to present the generalized workflow of the proposed pseudo-rigid body model. The objective is to provide fresh perspectives and guidance to researchers working in the field of soft robots.

6.2 Workflow

The generalized workflow, depicted in Fig. 6.1, illustrates the process of developing a PRB (Placeholder for the model) model, which can be divided into four distinct steps.

Step 1: Observing Behavior

The initial step involves observing the static and dynamic behavior of the target device, which may vary depending on the specific behavior being modeled. This process can vary, based on the specific behavior that will be modeled. For example, in the case study discussed in Ch. 4, a series of sliding-pushing tests were conducted to measure the stiffness change and critical buckling limit variation of a fin in opposite directions using a linear gauge. In the case study presented in Ch. 5, however, a set of bending and twisting tests were performed using a UR5 robotic arm.

Step 2: Developing Canonical Model

During the second step of the proposed modeling workflow, the main objective is to develop the canonical model based on the insights obtained from the previous step. This model is constructed using a series of rigid links and spring-damper joints, where the specific values for spring stiffness, damping, and other design variables are yet to be determined. By connecting these links and joints at various positions and angles, it becomes feasible to qualitatively reproduce the observed dynamic behavior. For instance, two distinct motions were observed during the test in the case study discussed in Ch. 4. The first motion involves the rotation of the fin around the tubular body, which can be modeled using a pin joint with linear spring-damper characteristics. The other observed motion is the variation in buckling limits in two opposite directions during the fin's rotation, which can be modeled using a nonlinear torsional joint with different spring stiffness in each direction. In the case study presented in Ch. 5, the model aims to replicate the diverse bending stiffness in orthogonal directions and the twisting torsion along the beam axis. As a result, I have designed the PRB model incorporating a series of links and pin joints positioned at different locations and orientations. This configuration allows for the replication of the dynamic oval-like pattern observed at the beam's end-effector when actuated by a shaking input.

Step 3: Lab Dynamic Testing

At this stage, a preliminary canonical model has been constructed, with the variables yet to be determined. Consequently, the third step of the proposed modeling workflow involves conducting a series of laboratory dynamic tests to acquire reference data for fitting these variables. These tests need to be designed to enable the replication of the desired dynamic behavior of the target device while maintaining a simple test setup. For example, in Ch. 4, the test was designed to fix the device underwater and induce tube deformation, recording

the thrust force in two directions. Similarly, in Ch. 5, the test was designed to capture dynamic positional data of the beam's end-effector during the recovery process after release from a load. This step aims to gather crucial data that contributes to understanding the specific dynamic behavior exhibited by the target device. Other dynamic parameters such as mass and dimensions can be obtained through direct measurement or from manufacturers' data sheets.

Step 4: Fitting the model

The final step of the proposed modeling workflow involves fitting the undetermined variables using the data obtained from the laboratory tests conducted in the previous stage. To initiate this process, simulations are performed using the same setup as the lab tests. The choice of simulator depends on the specific application. For instance, in Ch. 4, a Python-based symbolic dynamic solver called Pynamic is utilized for simulating the process [1]. Conversely, in Ch. 5, MuJoCo, a rigid body simulator, is employed [124]. Following that, optimization algorithms can be employed to fit the model variables by minimizing the average error between the simulation results and the reference data obtained from the laboratory experiments. The objective function for the optimization process can be expressed as:

$$Min\left\{\sqrt{\sum_{j=0}^{n-1}\sum_{i=1}^{m}\left[(M_i(j)-\hat{M}_i(j))^2\right]/(m\cdot n)}\right\}. \tag{6.1}$$

The simulation data obtained from dataset i at time step j is denoted as $M_i(j)$, while the corresponding state obtained from the laboratory experiments is represented as $\hat{M}_i(j)$. In this context, $n-1$ represents the total number of data sampling steps for each test, and m represents the total number of datasets collected. The algorithm described in Equation 5.13 was applied with three sets of data ($m = 3$), where displacements in three orthogonal

[1] **pynamics:** https://pypi.org/project/pynamic/

directions were recorded. At this stage, the PRB model has been determined and can be applied to the simulator for conducting future simulations.

6.3 Discussions

This chapter sheds light on providing general guidance for the development of order-reduced models for soft robots using the pseudo-rigid body modeling method. The effectiveness of this method has been validated through case studies presented in Ch. 4 and Ch. 5, demonstrating its ability to provide accurate dynamic simulation results with low computational cost. The resulting model is a rigid-body model, making it compatible with widely used and commercially available rigid-body simulators that offer high computational efficiency. Additionally, the model fitting process, which involves calibrating the model based on specific prototypes, enables the resulting model to accurately capture manufacturing variations. Furthermore, the high computational efficiency of the method allows for its application in data-intensive tasks such as design optimizations and data-driven controls, where numerous simulations need to be executed to gather extensive datasets.

While the PRB model has demonstrated numerous strengths, it is important to acknowledge the existence of limitations in certain scenarios. Firstly, the proposed PRB model is specifically designed to capture and replicate certain targeted behaviors of the objective device, rather than providing a generalized model like Finite Element Method (FEM) models. This limitation may restrict its applicability in cases that require a broader and more comprehensive model capable of representing various behaviors exhibited by the target structure.

Additionally, the accuracy of the resulting PRB model heavily relies on the quality and precision of the dynamic lab test data. Inaccurate or imprecise test data may lead to less accurate model predictions. Hence, careful consideration and precise execution of the dynamic lab tests are crucial to ensure reliability of the model.

Moreover, the proposed PRB model needs to be calibrated for each application to match the characteristics of the specific prototype. This calibration process may not be suitable or feasible in situations involving numerous prototypes or prototypes that are challenging to calibrate accurately.

Future research in the field of SCRAM system modeling can concentrate on developing innovative modeling methods that significantly reduce simulation time while accurately generating a comprehensive model capable of replicating various dynamic behaviors of the target structure. This advancement would enable the application of real-time model predictive controls. Additionally, future work can focus on establishing a connection between real prototypes and the model, allowing simulations to accurately depict the behavior of the actual prototype in real-world environments. To achieve this, the modeling process should be capable of gathering information from the surrounding environment, including factors such as temperature, friction, drag, and more. By incorporating these environmental influences, the model can effectively learn and predict the robot's dynamic interaction with the environment, facilitating precise and fast simulations.

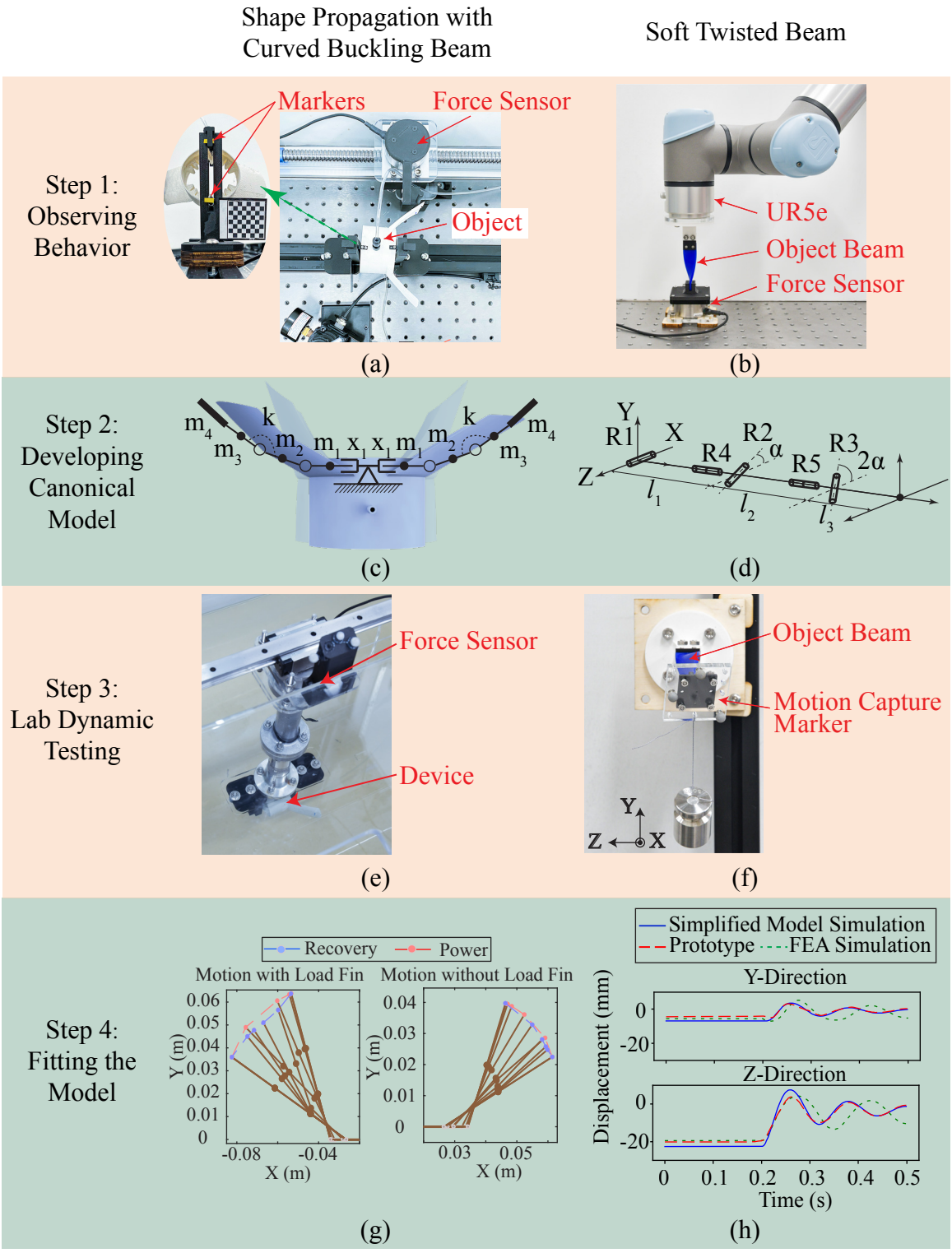

Figure 6.1: Workflow of pseudo-rigid body modeling method

Chapter 7

MANUFACTURING SCRAM DEVICES

7.1 Introduction

This chapter delves into the manufacture of SCRAM devices and aims to offer insights and criteria for selecting appropriate manufacturing methods to fabricate these devices.

Traditionally, soft robots predominantly utilize silicone-based materials, making molding the manufacturing method that has gained widespread acceptance in the soft robotic community. I have also utilized this technique to fabricate SCRAM devices, as demonstrated in Figure 7.1 (a) and (b). In these examples, soft twisted beams with diverse material and geometry designs were molded, resulting in high-quality parts. However, when conducting research on design optimization and dynamic behavior modeling, there is a need for prototypes with diverse designs and materials. This requirement renders molding unsuitable due to the significant time and cost involved in creating molds for each design. Examples can be found in 7.1 (c) and (d) which illustrate two molds created for two specific designs as depicted in 7.1 (a) and (b). Each of these molds required approximately 15 hours of 3D printing time. Additionally, the incorporation of pneumatic actuation in many soft robots necessitates the use of air passages and bladders, resulting in a notable increase in structural complexity. As a result, difficulties may arise during the molding process, leading to final parts not being airtight, and lowering actuation performance. Molding is also a one-time process, meaning that no modifications can be made after the material cures. This limitation requires more iteration, taking more time, which increases the cost of development. Moreover, the molding process necessitates the expertise of well-trained and experienced professionals, making it inaccessible to the general public. This limitation

hampers the widespread use of soft robots in public domains, such as educational robots for K-12 education.

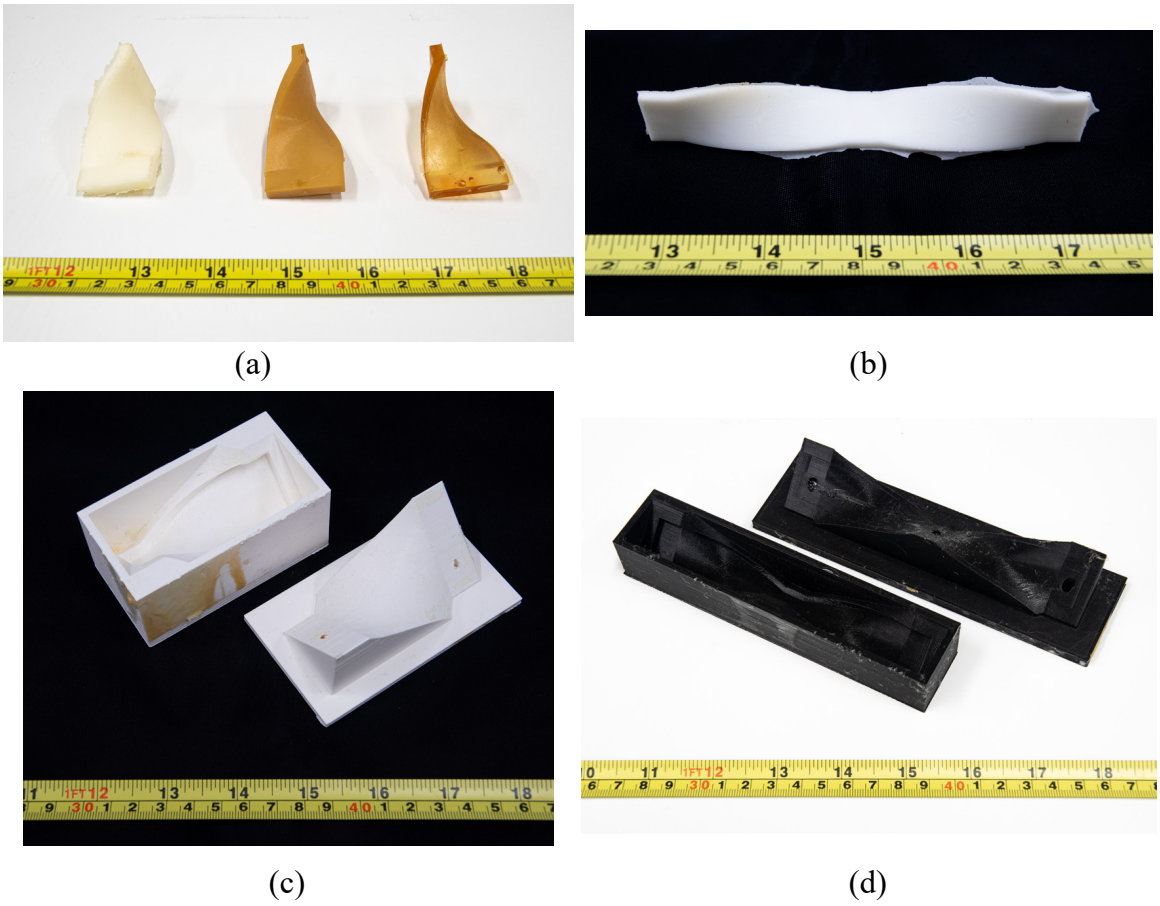

(a) (b)

(c) (d)

Figure 7.1: Example SCRAM prototypes made by molding.

3D printing has emerged as a widely adopted and highly advanced manufacturing technique in the soft robot applications. Unlike traditional molding, 3D printing offers superior capabilities in creating intricate structures, while significantly reducing the design process compared to mold design. Additionally, 3D printing has become more accessible to the general public, even without prior knowledge of soft robotics, as individuals can create soft robots using just a 3D printer and a well-designed file. Furthermore, dual-extruder 3D printers enable the simultaneous printing of two materials, expanding the range of design possibilities beyond what is achievable with the molding method. As shown in Fig. 7.2(a)

where a twisted beam prototype was printed using two different materials, with Thermoplastic Polyurethane (TPU) used for the beam prototype and Nylon utilized as supporting material. Additionally, Fig. 7.2(b) illustrates the development of a tubular structure using TPU and Nylon. Nylon, chosen for its rigidity and durability, was employed to hold the structural shape and create holes in the middle for tendon actuation, while TPU was used for the tubular body. More examples can be found in Fig. 7.2 (c) and (d), where the 3D printing method with Thermoplastic Elastomer (TPE) material was used to print curved beam, and paddling robot with pneumatic actuator, respectively. However, there are challenges associated with 3D printing in comparison to molding. One such challenge involves ensuring air impermeability for air passages and bladders. This arises from the common Fused Deposition Modeling (FDM) method used in most 3D printers. With FDM, the product is printed layer by layer, potentially leading to leaks between layers and inadequate air sealing. An instance illustrating this can be observed in Fig. 7.2(e), wherein the adherence quality between layers differs for prototypes produced using TPU and TPE. Additionally, standard 3D printers have limitations when it comes to material rigidity. Materials with lower rigidity can pose issues during the printing process, particularly during filament feeding. Furthermore, 3D printed parts are often highly variable in their quality and performance due to process variations. Factors such as inconsistent temperature control and filament quality can create flaws in prototypes, resulting in variations in the dynamic behavior of prototypes, even when they have the same design. An example can be observed in Fig. 7.2(f). Consequently, these limitations restrict the widespread use of 3D printing for manufacturing soft robots that require materials with lower rigidity and hardness.

The laminate fabrication method is also a popular manufacturing method in soft robotic applications. Drawing inspiration from origami systems, researchers have devised design and manufacturing methods that involve the utilization of multiple layers of various planar materials. Through 2D processes like lamination and laser ablation, these 2D materials can

be delicately designed and fabricated to enable the creation of 3D structures with multiple degrees of freedom capable of generating intriguing forms of locomotion. This method has been used extensively in micro-scale soft, capitalizing on the precise nature of laser cutting processes. Layer-based laminate fabrication is compatible with mass-production techniques, which can further lower the costs associated with the design, development, and distribution of robots, thanks to the low cost of 2D materials and the convenience of laminate-cutting processes. Nonetheless, there are certain limitations associated with this method. First, the materials employed in laminate fabrication primarily consist of thin planar materials that, in certain cases, may lack the necessary rigidity to adequately support the structure, leading to potential difficulties in control. Additionally, as the 2D materials are laminated together to construct 3D structures, issues of delamination can arise, impacting the overall performance and resulting in diminished durability of such robots.

The rest of this chapter discusses how the inherent characteristics of SCRAM devices, achieved through the utilization of structural anisotropy to simplify the structure and actuation, can address the challenges in the aforementioned manufacturing methods. By doing so, they hold the potential to decrease manufacturing costs, improve performance and durability, and expand the applicability of these manufacturing methods.

7.2 Criteria for Selecting a Manufacturing Method

Selecting the appropriate manufacturing method plays a crucial role in determining the performance of the device being produced. Hence, carefully choosing the manufacturing method when fabricating SCRAM devices is of utmost importance. This selection process closely aligns with both the design and the chosen material for fabrication.

For instance, in Ch. 3, the selection process commences with the evaluation of pinched tubes made from various materials to determine the optimal material, which turns out to be

TPU95A. Subsequently, the 3D printing manufacturing method is chosen due to its flexible nature in accommodating diverse designs and sizes and its compatibility with 3D printing TPU materials.

In Ch. 4, the preference for the 3D printing method over molding emerges despite the desirability of achieving superior air impermeability in pneu-net actuators. The decision to favor 3D printing stems from the intricate nature of the structure, involving a tubular body and interconnected side fins, making it impractical to use molding as a one-time solution.

Furthermore, in Ch. 5, although both 3D printing and molding can yield satisfactory prototypes, the 3D printing method is once again favored due to its superior ability to manufacture prototypes of varying scales and shapes. Opting for molding would necessitate creating new molds for each new design, leading to significant time consumption.

Drawing from the aforementioned case studies, I consolidate the key findings and outline general criteria for the selection of a manufacturing method when developing soft robotic devices.

- **Performance requirement:** The chosen manufacturing method must fulfill the performance requirements of the intended prototype. These performance requirements are determined by factors such as the prototype's operating environment, method of actuation, and specific application. For instance, underwater robots require a high level of waterproofing, while pneumatic-actuated robots rely on effective air-sealing performance. Additionally, in applications involving human interaction, both the manufacturing method and the materials used must be safe for humans.

- **Design complexity and materials:** The manufacturing method must be compatible with the specific design and material selection employed. For instance, the molding method may prove inadequate when dealing with complex structures. Similarly, for micro-scale robots, both 3D printing and molding might lack the necessary pre-

cision. Additionally, the choice of manufacturing method is influenced by material characteristics. For instance, materials with low rigidity may not be suitable for 3D printing, while uncured materials cannot be effectively utilized in molding. Moreover, materials that are difficult to laminate or laser ablate may not be appropriate for laminate manufacturing methods.

- **Time, cost, and expertise:** Time, cost, and expertise are also critical considerations when evaluating the manufacturing process. These factors hold significant importance, particularly in the prototyping and testing phase, where numerous prototypes with diverse designs are required for testing purposes. The selection of an appropriate manufacturing method can greatly impact time efficiency, labor requirements, and cost-effectiveness. For example, in the case study presented in Ch. 5, the dynamic behavior of the twist beams was heavily influenced by design parameters. Consequently, multiple prototype beams were manufactured to comprehend the relationship between these parameters and the resulting dynamic behavior. The molding method may not be suitable in this scenario, as it would necessitate creating a specific mold for each design, leading to time and cost inefficiencies. Furthermore, in applications beyond the realm of robotic communities, the expertise associated with manufacturing such products also assumes significance. For instance, in K-12 education, the manufacturing process should demand less expertise while ensuring safety remains a priority.

7.3 Discussion

Considering the aforementioned criteria, the implementation of the SCRAM concept can bring notable advantages to manufacturing soft robots. First, the SCRAM devices exploit the inherent anisotropy of curved planar structures to leverage the dynamic changes in their shape caused by material hysteresis and elasticity. This unique characteristic al-

lows them to generate high-dimensional nonlinear motions using simple actuation forces, resulting in a substantial reduction in the required actuation effort. This reduction leads to simplified structures, thereby expanding the range of compatible manufacturing methods. Additionally, the simplified structure of SCRAM devices enhances time efficiency and cost-effectiveness. As a result, the prototyping and testing phases are considerably shortened, yielding substantial time savings.

Although the SCRAM concept has shown significant advantages in improving manufacturing efficiency, limitations remain. SCRAM devices rely on soft curved structures, which makes them sensitive to manufacturing variability. For example, in the case study in Ch. 5, we found that, though they were printed using the same design file and the same printer, the 3D printed prototypes varied in material density and layer compactness. This variance resulted in different dynamic behavior observed during the test, which would prevent the same model parameters to be used even across the same design printed twice. This would require an extra calibration step for each individual part, a time-consuming step with potential performance implications on system performance. As a result of this limitation, we have developed a modeling method presented in Ch. 6. This method involves a simplified model with lower computational cost, enabling a fast and efficient calibration process. By employing this approach, we can accurately simulate the dynamic behavior of each prototype while accounting for manufacturing variations.

Additionally, for future use of SCRAM devices for reconfigurable amphibious robots, in order to reconfigure the geometry and control the dynamic behavior of the SCRAM device, actuators such as shape memory alloy (SMA) and pneumatic actuators will need to be attached to the body of the device, which will increase the complexity of the structure and will create new problems during manufacturing. Moreover, the rigid-soft paradox may also result in difficulties in manufacturing. For instance, when designing the walking robot in the case study in Ch. 5, on one hand, we want the twisted beam to be soft enough to

generate as big oval-like motion as possible, on the other hand, serving as the legs, the beam has to be rigid enough to support the body weight. This tradeoff constrains the materials, geometries, and manufacturing methods available to the designer.

In future research on manufacturing SCRAM devices, one area of focus could be the development of innovative multi-material manufacturing methods. These methods would expand the range of available materials for manufacturing, while still ensuring reasonable time costs and precision. By broadening the material selection, researchers would have more options to optimize the performance and characteristics of SCRAM devices. Additionally, future work can concentrate on innovative designs of SCRAM devices. The goal would be to create simpler structures that possess reconfigurability and can be manufactured with ease, without compromising the device's ability to achieve efficient and effective locomotion in various configurations. By optimizing the design, manufacturing processes can be simplified, making producing SCRAM devices more feasible and cost-effective.

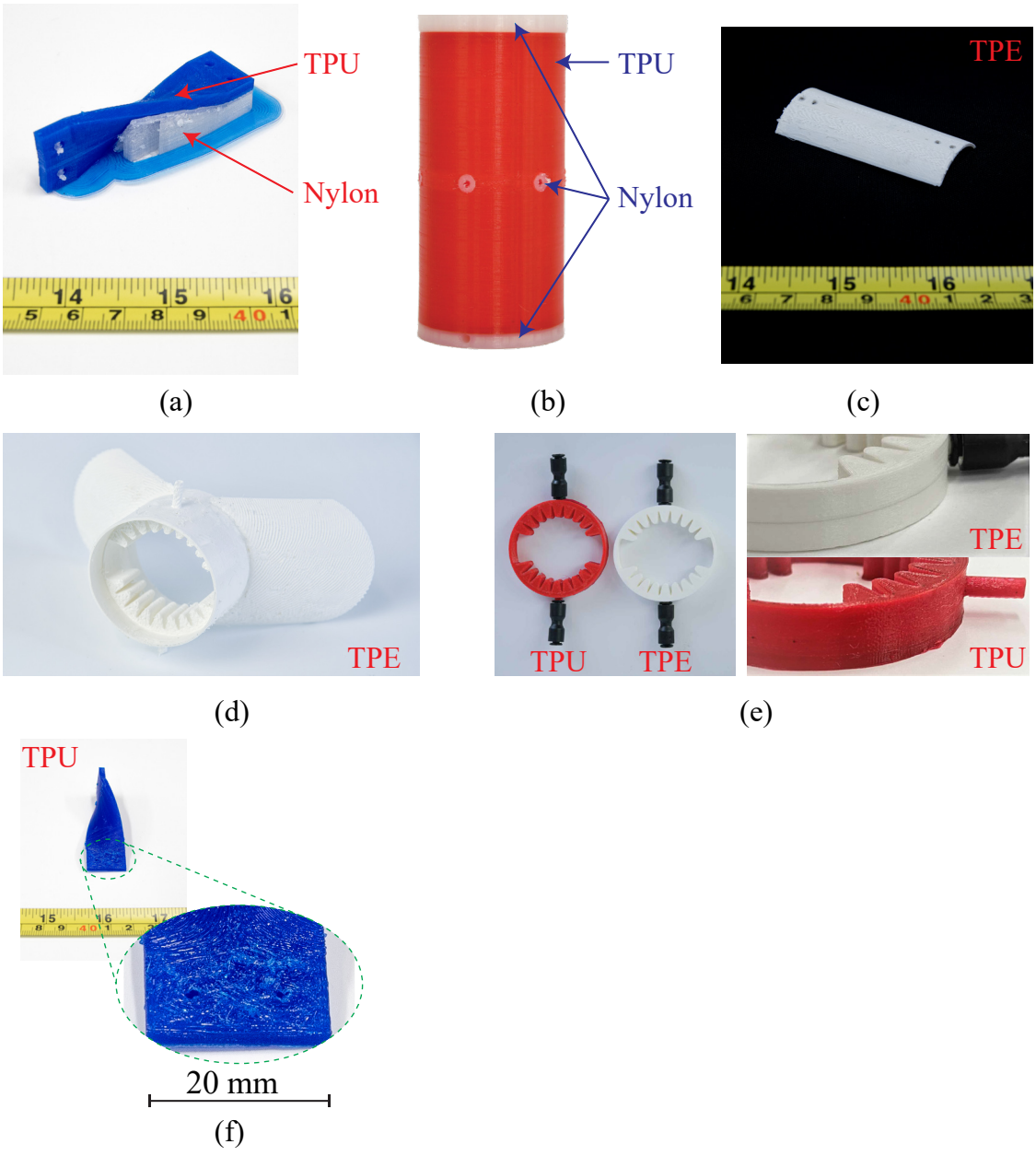

Figure 7.2: Example SCRAM prototypes made by 3D printing.

Chapter 8

CONCLUSION

This dissertation explores the curved geometry of thin elastic structures, which can undergo local shape changes and reconfiguration of mechanical properties when manipulated. This concept provides the foundation for a novel class of soft systems known as Soft Curved Reconfigurable Anisotropic Mechanisms (SCRAMs). Through the analysis of stiffness and shape change behaviors in three case studies, a comprehensive methodology is presented for the design, modeling, manufacturing, optimization, and control of diverse SCRAM devices capable of accomplishing various locomotion tasks.

This dissertation showcases the potential of the SCRAM concept through a series of case studies. The summary of the work can be found in Fig. 8.1. The initial case study in Ch. 3 explores the application of pinching-induced actuation in manipulating local surface curvature to adjust the stiffness of a thin-walled tube. The investigation reveals the correlation between the applied pinching force and the resulting tube deformation, demonstrating how multiple pinching forces can be combined to create a flexure hinge. Furthermore, the study examines the impact of pinching on local stiffness and underscores the possibility of using pinching forces to modify the stiffness properties of soft structures. Additionally, the dissertation demonstrates the practical implementation of the SCRAM concept in robotic arms, showcasing the ability to reconfigure the positioning and orientation of virtual joints along the arm to modify its workspace.

Our previous research [106, 107], as illustrated in Fig. 8.1(b), has uncovered that the utilization of preferential buckling in curved beams within swimming robots can passively reduce effective area during the recovery stroke, resulting in the generation of positive net thrust and moment. These curved beams can also be actively adjusted to modify their

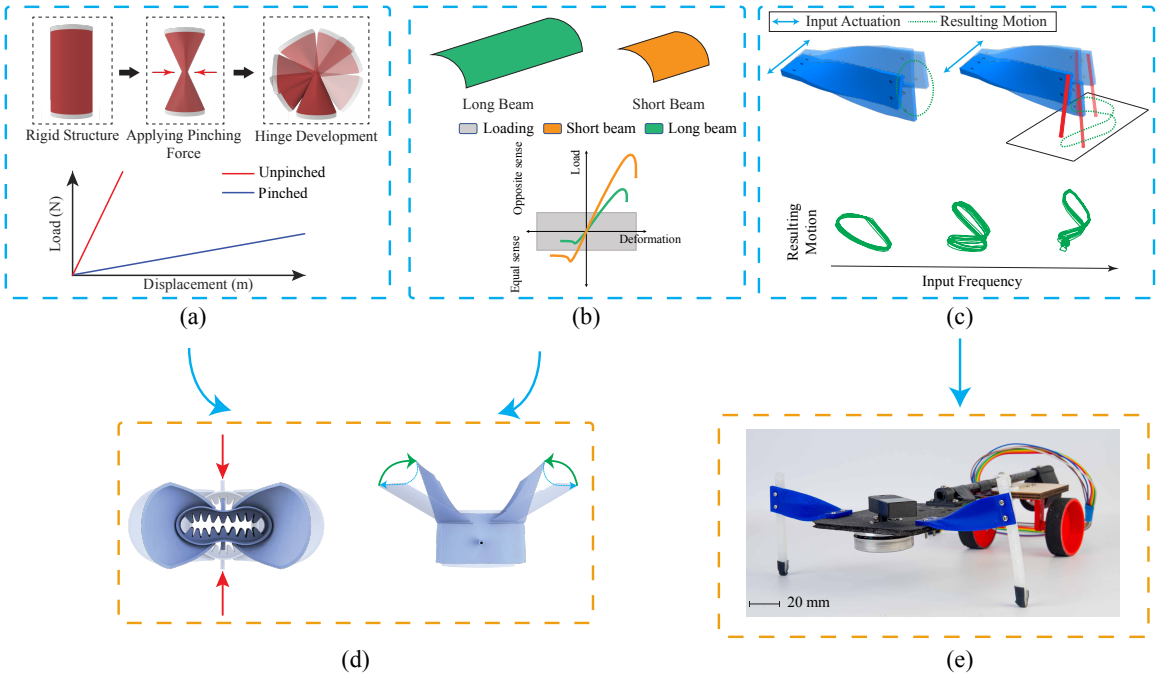

Figure 8.1: **Summary of works. (a):** Reconfigurable Soft Flexure Hinges via Pinched Tubes; **(b):** Preferential buckling curved beams for swimming robot; **(c):** Vibrational soft twisted beam; **(d):** Swimming robot using shape propagation mechanism; **(e):** Walking robot using soft twisted beam mechanism;

behavior as needed for swimming applications, allowing an underwater robot to switch between rowing and flapping gaits.

In the second case study in Ch. 4, we expand on the concept of buckling curved beams and concentrate on transmitting actuation forces through soft, curved materials for swimming purposes as shown in Fig. 8.1(d). This concept takes advantage of material mechanics to produce anisotropic stiffness and buckling behavior, which leads to an asymmetric paddling gait in the end-effector, mimicking a locomotion strategy observed in nature. This case study provides a summary of our ongoing work in comprehending the utilization of curvature change, shape propagation, buckling, and hysteresis in soft systems to simplify actuation and control complexity for swimming.

The third case study as in Ch. 5 investigates a mechanism for transmitting vibration through soft twisted beams that make contact with the ground, with the aim of simplifying the actuation of walking robots. This study explores how ground contact impacts the dynamic behavior of the system and demonstrates how the proposed twisted beam generates a controllable walking gait from a single vibrational input. Additionally, a modeling method is proposed in this study to rapidly simulate the nonlinear dynamic behavior of vibrational soft twisted beams. This method employs a pseudo-rigid-body approximation to reduce the model's complexity, generating a rigid body-based model suitable for dynamic simulations involving ground contact in tools such as MuJoCo.

In summary, this dissertation focuses on investigating three distinct categories of novel mechanism designs: soft pinching tubes, soft curved beams, and soft twisted beams. These mechanisms were then applied to develop two innovative robots capable of swimming and walking, respectively. The research demonstrates the potential of the SCRAM (Soft Curved Robotics for Actuation and Manufacturing) concept in addressing various challenges related to actuation, manufacturing, and modeling within the field of soft robotics. The introduction of these innovative mechanism designs and simplified modeling methods proposed in this study holds great promise for significantly impacting future research in the actuation, modeling, and manufacturing of soft robotic systems.

8.1 Impact and Future Works

Soft robotics is an emerging field with great potential, despite the numerous challenges that still need to be overcome. Via several case studies, this dissertation shows a promising solution to those challenges using the SCRAM concept. This dissertation mainly contributes to the field of soft robots by providing solutions to challenges in the actuation, modeling, and manufacturing of soft robotic systems.

- **Mechanism design:** This dissertation explores three specific mechanisms catego-

rized under the SCRAM concept: soft pinched tubes, curved buckling beams, and soft twisted beams. These mechanisms leverage reconfigurable anisotropy to generate asymmetrical motions, thereby reducing the need for extensive actuation to drive these motions. By integrating these mechanisms into maneuverable robots, the dissertation introduces two robots capable of swimming and walking, respectively. These examples demonstrate how the proposed mechanisms effectively address actuation and control challenges commonly encountered in traditional soft robots.

- **Modeling:** This dissertation tackles the modeling challenge of soft robotic systems by introducing a new pseudo-rigid body model that is computationally efficient and capable of accurately capturing the dynamic behavior of highly nonlinear systems. The effectiveness of the proposed modeling method is demonstrated through successful simulations of a shape-propagating paddling robot in an underwater environment and a walking robot using soft twisted beams with ground contact. These examples showcase the capability of the simplified modeling approach to generate fast and accurate dynamic simulation results for SCRAM robots.

- **Manufacturing:** This dissertation also investigates the manufacturing processes for soft robotics, with a focus on understanding the landscape of 3D printing over traditional fabrication methods. It delves into the aspects of achieving waterproofing, flexibility, rigidity, compatibility, and manufacturability in soft robotic structures.

Future work can be carried out from the following perspectives:

- **Adaptable robot:** The capability to modify their shape to accommodate various environments is one of the primary goals for soft robots. Through this dissertation, it has been demonstrated that SCRAM devices possess the potential to facilitate the active alteration of a robot's shape through simple actuation. Continued investigation

into this concept has the potential to result in the creation of increasingly sophisticated adaptive robots. One intriguing possibility, as explored in this dissertation, involves utilizing a tubular structure that can be manipulated to reconfigure its stiffness. A snake-like robot with reconfigurable stiffness can be developed by connecting multiple modules of such structures in different orientations and positions. This adaptable robot has the capability to effectively navigate and perform tasks in confined and dangerous environments, making it well-suited for exploration and rescue missions.

- **Smart, amphibious mobile robot:** Soft robotic systems offer distinct benefits due to their ability to change shape, enabling efficient adaptation of locomotion modes such as swimming, walking, and flying, depending on the surrounding environment. Leveraging these characteristics, amphibious robots can be developed, capable of seamlessly transitioning between different environments without requiring adjustment. Such robots hold tremendous potential in space exploration scenarios, where accessing remote areas may pose challenges for human presence. These robots can rely on their own capabilities to reconfigure themselves and select the most suitable maneuver mode for the given environment, enabling effective exploration and navigation in space. Amphibious robots have garnered significant attention in recent years, but research progress in this field has been sluggish. Given the SCRAM concept's ability to simplify actuation, it can also be leveraged to address challenges and create such robots. In addition, this endeavor will necessitate research into innovative materials capable of modifying their properties based on the surrounding environment. Such an approach can be incorporated into embodied intelligence, resulting in intelligent robots capable of adapting their locomotion autonomously to suit their surroundings without human intervention. To illustrate, the vibrating soft

twisted beam mechanism discussed in this dissertation shows the capability of producing diverse movements via manipulation of the actuation frequency. When the twisted beams are positioned in different orientations and locations, they exhibit diverse locomotion patterns through simple vibrational actuations, including paddling, walking, and flapping motions. This discovery holds immense promise for the development of amphibious robots that can achieve swimming, walking, and flying capabilities using the same actuation input, merely by adjusting the orientation and placement of these beams.

Furthermore, this application has the potential to inspire research in smart materials capable of exhibiting diverse dynamic behaviors, including variations in stiffness, elasticity, hysteresis, and more, in response to different environmental conditions like humidity, temperature, and gravity. This line of investigation could lead to the development of intelligent robots that possess the ability to automatically reconfigure their maneuver modes to adapt to their surroundings, thereby enabling enhanced performance and versatility in diverse environments.

- **Modeling and design optimizations of soft robots:** Soft robotic systems present modeling challenges due to their high degree of freedom and their materials' nonlinear, elastic properties, which result in computationally expensive simulations. As a result, simulation costs are a hindrance to both design optimization and control. Therefore, there is an urgent need for more efficient modeling methods. Future research aimed at developing rapid and precise modeling techniques could prove extremely beneficial for optimizing the design and implementing model predictive control for soft robotic systems.

8.2 Publications

8.2.1 Journal Papers

- **Y. Jiang**, F. Chen and D. M. Aukes, "Tunable Dynamic Walking via Soft Twisted Beam Vibration," in IEEE Robotics and Automation Letters, vol. 8, no. 4, pp. 1967-1974, April 2023;

- M. Sharifzadeh, **Y. Jiang**, and D. M. Aukes, "Reconfigurable Curved Beams for Selectable Swimming Gaits in an Underwater Robot," in IEEE Robotics and Automation Letters, vol. 6, no. 2, pp. 3437-3444, April 2021;

- M. Sharifzadeh, **Y. Jiang**, A. Lafmejani, K. Nichols, and D. M. Aukes, "Maneuverable gait selection for a novel fish-inspired robot using a CMA-ES-assisted workflow," in Bioinspiration & Biomimetics, vol. 16, no. 5, pp. 056017, August 2021.

8.2.2 Conference Papers

- **Y. Jiang**, M. Sharifzadeh, and D. M. Aukes, "Reconfigurable Soft Flexure Hinges via Pinched Tubes," 2020 IEEE/RSJ International Conference on Intelligent Robots and Systems (IROS), 2020, pp. 8843-8850;

- **Y. Jiang**, M. Sharifzadeh, and D. M. Aukes, "Shape Change Propagation Through Soft Curved Materials for Dynamically-Tuned Paddling Robots," 2021 IEEE 4th International Conference on Soft Robotics (RoboSoft), 2021, pp. 230-237;

- M. Sharifzadeh, **Y. Jiang**, A. Lafmejani, D. M. Aukes, "Compensating for Material Deformation in Foldable Robots via Deep Learning – A Case Study," 2022 IEEE International Conference on Robotics and Automation (ICRA), 2022;

- Sharifzadeh, M, **Jiang, Y**, Khodambashi, R, & Aukes, D. “Increasing the Life Span of Foldable Manipulators With Fabric.” Proceedings of the ASME 2020 International Design Engineering Technical Conferences and Computers and Information in Engineering Conference. Volume 10: 44th Mechanisms and Robotics Conference (MR). Virtual, Online. August 17–19, 2020. V010T10A087. ASME.

8.2.3 Talks

Conference proceedings talks:

- ”Tunable Dynamic Walking via Soft Twisted Beam Vibration”, 2023 IEEE International Conference on Soft Robotics (RoboSoft), April, 2023;
- “Compensating for Material Deformation in Foldable Robots Via Deep Learning – a Case Study”, The 2022 International Conference on Robotics and Automation (ICRA), May 2022;
- “Reconfigurable Curved Beams for Selectable Swimming Gaits in an Underwater Robot”, The 2021 International Conference on Robotics and Automation (ICRA), May 2021;
- “Shape Change Propagation Through Soft Curved Materials for Dynamically-Tuned Paddling Robots”, 2021 IEEE International Conference on Soft Robotics (RoboSoft), April 2021;
- “Reconfigurable Soft Flexure Hinges via Pinched Tubes”, 2020 IEEE RSJ International Conference on Intelligent Robots and Systems (IROS), October 2020;

Workshop presentations:

- ”Model Order Reduction for Vibrational Soft Twisted Beams Using Pseudo-rigid-body Modeling – A Case Study”, RoboSoft 2023: Workshop on Reduced-Order Modeling for Soft Robots, April 2023;
- “Modular Robots Using Soft Curved Reconfigurable Anisotropic Mechanisms”, ICRA 2022: Workshop on Modular Self-reconfigurable Robots, May 2022;

REFERENCES

[1] Ahn, S. H., K. T. Lee, H. J. Kim, R. Wu, J. S. Kim and S. H. Song, "Smart Soft Composite: An Integrated 3D Soft Morphing Structure Using Bend-twist Coupling of Anisotropic Materials", International Journal of Precision Engineering and Manufacturing **13**, 4, 631–634 (2012).

[2] Amiri Moghadam, A. A., S. Alaie, S. Deb Nath, M. Aghasizade Shaarbaf, J. K. Min, S. Dunham and B. Mosadegh, "Laser cutting as a rapid method for fabricating thin soft pneumatic actuators and robots", Soft Robotics **5**, 4, 443–451 (2018).

[3] Aoshima, S.-i., T. Tsujimura and T. Yabuta, "A Miniature Mobile Robot Using Piezo Vibration for Mobility in a Thin Tube", Journal of Dynamic Systems, Measurement, and Control **115**, 2A, 270–278, URL `https://doi.org/10.1115/1.2899031` (1993).

[4] Armon, S., E. Efrati, R. Kupferman and E. Sharon, "Geometry and mechanics in the opening of chiral seed pods", Science **333**, 6050, 1726–1730, URL `https://www.science.org/doi/abs/10.1126/science.1203874` (2011).

[5] Awad, L. N., J. Bae, K. O'Donnell, S. M. M. D. Rossi, K. Hendron, L. H. Sloot, P. Kudzia, S. Allen, K. G. Holt, T. D. Ellis and C. J. Walsh, "A soft robotic exosuit improves walking in patients after stroke", Science Translational Medicine **9**, 400, eaai9084, URL `https://www.science.org/doi/abs/10.1126/scitranslmed.aai9084` (2017).

[6] Baines, R., S. K. Patiballa, J. Booth, L. Ramirez, T. Sipple, A. Garcia, F. Fish and R. Kramer-Bottiglio, "Multi-environment robotic transitions through adaptive morphogenesis", Nature **610**, 283–289 (2022).

[7] Banerjee, J. R., "Free vibration analysis of a twisted beam using the dynamic stiffness method", International Journal of Solids and Structures **38**, 38-39, 6703–6722 (2001).

[8] Bartlett, N. W., M. T. Tolley, J. T. B. Overvelde, J. C. Weaver, B. Mosadegh, K. Bertoldi, G. M. Whitesides and R. J. Wood, "A 3d-printed, functionally graded soft robot powered by combustion", Science **349**, 6244, 161–165, URL `https://science.sciencemag.org/content/349/6244/161` (2015).

[9] Bende, N. P., A. A. Evans, S. Innes-Gold, L. A. Marin, I. Cohen, R. C. Hayward and C. D. Santangelo, "Geometrically controlled snapping transitions in shells with curved creases", Proceedings of the National Academy of Sciences of the United States of America **112**, 36, 11175–11180 (2015).

[10] Bergmann, D. C., J. R. Crew, J. M. Kramer and W. B. Wood, "Cuticle chirality and body handedness in Caenorhabditis elegans", Developmental Genetics **23**, 3, 164–174 (1998).

[11] Brown, E., N. Rodenberg, J. Amend, A. Mozeika, E. Steltz, M. R. Zakin, H. Lipson and H. M. Jaeger, "Universal robotic gripper based on the jamming of granular material", Proceedings of the National Academy of Sciences **107**, 44, 18809–18814, URL https://www.pnas.org/doi/abs/10.1073/pnas.1003250107 (2010).

[12] Calisti, M., M. Giorelli, G. Levy, B. Mazzolai, B. Hochner, C. Laschi and P. Dario, "An octopus-bioinspired solution to movement and manipulation for soft robots", Bioinspiration and Biomimetics **6**, 3 (2011).

[13] Cardou, A. and C. Jolicoeur, "Mechanical Models of Helical Strands", Applied Mechanics Reviews **50**, 1, 1–14, URL https://doi.org/10.1115/1.3101684 (1997).

[14] Carpi, F., R. Kornbluh, P. Sommer-Larsen and G. Alici, "Electroactive polymer actuators as artificial muscles: are they ready for bioinspired applications?", Bioinspiration and Biomimetics **6**, 4, 045006, URL https://dx.doi.org/10.1088/1748-3182/6/4/045006 (2011).

[15] Cheng, M. and Q. Li, "Left-Handed or Right-Handed? Determinants of the Chirality of Helically Deformable Soft Actuators", Soft Robotics **00**, 00, 1–11 (2021).

[16] Cheng, Z., W. Feng, Y. Zhang, L. Sun, Y. Liu, L. Chen and C. Wang, "A highly robust amphibious soft robot with imperceptibility based on a water-stable and self-healing ionic conductor", Advanced Materials **n/a**, n/a, 2301005, URL https://onlinelibrary.wiley.com/doi/abs/10.1002/adma.202301005 (????).

[17] Chi, Y., Y. Hong, Y. Zhao, Y. Li and J. Yin, "Snapping for high-speed and high-efficient butterfly stroke–like soft swimmer", Science Advances **8**, 46, eadd3788, URL https://www.science.org/doi/abs/10.1126/sciadv.add3788 (2022).

[18] Clark, A. B. and N. Rojas, "Assessing the performance of variable stiffness continuum structures of large diameter", IEEE Robotics and Automation Letters **4**, 3, 2455–2462 (2019).

[19] Clemente, C. J. and C. Richards, "Muscle function and hydrodynamics limit power and speed in swimming frogs", Nature Communications **4**, May (2013).

[20] Combes, S. and T. Daniel, "Flexural stiffness in insect wings ii. spatial distribution and dynamic wing bending", Journal of Experimental Biology **206**, 17, 2989–2997 (2003).

[21] Coyle, S., C. Majidi, P. LeDuc and K. J. Hsia, "Bio-inspired soft robotics: Material selection, actuation, and design", Extreme Mechanics Letters **22**, 51–59, URL https://www.sciencedirect.com/science/article/pii/S2352431617302316 (2018).

[22] Dadashi, F., A. Arami, F. Crettenand, G. P. Millet, J. Komar, L. Seifert and K. Aminian, "A hidden Markov model of the breaststroke swimming temporal phases using wearable inertial measurement units", 2013 IEEE International Conference on Body Sensor Networks, BSN 2013 pp. 1–6 (2013).

[23] Demaine, E. D., M. L. Demaine, D. Koschitz and T. Tachi, "Curved crease folding – a review on art, design and mathematics", (2011).

[24] Di Santo, V., E. L. Blevins and G. V. Lauder, "Batoid locomotion: effects of speed on pectoral fin deformation in the little skate, leucoraja erinacea", Journal of Experimental Biology **220**, 4, 705–712 (2017).

[25] Duncan, J. P. and J. L. Duncan, "Folded developables", Proceedings of the Royal Society of London. A. Mathematical and Physical Sciences **383**, 1784, 191–205 (1982).

[26] Dynamixel, "Dynamixel XM430-W350 performance graph", URL `http://emanual.robotis.com/docs/en/dxl/x/xm430-w350/#performance-graph` (2020).

[27] El-Atab, N., R. B. Mishra, F. Al-Modaf, L. Joharji, A. A. Alsharif, H. Alamoudi, M. Diaz, N. Qaiser and M. M. Hussain, "Soft actuators for soft robotic applications: A review", Advanced Intelligent Systems **2**, 10, 2000128, URL `https://onlinelibrary-wiley-com.ezproxy1.lib.asu.edu/doi/abs/10.1002/aisy.202000128` (2020).

[28] Fish, F. E., N. K. DiNenno and J. Trail, "The "dog paddle": Stereotypic swimming gait pattern in different dog breeds", Anatomical Record , January, 1–11 (2020).

[29] Fitzgerald, S. G., G. W. Delaney and D. Howard, "A review of jamming actuation in soft robotics", Actuators **9**, 4, 1–31 (2020).

[30] Flammang, B. E. and G. V. Lauder, "Caudal fin shape modulation and control during acceleration, braking and backing maneuvers in bluegill sunfish, lepomis macrochirus", Journal of Experimental Biology **212**, 2, 277–286 (2009).

[31] Ford, M. P., H. K. Lai, M. Samaee and A. Santhanakrishnan, "Hydrodynamics of metachronal paddling: Effects of varying Reynolds number and phase lag", Royal Society Open Science **6**, 10 (2019).

[32] Gadêlha, H., P. Hernández-Herrera, F. Montoya, A. Darszon and G. Corkidi, "Human sperm uses asymmetric and anisotropic flagellar controls to regulate swimming symmetry and cell steering", Science Advances **6**, 31, eaba5168, URL `https://www.science.org/doi/abs/10.1126/sciadv.aba5168` (2020).

[33] Gal, J. M. and R. W. Blake, "Biomechanics of Frog Swimming", Journal of Experimental Biology **138**, 399–411 (1988).

[34] Gandra, C. and P. Tallapragada, "Dynamics of a vibration driven bristlebot", ASME 2019 Dynamic Systems and Control Conference, DSCC 2019 **2**, August (2019).

[35] Gattas, J. M., "Miura-Base Rigid Origami : Parametrizations of Curved-Crease Geometries", **136**, December 2014, 1–10 (2016).

[36] Gelebart, A. H., D. J. Mulder, M. Varga, A. Konya, G. Vantomme, E. W. Meijer, R. L. Selinger and D. J. Broer, "Making waves in a photoactive polymer film", Nature **546**, 632–636 (2017).

[37] Gerbode, S. J., J. R. Puzey, A. G. McCormick and L. Mahadevan, "How the cucumber tendril coils and overwinds", Science **337**, 6098, 1087–1091, URL https://www.science.org/doi/abs/10.1126/science.1223304 (2012).

[38] Ghafouri, R. and R. Bruinsma, "Helicoid to spiral ribbon transition", Physical Review Letters **94**, 13, 1–4 (2005).

[39] Gittelman, S. H., "Locomotion and predatory strategy in backswimmers (hemiptera: Notonectidae)", The American Midland Naturalist **92**, 2, 496–500, URL http://www.jstor.org/stable/2424316 (1974).

[40] Goriely, A. and M. Tabor, "Spontaneous helix hand reversal and tendril perversion in climbing plants", Phys. Rev. Lett. **80**, 1564–1567, URL https://link.aps.org/doi/10.1103/PhysRevLett.80.1564 (1998).

[41] Gorissen, B., D. Melancon, N. Vasios, M. Torbati and K. Bertoldi, "Inflatable soft jumper inspired by shell snapping", Science Robotics **5**, 42, eabb1967, URL https://www.science.org/doi/abs/10.1126/scirobotics.abb1967 (2020).

[42] Gorissen, B., D. Reynaerts, S. Konishi, K. Yoshida, J. W. Kim and M. De Volder, "Elastic Inflatable Actuators for Soft Robotic Applications", Advanced Materials **29**, 43, 1–14 (2017).

[43] Heung, K. H., R. K. Tong, A. T. Lau and Z. Li, "Robotic glove with soft-elastic composite actuators for assisting activities of daily living", Soft Robotics **6**, 2, 289–304, URL https://doi.org/10.1089/soro.2017.0125, pMID: 30874489 (2019).

[44] Hodges, D. H., "A mixed variational formulation based on exact intrinsic equations for dynamics of moving beams", International Journal of Solids and Structures **26**, 11, 1253–1273, URL http://dx.doi.org/10.1016/0020-7683(90)90060-9 (1990).

[45] Hodges, D. H., "Geometrically Exact, Intrinsic Theory for Dynamics of Curved and Twisted Anisotropic Beams", AIAA Journal **47**, 5, 1308–1309 (2009).

[46] Holmér, I., "Propulsive efficiency of breaststroke and freestyle swimming", European Journal of Applied Physiology and Occupational Physiology **33**, 2, 95–103 (1974).

[47] Howell, L. L. and A. Midha, "Parametric deflection approximations for end-loaded, large-deflection beams in compliant mechanisms", Proceedings of the ASME Design Engineering Technical Conference **Part F168016-3**, March 1995, 157–166 (1992).

[48] Howell, L. L., A. Midha and T. W. Norton, "Evaluation of equivalent spring stiffness for use in a pseudo-rigid-body model of large-deflection compliant mechanisms", Journal of Mechanical Design, Transactions of the ASME **118**, 1, 126–131 (1996).

[49] Huffman, D. A., "Curvature and Creases: A Primer on Paper", IEEE Transactions on Computers **C-25**, 10, 1010–1019 (1976).

[50] Ilievski, F., A. D. Mazzeo, R. F. Shepherd, X. Chen and G. M. Whitesides, "Soft robotics for chemists", Angewandte Chemie International Edition **50**, 8, 1890–1895, URL https://onlinelibrary.wiley.com/doi/abs/10.1002/anie.201006464 (2011).

[51] ITO, S. and A. AZUMA, "Analysis of thrust performance for paddling locomotion", Theoretical and Applied Mechanics **50**, 271–280 (2001).

[52] Jiang, M., Q. Yu and N. Gravish, "Vacuum induced tube pinching enables reconfigurable flexure joints with controllable bend axis and stiffness", in "2021 IEEE 4th International Conference on Soft Robotics (RoboSoft)", pp. 315–320 (2021).

[53] Jiang, Y., M. Sharifzadeh and D. M. Aukes, "Reconfigurable soft flexure hinges via pinched tubes", in "2020 IEEE/RSJ International Conference on Intelligent Robots and Systems (IROS)", pp. 8843–8850 (2020).

[54] Jiang, Y., M. Sharifzadeh and D. M. Aukes, "Reconfigurable soft flexure hinges via pinched tubes (accepted)", IEEE International Conference on Intelligent Robots and Systems URL https://idealab.asu.edu/assets/jiang-iros-2020.pdf (2020).

[55] Jiang, Y., M. Sharifzadeh and D. M. Aukes, "Shape change propagation through soft curved materials for dynamically-tuned paddling robots", in "2021 IEEE 4th International Conference on Soft Robotics (RoboSoft)", pp. 230–237 (2021).

[56] Jizhuang, F., D. Qilong, Y. Qingguo, W. Yi, Q. Jiaming and Z. Yanhe, "Biologically inspired swimming robotic frog based on pneumatic soft actuators", Bioinspiration and Biomimetics **15**, 4 (2020).

[57] Jizhuang, F., Z. Wei, Y. Bowen and L. Gangfeng, "Propulsive efficiency of frog swimming with different feet and swimming patterns", Biology Open **6**, 4, 503–510 (2017).

[58] Katzschmann, R. K., J. DelPreto, R. MacCurdy and D. Rus, "Exploration of underwater life with an acoustically controlled soft robotic fish", Science Robotics **3**, 16, eaar3449, URL https://www.science.org/doi/abs/10.1126/scirobotics.aar3449 (2018).

[59] Kergosien, Y. L., H. Gotoda and T. L. Kunii, "Bending and Creasing Virtual Paper", IEEE Computer Graphics and Applications **14**, 1, 40–48 (1994).

[60] Kiendl, J., M.-C. Hsu, M. C. Wu and A. Reali, "Isogeometric kirchhoff–love shell formulations for general hyperelastic materials", Computer Methods in Applied Mechanics and Engineering **291**, 280 – 303, URL http://www.sciencedirect.com/science/article/pii/S0045782515001127 (2015).

[61] Kim, D., Z. Hao, A. R. Mohazab and A. Ansari, "On the forward and backward motion of milli-bristlebots", International Journal of Non-Linear Mechanics **127**, June, 103551, URL https://doi.org/10.1016/j.ijnonlinmec.2020.103551 (2020).

[62] Kim, H. I., M. W. Han, S. H. Song and S. H. Ahn, "Soft morphing hand driven by SMA tendon wire", Composites Part B: Engineering **105**, 138–148, URL http://dx.doi.org/10.1016/j.compositesb.2016.09.004 (2016).

[63] Kim, H.-J., S.-H. Song and S.-H. Ahn, "A turtle-like swimming robot using a smart soft composite (SSC) structure", Smart Materials and Structures **22**, 1, 014007, URL https://doi.org/10.1088%2F0964-1726%2F22%2F1%2F014007 (2012).

[64] Kovařík, H. and A. Sacchetti, "Resonances in twisted quantum waveguides", Journal of Physics A: Mathematical and Theoretical **40**, 29, 8371–8384, URL https://doi.org/10.1088/1751-8113/40/29/012 (2007).

[65] Laschi, C., M. Cianchetti, B. Mazzolai, L. Margheri, M. Follador and P. Dario, "Soft robot arm inspired by the octopus", Advanced Robotics **26**, 7, 709–727 (2012).

[66] Li, Y., F. Fish, Y. Chen, T. Ren and J. Zhou, "Bio-inspired robotic dog paddling: Kinematic and hydro-dynamic analysis", Bioinspiration and Biomimetics **14**, 6 (2019).

[67] Li, Y., T. Ren, Y. Chen, J. Zhou, Y. Hu, Z. Wang, W. Sun and C. Xiong, "Untethered multimode fluidic actuation: A new approach to soft and compliant robotics", Soft Robotics **8**, 1, 71–84 (2021).

[68] Lilley, D. M. J., "Understanding dna: The molecule and how it works", Trends in Genetics **9**, 185 (1993).

[69] Lin, H.-T., G. G. Leisk and B. Trimmer, "Goqbot: a caterpillar-inspired soft-bodied rolling robot", Bioinspiration and Biomimetics **6**, 2, 026007, URL https://dx.doi.org/10.1088/1748-3182/6/2/026007 (2011).

[70] Luo, M., W. Tao, F. Chen, T. K. Khuu, S. Ozel and C. D. Onal, "Design improvements and dynamic characterization on fluidic elastomer actuators for a soft robotic snake", IEEE Conference on Technologies for Practical Robot Applications, TePRA pp. 1–6 (2014).

[71] López, C. and J. Serna, "Quantitative analysis of kayak paddling technique: Definition of an optimal stroke profile", Revista Andaluza de Medicina del Deporte **4**, 91–95 (2011).

[72] Manti, M., V. Cacucciolo and M. Cianchetti, "Stiffening in soft robotics: A review of the state of the art", IEEE Robotics and Automation Magazine **23**, 3, 93–106 (2016).

[73] Margheri, L., B. Mazzolai, M. Cianchetti, P. Dario and C. Laschi, "Tools and methods for experimental in-vivo measurement and biomechanical characterization of an Octopus vulgaris arm", Proceedings of the 31st Annual International Conference of the IEEE Engineering in Medicine and Biology Society: Engineering the Future of Biomedicine, EMBC 2009 pp. 7196–7199 (2009).

[74] Markin, V. S., A. G. Volkov and E. Jovanov, "Active movements in plants: mechanism of trap closure by dionaea muscipula ellis", Plant signaling & behavior **3**, 10, 778–783 (2008).

[75] Marvi, H. and D. L. Hu, "Friction enhancement in concertina locomotion of snakes", Journal of the Royal Society Interface **9**, 76, 3067–3080 (2012).

[76] Mazaheri, K. and A. Ebrahimi, "Experimental investigation of the effect of chordwise flexibility on the aerodynamics of flapping wings in hovering flight", Journal of Fluids and Structures **26**, 4, 544–558 (2010).

[77] Mazzolai, B., L. Margheri, M. Cianchetti, P. Dario and C. Laschi, "Soft-robotic arm inspired by the octopus: Ii. from artificial requirements to innovative technological solutions", Bioinspiration and Biomimetics **7**, 2, 025005, URL `https://dx.doi.org/10.1088/1748-3182/7/2/025005` (2012).

[78] Miyashita, S., I. DiDio, I. Ananthabhotla, B. An, C. Sung, S. Arabagi and D. Rus, "Folding angle regulation by curved crease design for self-assembling origami propellers", Journal of Mechanisms and Robotics **7**, 2, 1–8 (2015).

[79] Miyashita, S., S. Guitron, M. Ludersdorfer, C. R. Sung and D. Rus, "An untethered miniature origami robot that self-folds, walks, swims, and degrades", Proceedings - IEEE International Conference on Robotics and Automation **2015-June**, June, 1490–1496 (2015).

[80] Mosadegh, B., P. Polygerinos, C. Keplinger, S. Wennstedt, R. F. Shepherd, U. Gupta, J. Shim, K. Bertoldi, C. J. Walsh and G. M. Whitesides, "Pneumatic networks for soft robotics that actuate rapidly", Advanced Functional Materials **24**, 15, 2163–2170 (2014).

[81] Mustapha, K. and Z. Zhong, "Wave propagation characteristics of a twisted micro scale beam", International Journal of Engineering Science **53**, 46–57, URL `https://www.sciencedirect.com/science/article/pii/S002072251100259X` (2012).

[82] Nasab, A. M., A. Sabzehzar, M. Tatari, C. Majidi and W. Shan, "A Soft Gripper with Rigidity Tunable Elastomer Strips as Ligaments", Soft Robotics **4**, 4, 411–420 (2017).

[83] Neppalli, S., B. Jones, W. McMahan, V. Chitrakaran, I. Walker, M. Pritts, M. Csencsits, C. Rahn and M. Grissom, "OctArm - A soft robotic manipulator", IEEE International Conference on Intelligent Robots and Systems p. 2569 (2007).

[84] Nguyen, K., N. Yu, M. M. Bandi, M. Venkadesan and S. Mandre, "Curvature-induced stiffening of a fish fin", Journal of the Royal Society Interface **14**, 130 (2017).

[85] Nguyen, K., N. Yu, M. M. Bandi, M. Venkadesan and S. Mandre, "Curvature-induced stiffening of a fish fin", Journal of The Royal Society Interface **14**, 130, 20170247 (2017).

[86] Onal, C. D. and D. Rus, "Autonomous undulatory serpentine locomotion utilizing body dynamics of a fluidic soft robot", Bioinspiration and Biomimetics **8**, 2 (2013).

[87] Pan, Q. and S. Guo, "A paddling type of microrobot in pipe", Proceedings - IEEE International Conference on Robotics and Automation pp. 2995–3000 (2009).

[88] Park, H., S. Park, E. Yoon, B. Kim, J. Park and S. Park, "Paddling based microrobot for capsule endoscopes", Proceedings - IEEE International Conference on Robotics and Automation , April, 3377–3382 (2007).

[89] Patel, D. K., X. Huang, Y. Luo, M. Mungekar, M. K. Jawed, L. Yao and C. Majidi, "Highly dynamic bistable soft actuator for reconfigurable multimodal soft robots", Advanced Materials Technologies **8**, 2, 2201259, URL https://onlinelibrary.wiley.com/doi/abs/10.1002/admt.202201259 (2023).

[90] Peele, B. N., T. J. Wallin, H. Zhao and R. F. Shepherd, "3D printing antagonistic systems of artificial muscle using projection stereolithography", Bioinspiration and Biomimetics **10**, 5, 55003, URL http://dx.doi.org/10.1088/1748-3190/10/5/055003 (2015).

[91] Pini, V., J. J. Ruz, P. M. Kosaka, O. Malvar, M. Calleja and J. Tamayo, "How two-dimensional bending can extraordinarily stiffen thin sheets", Scientific Reports **6**, July, 1–6, URL http://dx.doi.org/10.1038/srep29627 (2016).

[92] Polygerinos, P., N. Correll, S. A. Morin, B. Mosadegh, C. D. Onal, K. Petersen, M. Cianchetti, M. T. Tolley and R. F. Shepherd, "Soft robotics: Review of fluid-driven intrinsically soft devices; manufacturing, sensing, control, and applications in human-robot interaction", (2017).

[93] Polygerinos, P., Z. Wang, K. C. Galloway, R. J. Wood and C. J. Walsh, "Soft robotic glove for combined assistance and at-home rehabilitation", Robotics and Autonomous Systems **73**, 135–143, URL https://www.sciencedirect.com/science/article/pii/S0921889014001729, wearable Robotics (2015).

[94] Pu, H., Y. Sun, Y. Yang, S. Ma and Z. Gong, "Modeling of the oscillating-paddling gait for an ePaddle locomotion mechanism", Proceedings - IEEE International Conference on Robotics and Automation pp. 3429–3435 (2013).

[95] Qaiser, Z. and S. Johnson, "Generalized spiral spring: A bioinspired tunable stiffness mechanism for linear response with high resolution", Journal of Mechanisms and Robotics **13**, 1 (2021).

[96] R, C. and M. A, "Elephant trunk type elastic manipulator - a tool for bulk and liquid materials transportation", Robotica **17**, 1, 11–16 (1999).

[97] Renda, F., M. Giorelli, M. Calisti, M. Cianchetti and C. Laschi, "Dynamic model of a multibending soft robot arm driven by cables", IEEE Transactions on Robotics **30**, 5, 1109–1122 (2014).

[98] Ristroph, L., A. J. Bergou, J. Guckenheimer, Z. J. Wang and I. Cohen, "Paddling mode of forward flight in insects", Physical Review Letters **106**, 17, 1–4 (2011).

[99] Roberts, J. W., R. Cory and R. Tedrake, "On the controllability of fixed-wing perching", in "Proceedings of the American Control Conference", No. 1, pp. 2018–2023 (IEEE, 2009), URL `http://ieeexplore.ieee.org/document/5160526/`.

[100] Rosen, A., "Structural and Dynamic Behavior of Pretwisted Rods and Beams", Applied Mechanics Reviews **44**, 12, 483–515, URL `https://doi.org/10.1115/1.3119490` (1991).

[101] Rus, D. and M. T. Tolley, "Design, fabrication and control of soft robots", Nature **521**, 7553, 467–475 (2015).

[102] Saito, K., S. Nomura, S. Yamamoto, R. Niiyama and Y. Okabe, "Investigation of hindwing folding in ladybird beetles by artificial elytron transplantation and microcomputed tomography", Proceedings of the National Academy of Sciences **114**, 22, 5624–5628 (2017).

[103] Schilthuizen, M. and A. Davison, "The convoluted evolution of snail chirality", Naturwissenschaften **92**, 11, 504–515 (2005).

[104] Selinger, R. L. B., J. V. Selinger, A. P. Malanoski and J. M. Schnur, "Shape selection in chiral self-assembly", Phys. Rev. Lett. **93**, 158103, URL `https://link.aps.org/doi/10.1103/PhysRevLett.93.158103` (2004).

[105] Sharifzadeh, M. and D. Aukes, "Curvature-induced buckling for flapping-wing vehicles", IEEE/ASME Transactions on Mechatronics pp. 1–1 (2020).

[106] Sharifzadeh, M. and D. M. Aukes, "Curvature-induced buckling for flapping-wing vehicles", IEEE/ASME Transactions on Mechatronics **26**, 1, 503–514 (2021).

[107] Sharifzadeh, M., Y. Jiang and D. M. Aukes, "Reconfigurable curved beams for selectable swimming gaits in an underwater robot", IEEE Robotics and Automation Letters **6**, 2, 3437–3444 (2021).

[108] Shepherd, R. F., F. Ilievski, W. Choi, S. A. Morin, A. A. Stokes, A. D. Mazzeo, X. Chen, M. Wang and G. M. Whitesides, "Multigait soft robot", Proceedings of the National Academy of Sciences of the United States of America **108**, 51, 20400–20403 (2011).

[109] Shin, Y. J., H. J. Lee, K.-S. Kim and S. Kim, "A robot finger design using a dual-mode twisting mechanism to achieve high-speed motion and large grasping force", IEEE Transactions on Robotics **28**, 6, 1398–1405 (2012).

[110] Shiva, A., A. Stilli, Y. Noh, A. Faragasso, I. D. Falco, G. Gerboni, M. Cianchetti, A. Menciassi, K. Althoefer and H. A. Wurdemann, "Tendon-Based Stiffening for a Pneumatically Actuated Soft Manipulator", IEEE Robotics and Automation Letters **1**, 2, 632–637 (2016).

[111] Storn, R. and K. Price, "Differential Evolution – A Simple and Efficient Heuristic for global Optimization over Continuous Spaces", Journal of Global Optimization **11**, 4, 341–359, URL `https://doi.org/10.1023/A:1008202821328` (1997).

[112] Sugiyama, Y. and S. Hirai, "Crawling and jumping by a deformable robot", International Journal of Robotics Research **25**, 5-6, 603–620 (2006).

[113] Sumbre, G., G. Fiorito, T. Flash and B. Hochner, "Octopuses Use a Human-like Strategy to Control Precise Point-to-Point Arm Movements", Current Biology **16**, 8, 767–772 (2006).

[114] Sun, J., B. Tighe and J. Zhao, "Tuning the energy landscape of soft robots for fast and strong motion", in "2020 IEEE International Conference on Robotics and Automation (ICRA)", pp. 10082–10088 (2020).

[115] Sun, Y., S. Ma, K. Fujita, Y. Yang and H. Pu, "Modeling the rotational paddling of an ePaddle-based amphibious robot", IEEE International Conference on Intelligent Robots and Systems pp. 610–615 (2012).

[116] Sun, Y., H. K. Yap, X. Liang, J. Guo, P. Qi, M. H. Ang and C. H. Yeow, "Stiffness Customization and Patterning for Property Modulation of Silicone-Based Soft Pneumatic Actuators", Soft Robotics **4**, 3, 251–260 (2017).

[117] Tachi, T. and G. Epps, "Designing One-DOF Mechanisms for Architecture by Rationalizing Curved Folding", Proceedings of the International Symposium on Algorithmic Design for Architecture and Urban Design , October (2011).

[118] Takagi, H., S. Sugimoto, N. Nishijima and B. Wilson, "Swimming: Differences in stroke phases, arm-leg coordination and velocity fluctuation due to event, gender and performance level in breaststroke", Sports Biomechanics **3**, 1, 15–27 (2004).

[119] Tang, Y., Y. Chi, J. Sun, T.-H. Huang, O. H. Maghsoudi, A. Spence, J. Zhao, H. Su and J. Yin, "Leveraging elastic instabilities for amplified performance: Spine-inspired high-speed and high-force soft robots", Science Advances **6**, 19, eaaz6912, URL `https://www.science.org/doi/abs/10.1126/sciadv.aaz6912` (2020).

[120] Tasora, A., R. Serban, H. Mazhar, A. Pazouki, D. Melanz, J. Fleischmann, M. Taylor, H. Sugiyama and D. Negrut, "Chrono: An Open Source Multi-physics Dynamics Engine", in "High Performance Computing in Science and Engineering", edited by T. Kozubek, R. Blaheta, J. Šístek, M. Rozložník and M. Čermák, pp. 19–49 (Springer International Publishing, Cham, 2016).

[121] Tawk, C., M. In Het Panhuis, G. M. Spinks and G. Alici, "Bioinspired 3d printable soft vacuum actuators for locomotion robots, grippers and artificial muscles", Soft Robotics **5**, 6, 685–694 (2018).

[122] Terryn, S., J. Brancart, D. Lefeber, G. V. Assche and B. Vanderborght, "Self-healing soft pneumatic robots", Science Robotics **2**, 9, eaan4268, URL https://www.science.org/doi/abs/10.1126/scirobotics.aan4268 (2017).

[123] Thompson, K. G., D. P. MacLaren, A. Lees and G. Atkinson, "The effects of changing pace on metabolism and stroke characteristics during high-speed breaststroke swimming", Journal of Sports Sciences **22**, 2, 149–157 (2004).

[124] Todorov, E., T. Erez and Y. Tassa, "Mujoco: A physics engine for model-based control", in "2012 IEEE/RSJ International Conference on Intelligent Robots and Systems", pp. 5026–5033 (2012).

[125] Tolley, M. T., R. F. Shepherd, B. Mosadegh, K. C. Galloway, M. Wehner, M. Karpelson, R. J. Wood and G. M. Whitesides, "A Resilient, Untethered Soft Robot", Soft Robotics **1**, 3, 213–223 (2014).

[126] Torsi, L., G. M. Farinola, F. Marinelli, M. C. Tanese, O. H. Omar, L. Valli, F. Babudri, F. Palmisano, P. G. Zambonin and F. Naso, "A sensitivity-enhanced field-effect chiralsensor", Nature Materials **7**, 5, 412–417 (2008).

[127] UltiMaker, "Technical data sheet: TPU 95A", URL https://ultimaker.com/download/74976/UM180821%20TDS%20TPU%2095A%20RB%20V11.pdf, version 4.002 (2018).

[128] van der Walt, S., J. L. Schönberger, J. Nunez-Iglesias, F. Boulogne, J. D. Warner, N. Yager, E. Gouillart, T. Yu and the scikit-image contributors, "scikit-image: image processing in python", PeerJ **2**, e453, URL https://doi.org/10.7717/peerj.453 (2014).

[129] Vogel, R. and H. Stark, "Motor-driven bacterial flagella and buckling instabilities", The European Physical Journal E **35**, 2, 15 (2012).

[130] Volkov, A. G., T. Adesina, V. S. Markin and E. Jovanov, "Kinetics and mechanism of dionaea muscipula trap closing", Plant physiology **146**, 2, 694–702 (2008).

[131] Walker, J., T. Zidek, C. Harbel, S. Yoon, F. S. Strickland, S. Kumar and M. Shin, "Soft robotics: A review of recent developments of pneumatic soft actuators", Actuators **9**, 1, URL https://www.mdpi.com/2076-0825/9/1/3 (2020).

[132] Wang, M., B. P. Lin and H. Yang, "A plant tendril mimic soft actuator with phototunable bending and chiral twisting motion modes", Nature Communications **7**, 1–8, URL http://dx.doi.org/10.1038/ncomms13981 (2016).

[133] Watson, J. D. and F. H. Crick, "Molecular structure of nucleic acids: A structure for deoxyribose nucleic acid", (1974).

[134] Webster, R. J. and B. A. Jones, "Design and kinematic modeling of constant curvature continuum robots: A review", International Journal of Robotics Research **29**, 13, 1661–1683 (2010).

[135] Wei, Y., Y. Chen, T. Ren, Q. Chen, C. Yan, Y. Yang and Y. Li, "A Novel, Variable Stiffness Robotic Gripper Based on Integrated Soft Actuating and Particle Jamming", Soft Robotics **3**, 3, 134–143 (2016).

[136] Whitney, J. P., *Design and performance of insect-scale flapping-wing vehicles*, Ph.D. thesis (2012).

[137] Wu, J., Y. Zhao, Y. Zhang, D. Shumate, S. B. Slade, S. V. Franklin and D. L. Hu, "Elephant trunks form joints to squeeze together small objects", Journal of the Royal Society Interface **15**, 147 (2018).

[138] Yang, Y., K. Vella and D. P. Holmes, "Grasping with kirigami shells", Science Robotics **6**, 54 (2021).

[139] Yap, H. K., H. Y. Ng and C. H. Yeow, "High-Force Soft Printable Pneumatics for Soft Robotic Applications", Soft Robotics **3**, 3, 144–158 (2016).

[140] Zhai, Z., Y. Wang, K. Lin, L. Wu and H. Jiang, "In situ stiffness manipulation using elegant curved origami", Science Advances **6**, 47, 1–10 (2020).

[141] Zhang, Y., W. Zhang, J. Yang and W. Pu, "Bioinspired soft robotic fingers with sequential motion based on tendon-driven mechanisms", Soft Robotics **9**, 3, 531–541, URL `https://doi.org/10.1089/soro.2021.0009`, pMID: 34115957 (2022).

[142] Zheng, B., Y. Liu, J. Liu, S. Yin and J. Xu, "Novel mechanical behaviors of DNA-inspired helical structures with chirality", International Journal of Mechanical Sciences **161-162**, May (2019).

[143] Zhu, M., Y. Mori, T. Wakayama, A. Wada and S. Kawamura, "A Fully Multi-Material Three-Dimensional Printed Soft Gripper with Variable Stiffness for Robust Grasping", Soft Robotics **6**, 4, 507–519 (2019).

APPENDIX A

RAW DATA FROM SINGLE BEAM FREQUENCY SWEEP TEST

Here we show the detailed data from single beam frequency sweep test. Fig. A.1 shows the results using beam with $\phi = -90^\circ$ while Fig. A.2 shows results using beam with $\phi = 90^\circ$.

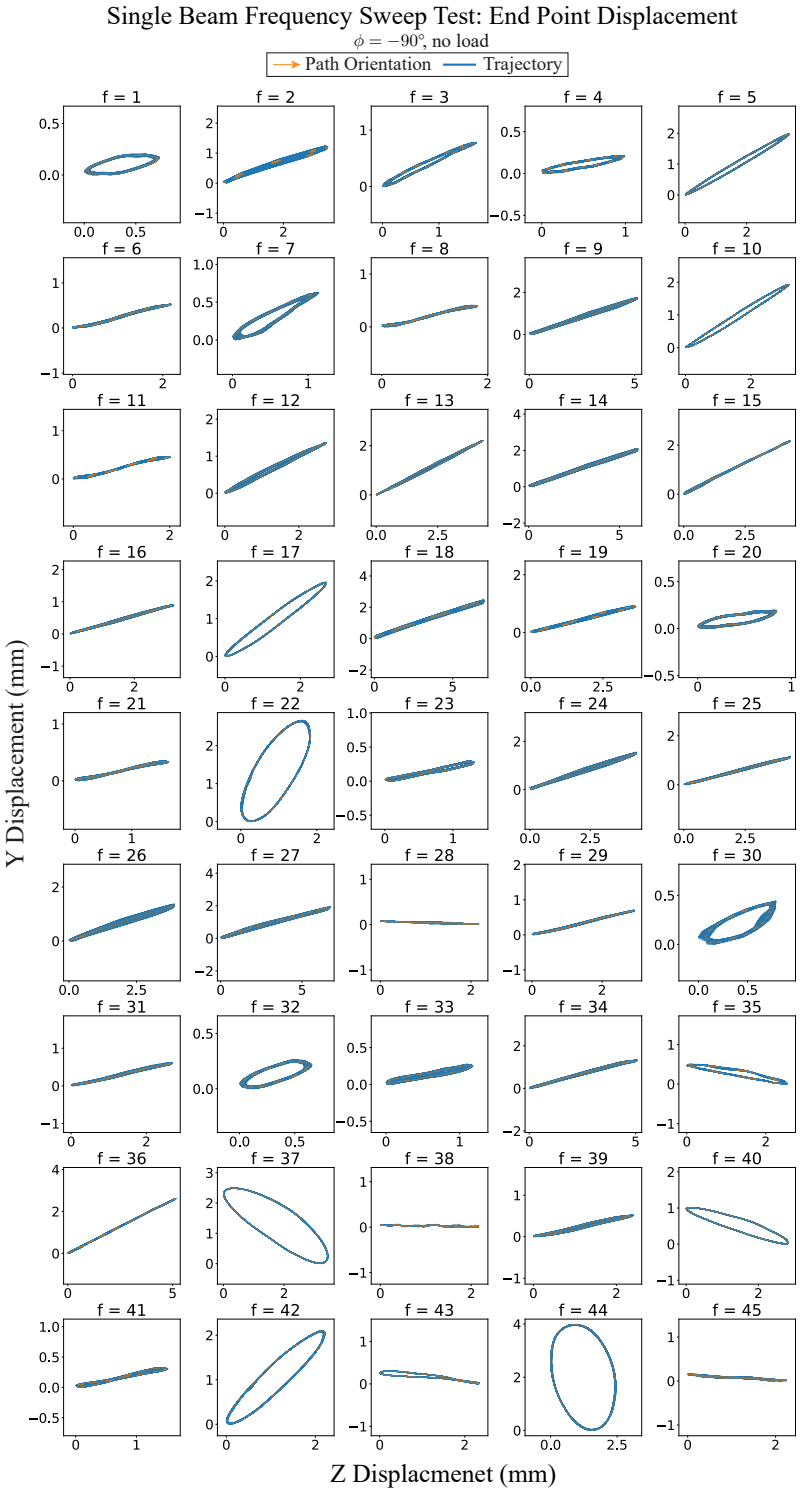

Figure A.1: Single Beam Frequency Sweep Test: $\phi = -90°$, No Load

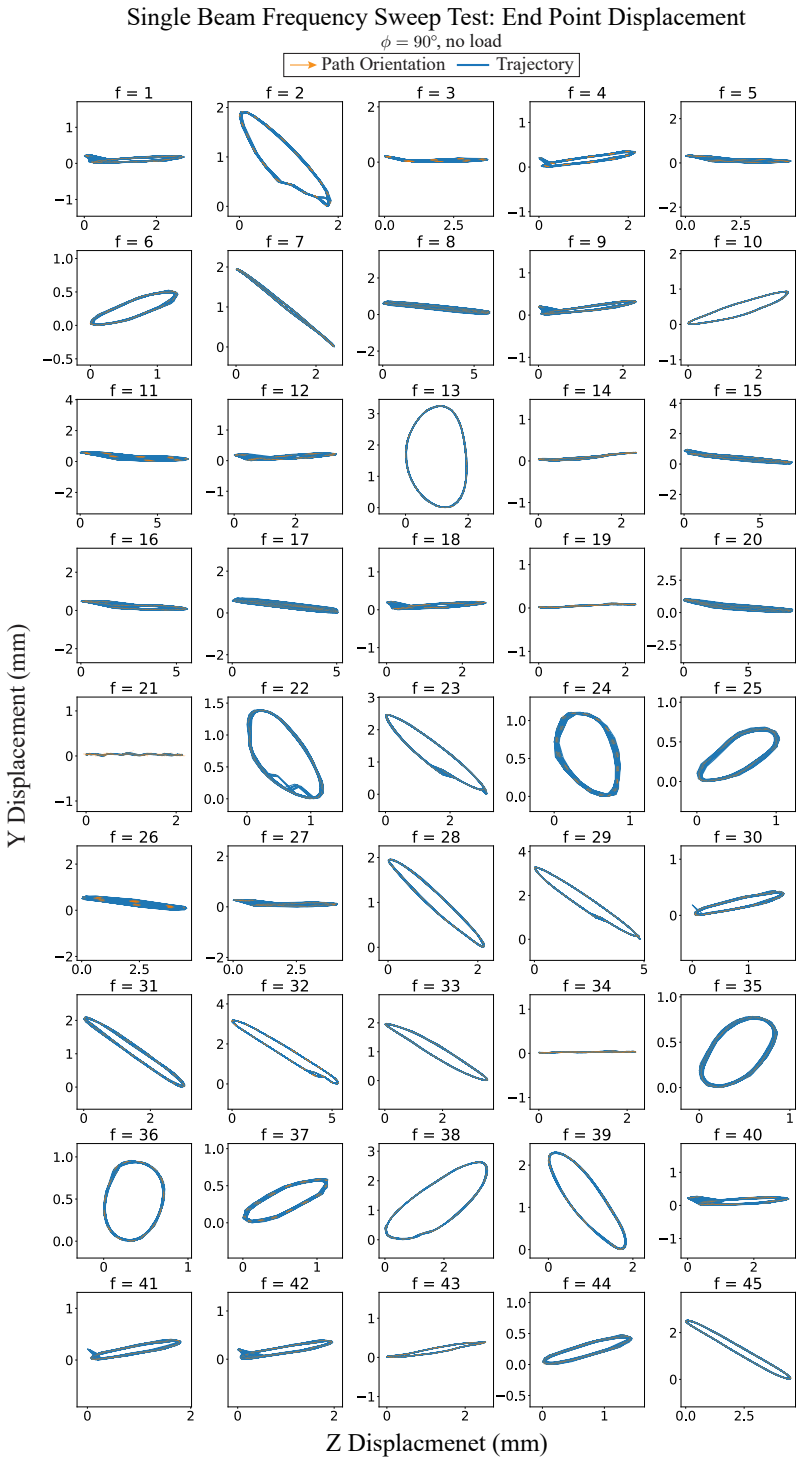

Figure A.2: Single Beam Frequency Sweep Test: $\phi = 90°$, No Load

APPENDIX B

RAW DATA FROM SINGLE BEAM OFFSET LOAD TEST

Here we show the detailed data from single beam offset load test. Figure B.1, B.2, B.3, and B.4 shows results using beam with $\phi = -90^\circ$ and offset load at lower-left, lower-right, upper-left, and upper-right, respectively. Figure B.5, B.6, B.7, and B.8 shows results using beam with $\phi = 90^\circ$ and offset load at lower-left, lower-right, upper-left, and upper-right, respectively.

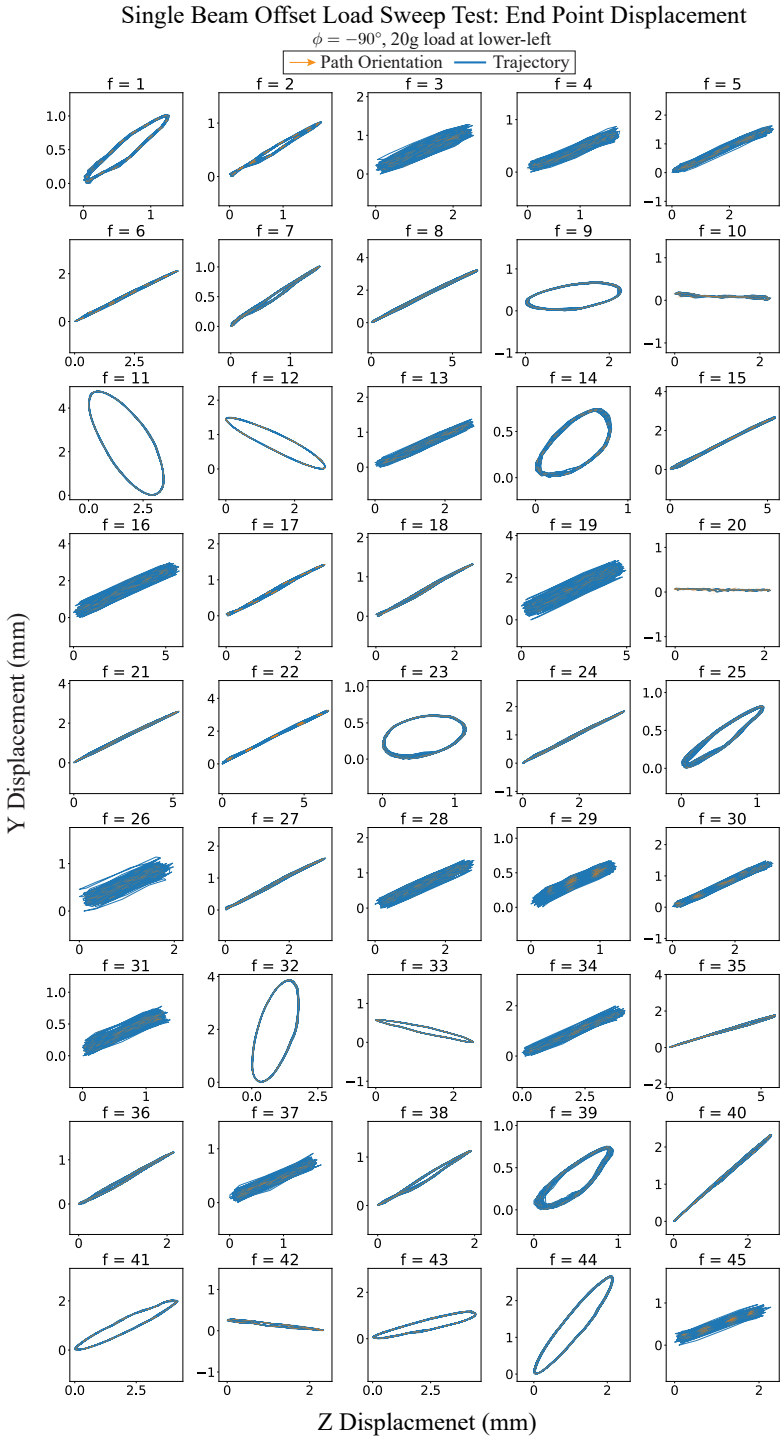

Figure B.1: Single Beam Offset Load Frequency Sweep Test: $\phi = -90°$, Load at Lower-left

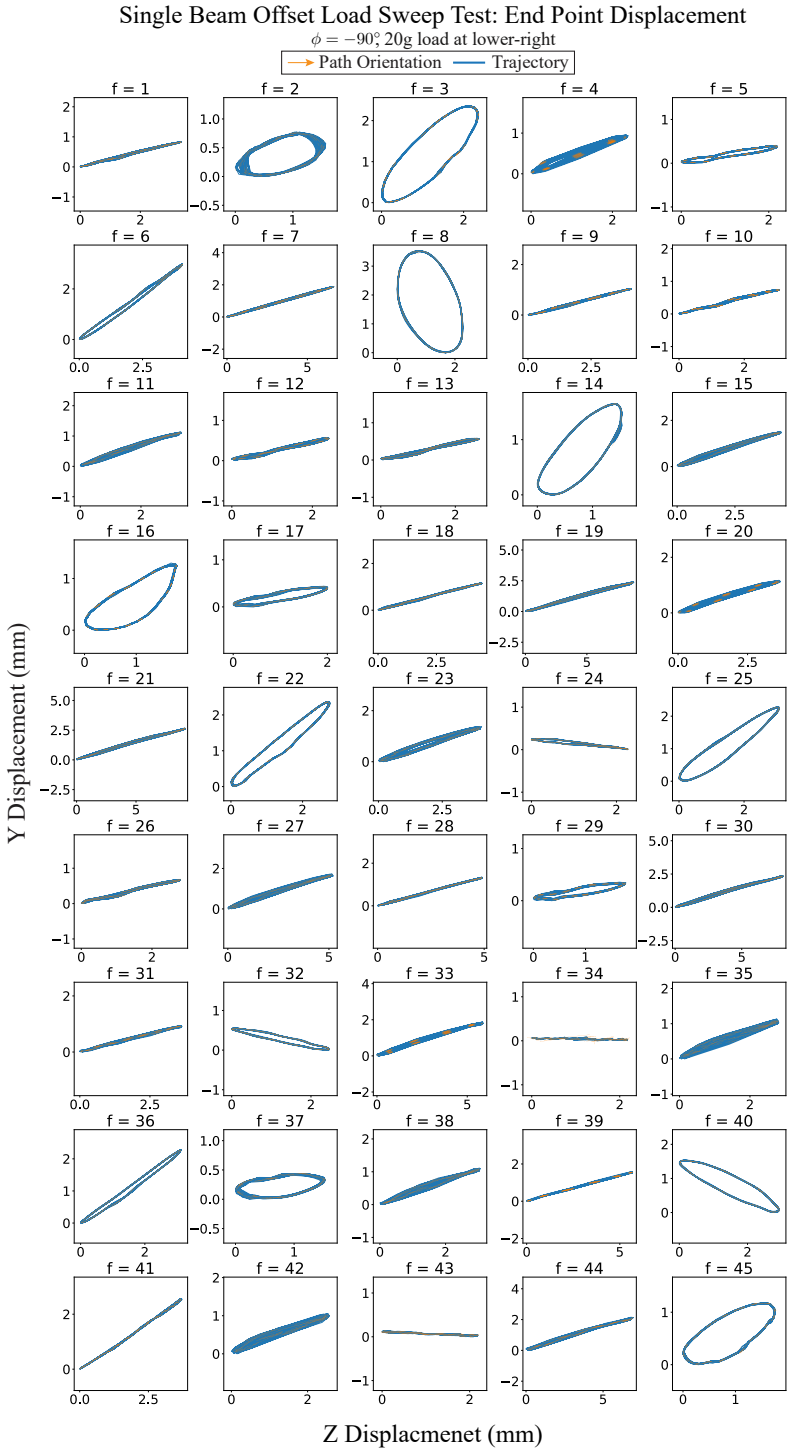

Figure B.2: Single Beam Offset Load Frequency Sweep Test: $\phi = -90^{\circ}$, Load at Lower-right

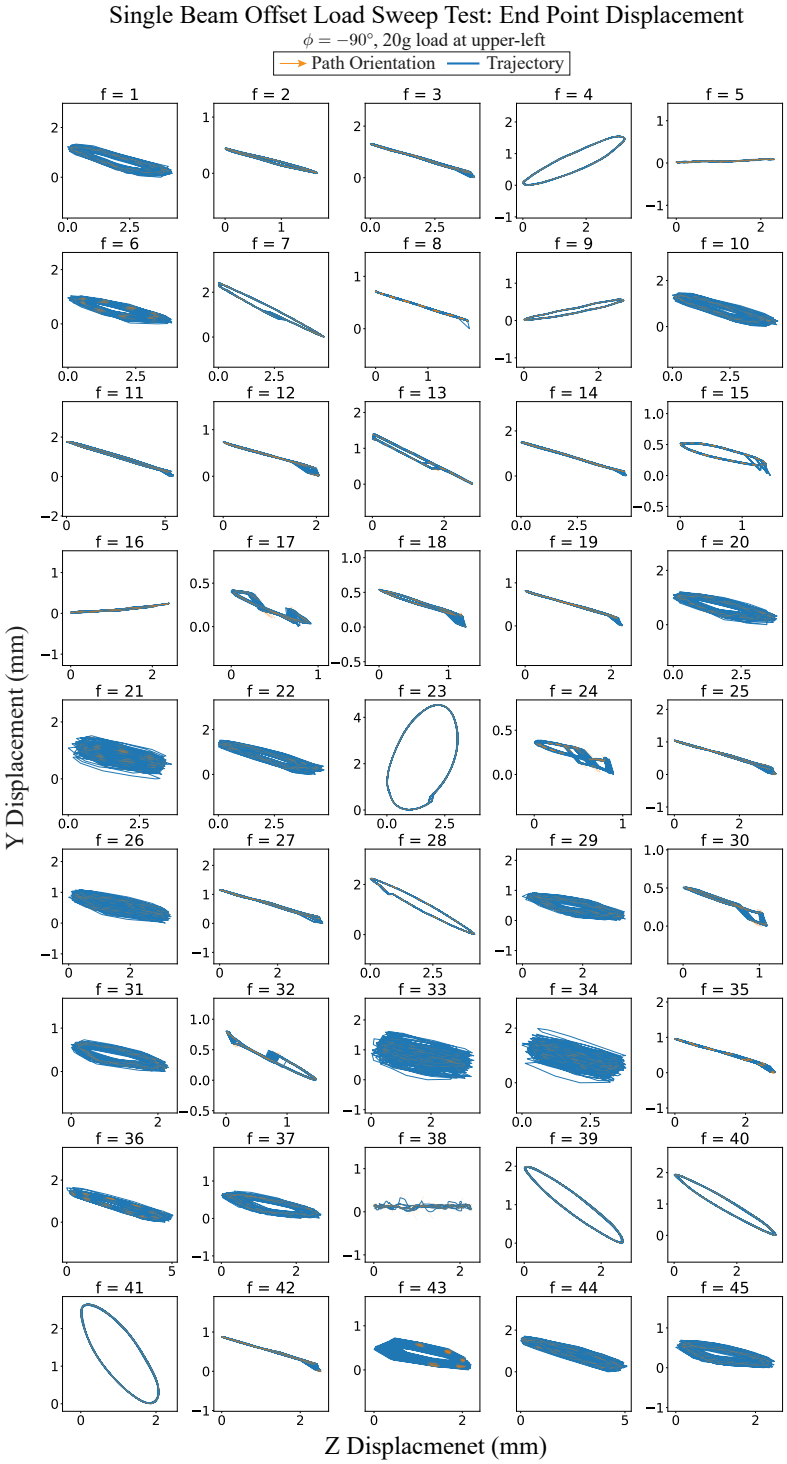

Figure B.3: Single Beam Offset Load Frequency Sweep Test: $\phi = -90°$, Load at Upper-left

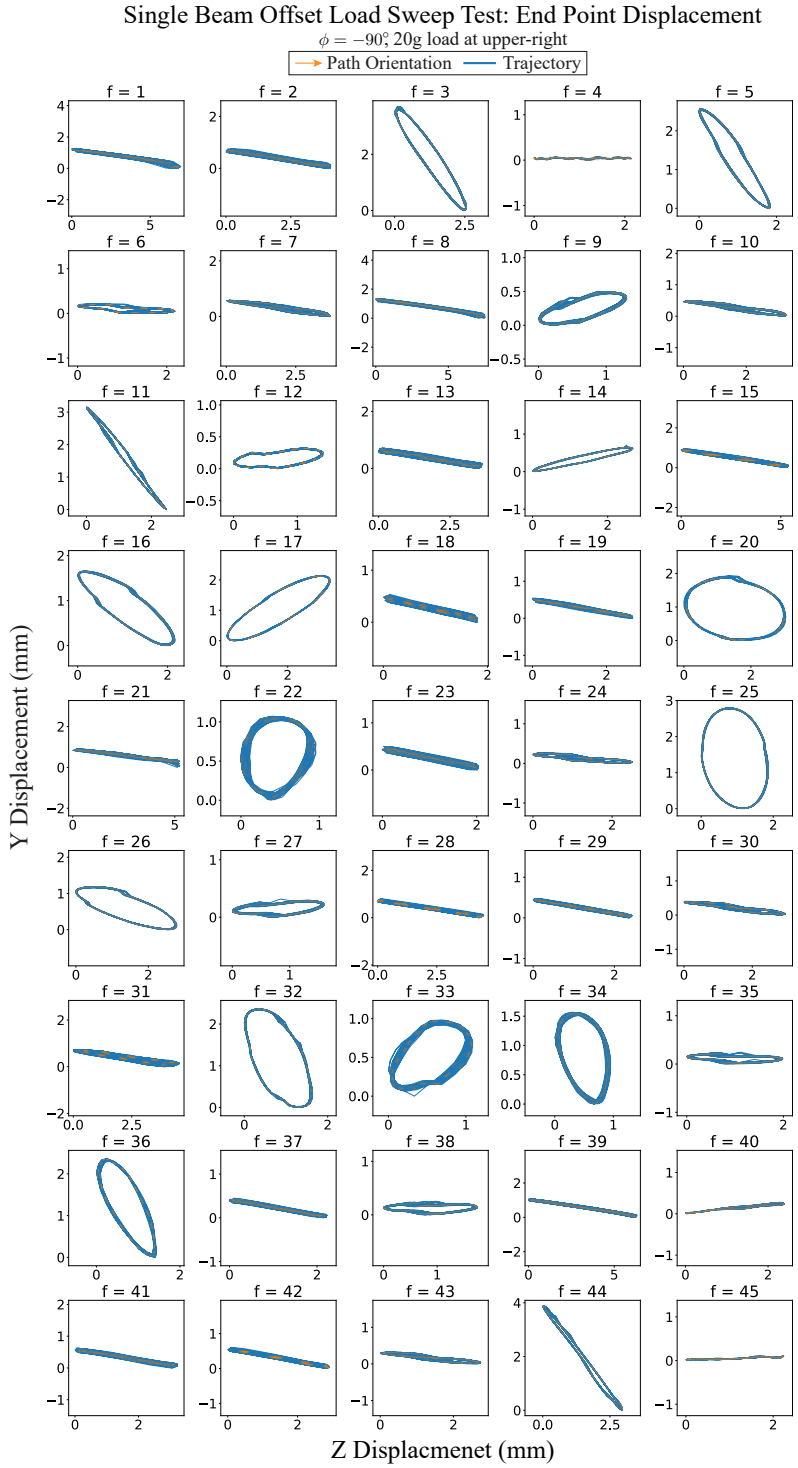

Figure B.4: Single Beam Offset Load Frequency Sweep Test: $\phi = -90°$, Load at Upper-right

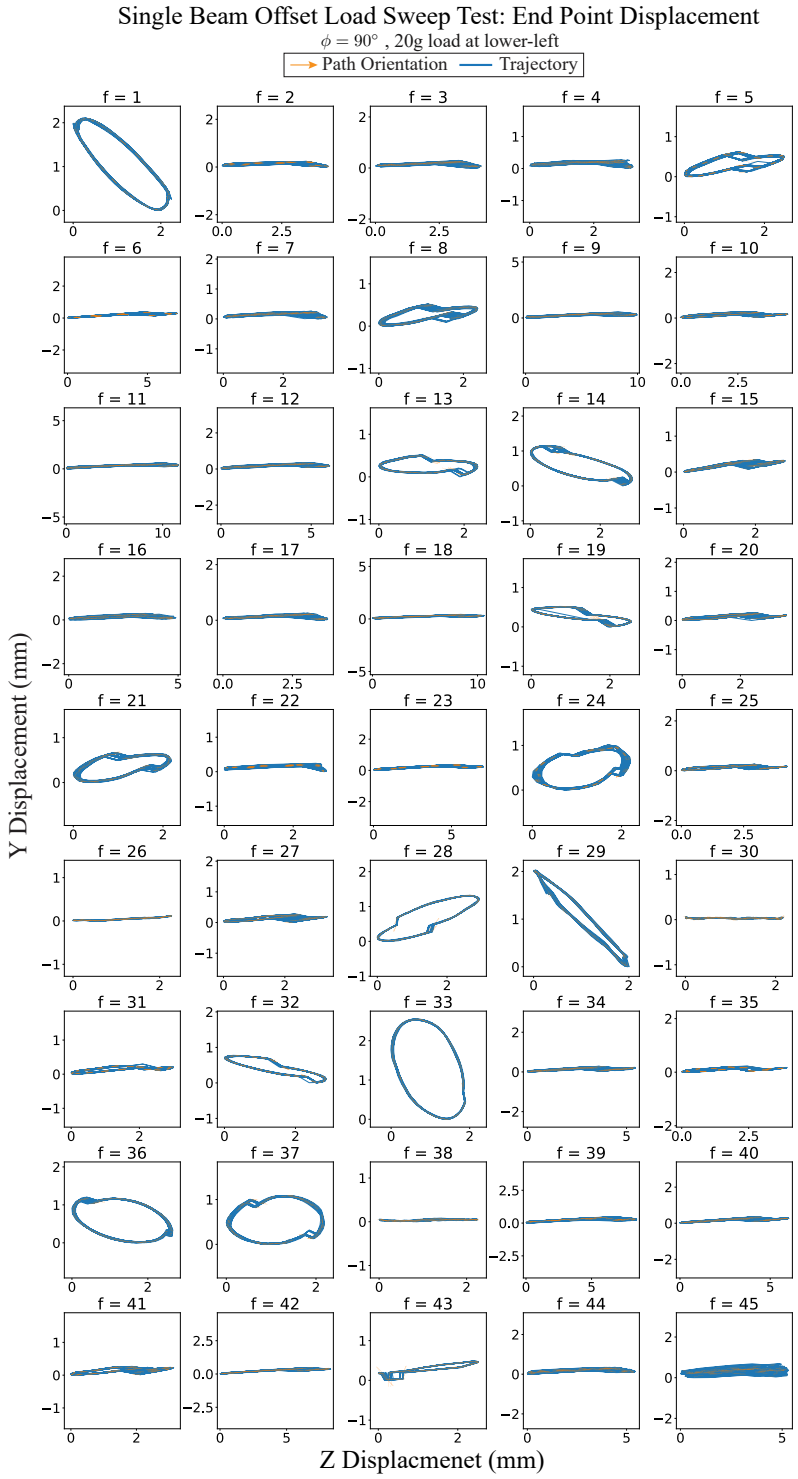

Figure B.5: Single Beam Offset Load Frequency Sweep Test: $\phi = 90°$, Load at Lower-left

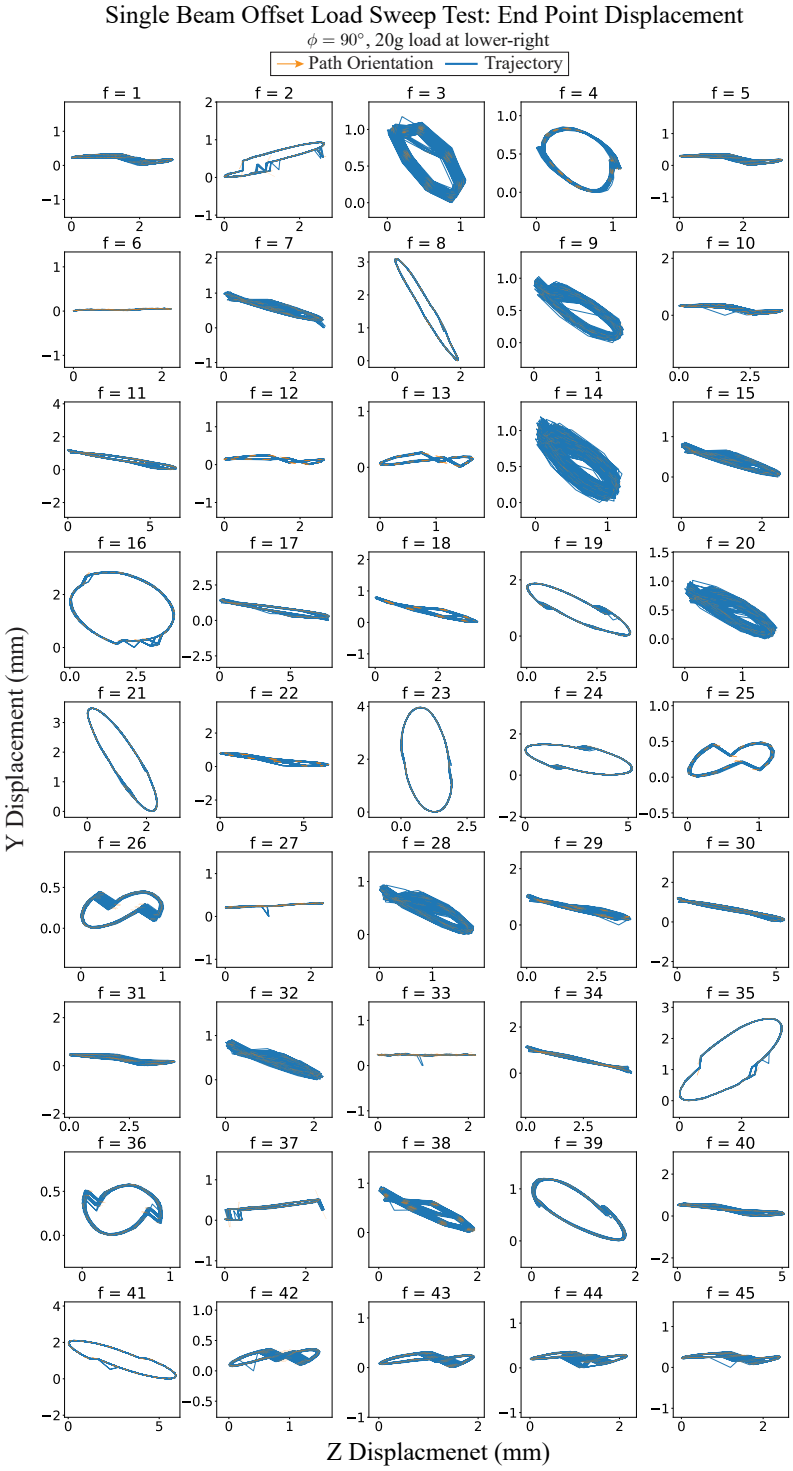

Figure B.6: Single Beam Offset Load Frequency Sweep Test: $\phi = 90°$, Load at Lower-right

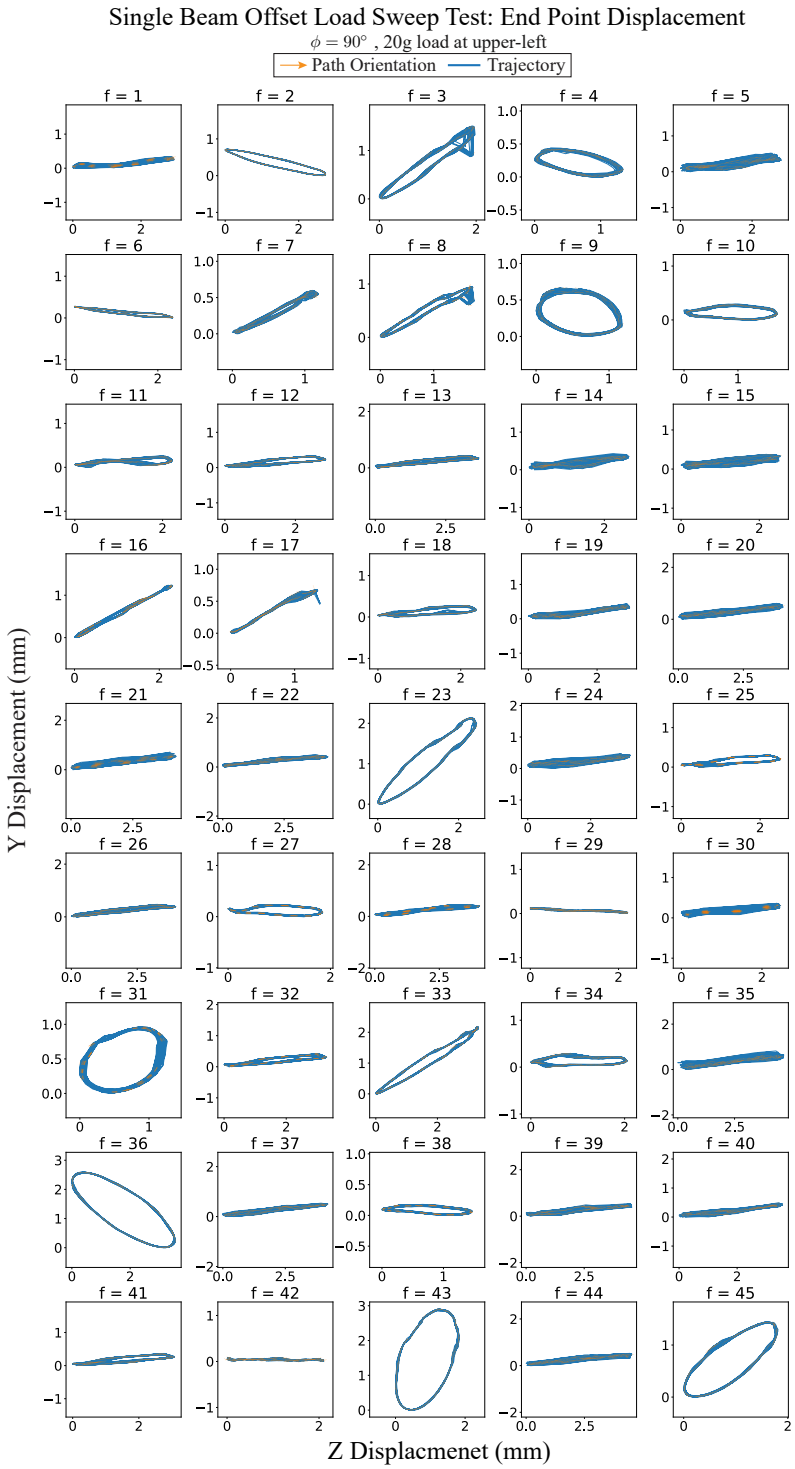

Figure B.7: Single Beam Offset Load Frequency Sweep Test: $\phi = 90°$, Load at Upper-left

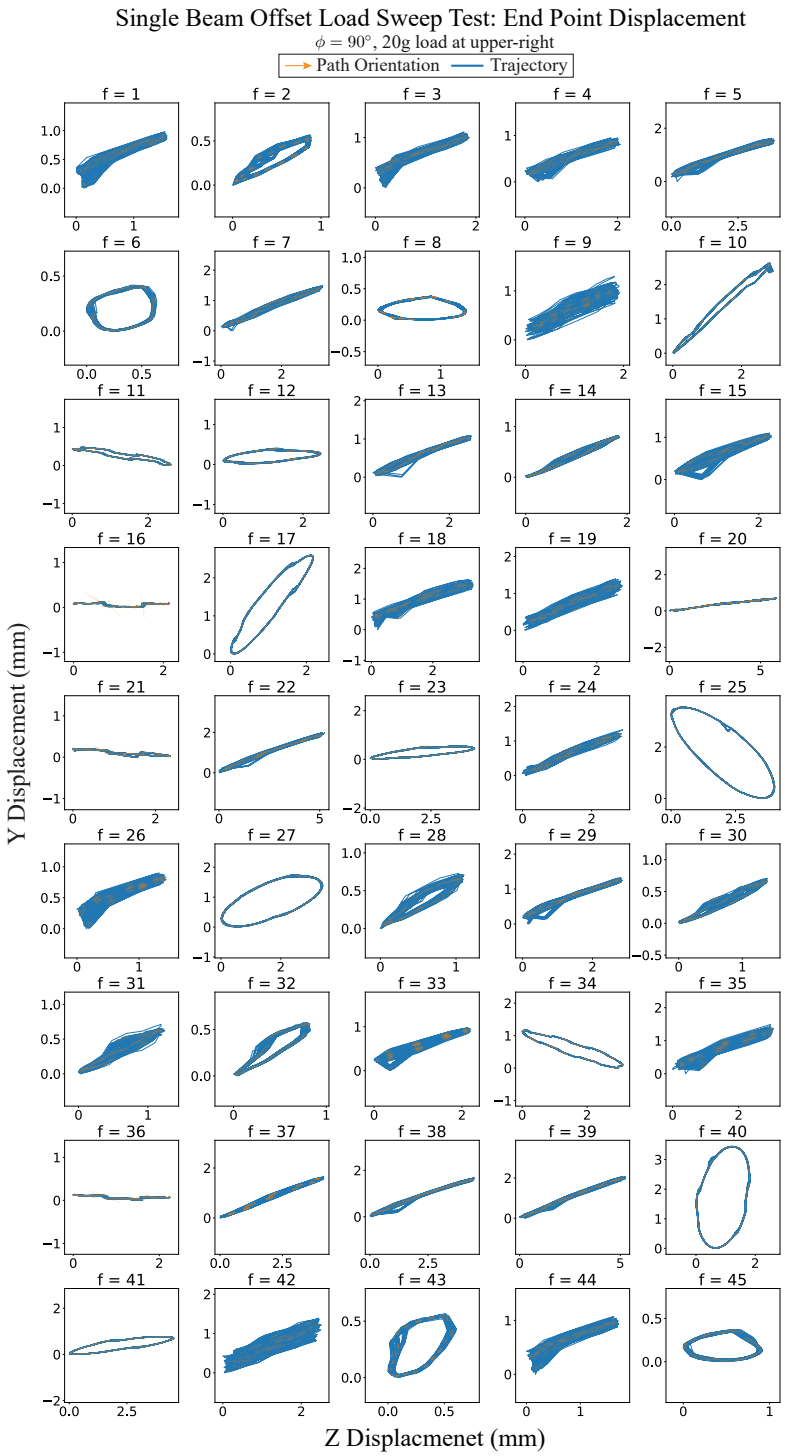

Figure B.8: Single Beam Offset Load Frequency Sweep Test: $\phi = 90°$, Load at Upper-right

APPENDIX C

CONSENT FROM CO-AUTHORS

I acknowledge the use of previously published papers in this dissertation.

- Chapter 3 is employed from paper: Y. Jiang, M. Sharifzadeh, and D. M. Aukes, "Shape Change Propagation Through Soft Curved Materials for Dynamically-Tuned Paddling Robots," 2021 IEEE 4th International Conference on Soft Robotics (RoboSoft), 2021, pp. 230-237;
- Chapter 4 is employed from paper: Y. Jiang, M. Sharifzadeh, and D. M. Aukes, "Reconfigurable Soft Flexure Hinges via Pinched Tubes," 2020 IEEE/RSJ International Conference on Intelligent Robots and Systems (IROS), 2020, pp. 8843-8850;
- Chapter 5 is employed from paper: Y. Jiang, F. Chen and D. M. Aukes, "Tunable Dynamic Walking via Soft Twisted Beam Vibration," in IEEE Robotics and Automation Letters, vol. 8, no. 4, pp. 1967-1974, April 2023.

All co-authors have granted me permission to use these papers in this dissertation.

Yuhao Jiang
July 16, 2023

BIOGRAPHICAL SKETCH

Yuhao Jiang was born and raised in Xi'an, Shaanxi, China. In 2015, he received a Bachelor of Engineering in Mechanical Engineering from Donghua University, Shanghai. After completing his undergraduate studies, he pursued his M.S. in Mechanical Engineering from the University of Florida and graduated in 2017. He continued his academic journey by enrolling in Arizona State University and completed his Ph.D. in Mechanical Engineering in 2023.